UNIVERSITÀ DEGLI STUDI DI PADOVA

Department of Physics and Astronomy "Galileo Galilei"

Master Degree in Astrophysics and Cosmology

Master Thesis

Addressing the disk heating mechanism of the late-type spiral galaxy NGC 7664

Supervisor

Prof. Enrico Maria Corsini

Co-Supervisors

Dott. Chiara Buttitta

Dott. Virginia Cuomo

Student

Pietro Cortese [2023926]

Accademic Year 2021/2022

Contents

Abstract

The scattering due molecular clouds, spiral arms, minor mergers, and bar instabilities has been proposed to explain why disk stars move onto eccentric and inclined orbits, although they formed in a thin layer of gas clouds rotating onto nearly circular orbits in the galactic plane. The shape of the stellar velocity ellipsoid depends on the disk heating mechanism. We constrained the disk heating mechanism of the late-type spiral NGC 7664. The shape of its velocity ellipsoid was already measured with the asymmetric-drift dynamical modelling of the stellar and ionized-gas kinematics along the major and minor axes of the galaxy. The resulting value of $\sigma_z/\sigma_R = 1.37 \pm 0.07$ is peculiar and hard to be theoretically explained. We fitted the NGC 7664 i-band image taken from the SDSS archive with a multi-Gaussian expansion model to parametrize the galaxy surface-brightness distribution. We then used this photometric model to fit the stellar kinematics with the Jeans anisotropic model. We found a best-fitting value of $\sigma_z/\sigma_R = 1.30 \pm 0.07$ by adopting a self-consistent model and $\sigma_z/\sigma_R = 0.97 \pm 0.03$ by adding a dark matter halo to the model. The result of the self-consistent one is consistent with the one previously found, but the model does not properly fit the kinematic data. On the other hand, the implementation of a dark matter halo significantly improves the best-fitting of the stellar kinematics. We conclude that minor mergers are responsible for the nearly-isotropic stellar velocity ellipsoid of NGC 7664. Indeed, the galaxy shows a very low content of molecular gas and displays a tidally-disturbed morphology of its outermost spiral arm. Our results increase the sample of galaxies with a measured stellar velocity ellipsoid shape. In literature we found a number of galaxies which are consistent with $\sigma_z/\sigma_R > 1$, but all the σ_z/σ_R measurements were carried out without taking into account the presence of a dark matter halo. This could be the explanation for these peculiar values. However, to achieve ultimate conclusions, a statistical approach, additional data (e.g. integral-field kinematics), and dynamical models that take into account the spatial variations of the stellar velocity ellipsoid shape are needed.

Chapter 1

Introduction

In Section 1.1 we introduce the case of the dynamical heating of galaxy disks, which is unveiled by assessing the shape of the stellar velocity ellipsoid. In Section 1.2 we present the main mechanisms responsible for disk heating in galaxies, that are the giant molecular clouds, density waves of spiral arms, mergers with satellite galaxies, and instabilities due to a bar. In Section 1.3 we explore the controversial relation between the shape of the stellar velocity ellipsoid and galaxy morphology. Lastly, in Section 1.4 we present the aim of this thesis, namely addressing the disk heating mechanism of the late-type spiral galaxy NGC 7664 and a summary of this work.

1.1   Dynamical heating of galaxy disks

The thickness of the Milky Way disk is about $z_\star \sim 300$ pc, where $z_\star$ represents the scale height of the stellar component in the disk (Binney & Tremaine, 2008). The same is true for the other spirals, as it is evident in the observations of edge-on galaxies (Guthrie, 1992; Padilla & Strauss, 2008). This thickness reveals that the disk stars do not move onto coplanar and circular orbits, despite they formed in a thin layer of molecular gas ($z_{\mathrm{gas}} \sim 50$ pc, where z_{gas} is the scale height of the gas disk), moving onto circular orbits onto the galactic plane (Malhotra, 1995). The process that causes orbit diffusion is called disk heating. The constraints on the disk heating mechanisms are provided by the three-dimensional distribution of the stellar velocity dispersion, whose amplitude and direction are nicely modelled by an ellipsoid function, which was originally proposed by Schwarzschild (1907). The so-called stellar velocity ellipsoid (SVE) is parametrized in cylindrical (R, ϕ, z) coordinates by its radial σ_R, tangential σ_ϕ, and vertical σ_z components, respectively. Its shape can be described by its axial ratios σ_ϕ/σ_R and σ_z/σ_R. For an axisymmetric disk with stellar orbits close to circular (i.e. in epicyclic approximation), σ_ϕ/σ_R depends only on the circular velocity and not on the disk heating mechanism. On the other hand, measurements of the σ_z/σ_R ratio can thus be used to constrain the predominant heating process in galaxy disks. In the solar neighborhood, the ratio between the vertical and radial components of the SVE was measured directly using the radial velocities and proper motions of nearby stars using data from the *Hipparcos* satellite (Dehnen & Binney, 1998), and more recently from the *Gaia* satellite (Gaia Collaboration et al., 2018); it resulted to be $\sigma_z/\sigma_R \simeq 0.5$. It has been also shown that the SVE of disk stars in the solar neighborhood correlates with their ages, which is the age-velocity dispersion relation (AVR, Wielen, 1977). This relation is most commonly parametrized as a power law of the form $\sigma \propto t^p$, where σ is the velocity dispersion, t is the stellar age and p is the exponent, ranging from 0.2 to 0.5 (Wielen, 1977; Nordström et al., 2004; Aumer & Binney, 2009). Moreover, Aumer & Binney (2009) used a new reduction of the *Hipparcos* data, finding a correlation between the velocity dispersion ratios and colors of the stars. The physical meaning of these two relations is that red old stars have larger velocity dispersion with respect to blue young stars because of the slow increase of the random velocities with age attributed to heating due to massive objects such as spiral

arms or molecular clouds. For external galaxies, the shape of the SVE can not be measured directly as in the Milky Way, but it can be derived using the method proposed by Gerssen et al. (1997), that uses the velocity dispersion measured along the line of sight (LOS) of the stellar component for the major and minor axes of a galaxy disk.

1.2 Disk heating mechanisms

Many mechanisms have been invoked to explain why disk heating occurs. Each of them contributes in a different way to the shape of the SVE. The candidate agents for dynamical heating can be classified as:

1. *three-dimensional agents*, responsible for increasing the vertical and radial (and azimuthal) components of the SVE, like the encounters with giant molecular clouds and mergers with satellites.

2. *radial (or planar) agents*, that are involved only in radial (planar) heating, with no effect on the vertical component of the SVE, like the spiral structure which is typical of most disk galaxies.

1.2.1 Giant molecular clouds

Spitzer & Schwarzschild (1951) proposed that disk stars can acquire kinetic energy through stochastic collisions with giant molecular clouds (GMCs) with mass $M_{\mathrm{GMC}} > 10^5$ M$_\odot$. They theorized that all the stars have encounters with GMCs, but only population I stars have a sufficiently short relaxation time $t_{\mathrm{relax}} = n_{\mathrm{relax}} t_{\mathrm{cross}}$, where n_{relax} is the number of galaxy crossings that is required for the velocity of a star, to change by order of itself and t_{cross} is the time needed for a star to cross the galaxy once (Binney & Tremaine, 2008), to affect the SVE. Since the diffusion of stars through collisions with GMCs occur in random directions, the heating of the stellar component is expected to be nearly isotropic ($\sigma_R = \sigma_\phi = \sigma_z$). More recent N-body simulations by Aumer et al. (2016) have confirmed this isotropic diffusion from the collisions between stars and GMCs. Spitzer & Schwarzschild (1951) presented this mechanism before the first observations of GMCs and they suggested it is the responsible for the dynamical heating in the solar neighborhood. It was later shown that heating by GMCs alone fails to explain several observations (Lacey, 1984; Jenkins & Binney, 1990). Indeed, the predicted ratio between the vertical and radial components σ_z/σ_R of the SVE in the solar neighborhood computed with models where GMCs are the only mechanism is too high ($\sigma_z/\sigma_R \simeq 0.75$) compared to the observed value of 0.5 for old stars, the predicted exponent in the AVR is too low with respect to the observed one, and the masses and densities of GMCs determined from observations are too low by a factor of 5 or so to explain the observed dispersion amplitude. The time evolution of the σ_z/σ_R ratio of a simulated Milky Way-like galaxy by Jenkins & Binney (1990) where the scattering with GMCs is the only heating mechanism is shown in Figure 1.1. In this case, we can see that the σ_z/σ_R ratio becomes $\sigma_z = \sigma_R \simeq 0.75$. The observations in the solar neighborhood can be explained from the fact that the influence of GMCs was significantly higher in the past than now, due to higher mass and/or number densities of the GMCs. Hence, their heating efficiency would have decreased over time due to a decline in the star formation rate. As a consequence, we probably need to invoke other heating agents to explain the level of SVE anisotropy observed in later evolutionary stages of the stellar disks.

1.2.2 Density waves of spiral arms

Another heating mechanism is the diffusion of disk stars caused by transient spiral arm waves that lead to potential fluctuations that excite the random motion of the stars (Barbanis & Woltjer, 1967). In fact, galaxy disks are not homogeneous structures, since they are composed by gas, dust, and young stars concentrated in the spiral arms that give rise to these density fluctuations. In this case, the disk appears to be more effectively heated in the radial direction rather then in the vertical one, since the vertical oscillation frequency is higher than the frequency for which the disk stars meet the spiral arms. These interactions have interesting consequences for the distribution of the disk stars. Several numerical studies pointed to spiral arms as the most efficient source of dynamical heating in
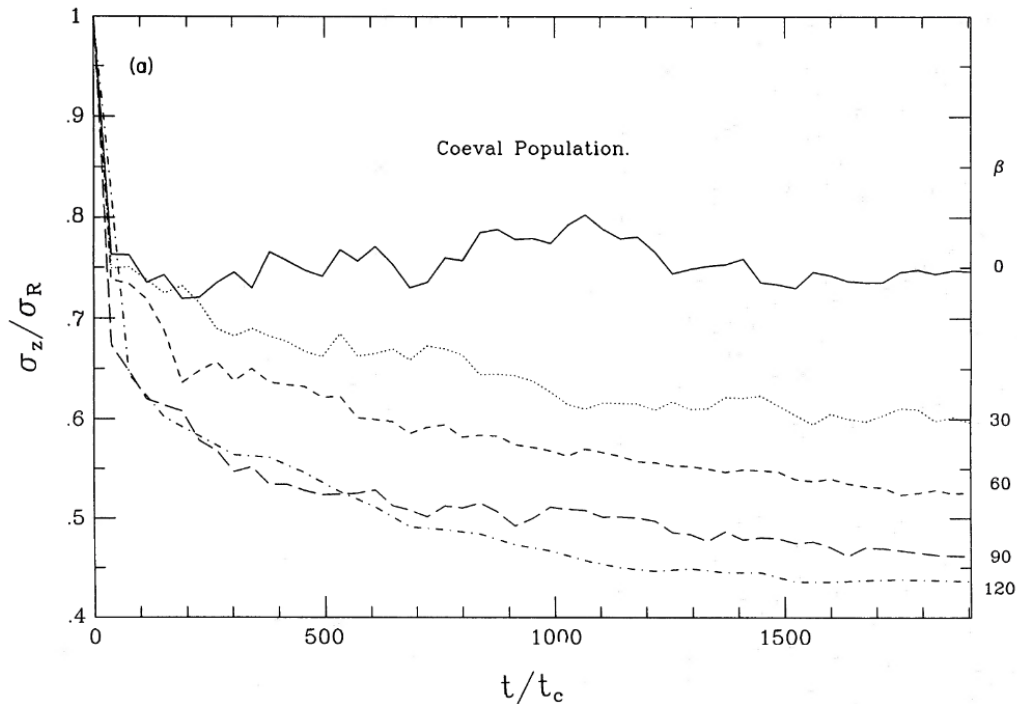
Figure 1.1: Time evolution of the σ_z/σ_R ratio for a coeval stellar population from numerical simulations. The solid line corresponds to disk heating by GMCs only. The other dashed lines are for disks where the heating by spiral arms is increasingly important (from top to bottom) (Jenkins & Binney, 1990).

the disk plane (Jenkins & Binney, 1990; Merrifield et al., 2001). However, the spiral arms only are not sufficient to explain the heating of galaxy disks, because they are not efficient in vertical heating.

These considerations led to an hybrid model, in which the spiral waves excite velocities in the disk plane and vertical velocities are then redistributed between horizontal and vertical motion through scattering due to GMCs (Carlberg, 1987; Jenkins & Binney, 1990). This hybrid model can successfully reproduce the observed σ_z/σ_R ratio and exponent of the AVR in the solar neighborhood. The time evolution of σ_z/σ_R computed from numerical simulations by Jenkins & Binney (1990), where the disk heating is due to both GMCs and spiral arms is shown in Figure 1.1.

1.2.3 Minor mergers

Another important source of disk heating is the interaction between a host galaxy and satellites or globular clusters, mostly in the form of minor mergers (Quinn et al., 1993). In particular, Toth & Ostriker (1992) showed with an analytical model how the infall of a satellite helps to explain the observed scale height in the Milky Way disk. Velazquez & White (1999) studied with numerical simulations the consequences of a merger between a galaxy similar to the Milky Way and a satellite with a initial mass equal to the 20% of the host galaxy disk mass. The result is the disk heating of the host galaxy in the vertical direction, where the value of σ_z increases by $10 - 20$ km s^{-1} and the disk scale height z_0 increases by a factor two. However, the disk heating caused by mergers does not have a single direction, since Velazquez & White (1999) measured changes in velocity dispersion along each axes of the SVE. The resulting shape of the SVE does not change, since the velocity changes along each axes are not significant. They concluded that this mechanism is efficient in heating the disk in all directions. Moreover, Velazquez & White (1999) showed that the disk heating by mergers depends on many parameters, like the direction of the motion, geometry of the satellite orbit, and mass of the spheroid. A massive spheroid can decrease the amount of vertical heating of the disk for a prograde orbit, but it can slowly decrease the disk inclination in a retrograde orbit. These results are consistent with more recent N-body simulations performed by D'Onghia (2015). In this case the
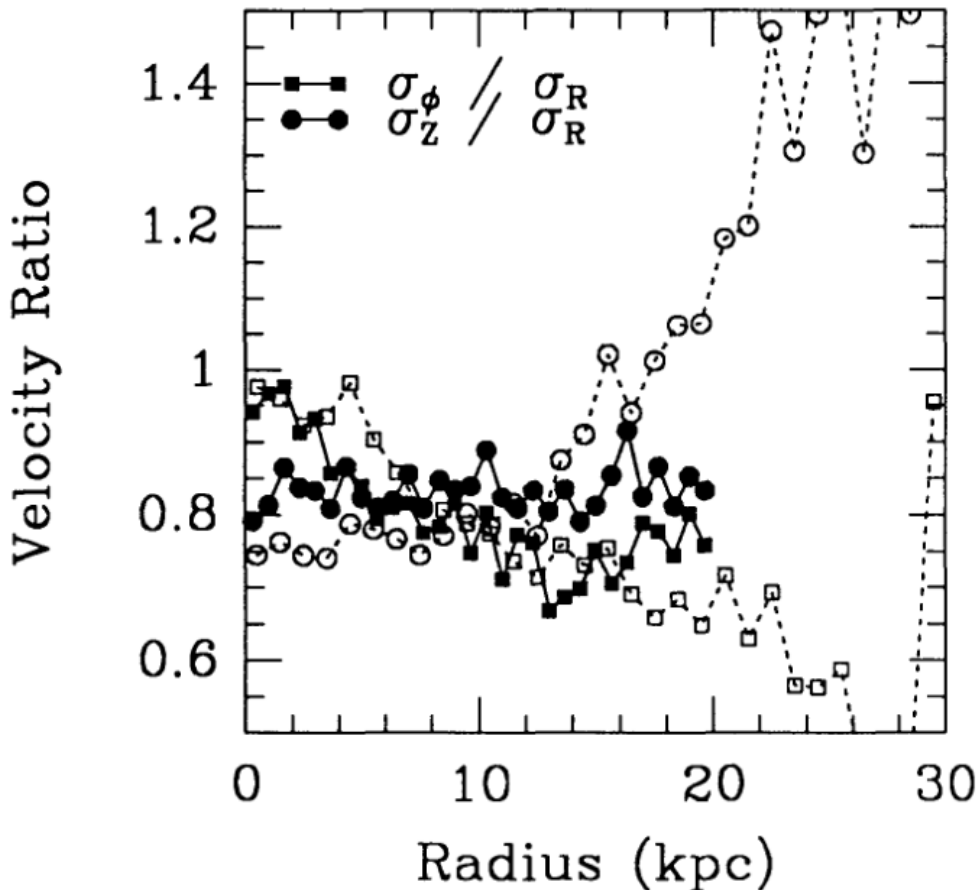
Figure 1.2: Radial profile of the ratios between the SVE components of a disk galaxy before (solid symbols) and after (open symbols) the merger with a satellite from numerical simulations. The circles give the trend of the σ_z/σ_R ratio, while the squares that of the σ_ϕ/σ_R ratio (Quinn et al., 1993).

host galaxy experience a merger with a massive satellite, then with 1000 small satellites, and lastly with 100 satellites where only two of them were massive. Also in the simulations by Kazantzidis et al. (2008) vertical, radial, and azimuthal velocity dispersions increase at the same time during mergers with satellite, without affecting the shape of the SVE but only its size. This result is in agreement with the kind of interaction known as three-dimensional heating agent. The ratios between the SVE components calculated from numerical simulations by Quinn et al. (1993) before and after the merger with a satellite galaxy are shown in Figure 1.2.

1.2.4   Bar instabilities

Using 70 high-resolution N-body simulations, Saha et al. (2010) found that instabilities due to the growth of a bar is a potential source of disk heating. There is a positive correlation between the bar growth and vertical heating of the disk stars, especially in the inner regions of the galaxy. These stars are generally heated in the vertical direction by a factor ~ 3 to 4 above their initial values over 5-6 Gyr. From the analysis of their simulations, Saha et al. (2010) found that in radially hot galaxies the vertical heating in the central regions dominates over radial heating, while the relative importance is inverted in the outer regions. In contrast, the radial heating dominates over vertical heating throughout the disk for radially cold galaxies. They concluded that their simulations suggest the presence of a common physical process between the disk heating in the vertical direction and growth of a bar. The vertical heating evolution of a barred galaxy from Saha et al. (2010) simulations is shown in Figure 1.3. Grand et al. (2016) confirmed later that bar instabilities are an important contributors to the disk heating, after associating the bar buckling to a sudden increase in vertical kinetic energy.
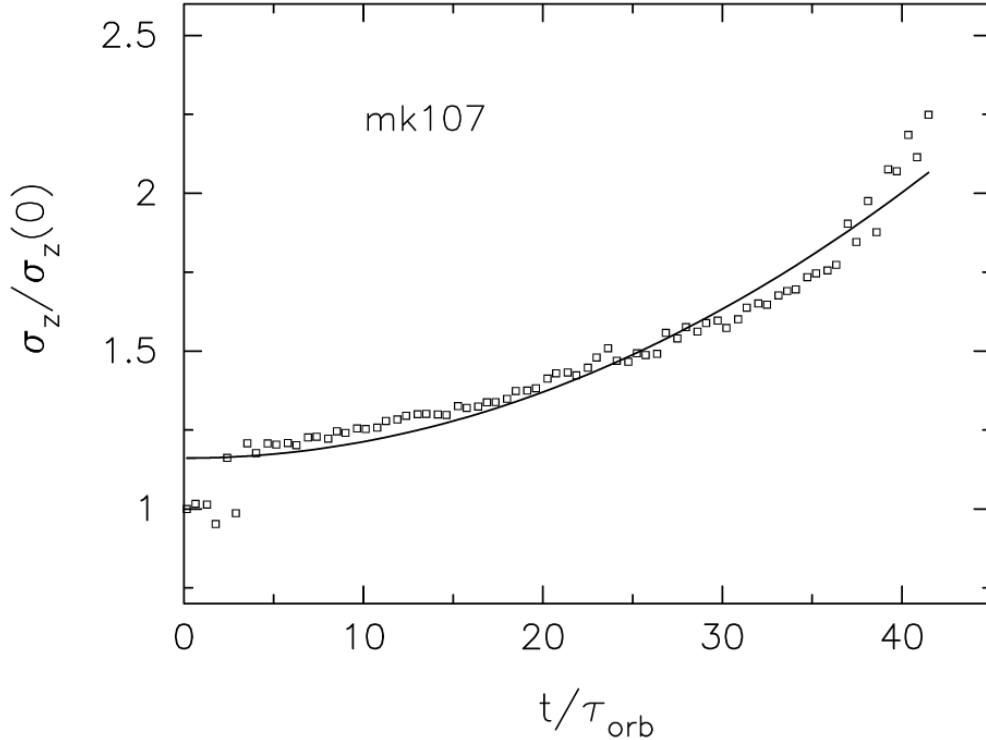
Figure 1.3: Time evolution of the vertical SVE component σ_z from the numerical simulation of a galaxy, where the main heating mechanism was the bar instability. The solid line is the model fitted to the simulated data (Saha et al., 2010).

1.3   Relation between the σ_z/σ_R ratio and Hubble type

Since each mechanism contributes to the disk heating in a different way, measuring the shape of the SVE in the disk of a galaxy allows us to identify the dominant source of dynamical heating. Using the available photometric and spectroscopic data of three disk galaxies having intermediate inclination, Merrifield et al. (2001) proposed that the main disk heating mechanism varies according to the morphological type of the galaxy. They found that the earlier was the Hubble type of the galaxy, the larger was the value of σ_z/σ_R. They proposed that galaxy interactions may provide a plausible explanation for this correlation. They concluded that σ_z/σ_R had to be measured for a larger sample of galaxies before drawn any general conclusion. Later on, Gerssen & Shapiro Griffin (2012) measured the shape of the SVE of eight spiral galaxies with Hubble types from Sa and Scd to probe this relation, finding a tight relation between galaxy morphology and the σ_z/σ_R ratio, as it can be seen in Figure 1.4.

Pinna et al. (2018) collected the literature values of the σ_z/σ_R ratio and morphological type for 55 galaxies. In addition, they extracted the σ_z/σ_R ratio for 32 galaxies of different morphological types from the numerical simulations by Martig et al. (2012) and Martinez-Valpuesta et al. (2007, 2017). Their plots of the σ_z/σ_R ratio as a function of the Hubble type from observations and simulations are shown in Figure 1.5. From this figure, it can not be seen a clear correlation between the shape of the SVE and Hubble type in both observations and simulations. This result is in disagreement with the trend found by Gerssen & Shapiro Griffin (2012). Pinna et al. (2018) explained that is partially due by the fact that the sample of Gerssen and Shapiro Griffin was carefully selected for having "optically regular-looking morphologies" and the typical appearance of their specific Hubble type. On the other hand, the Pinna et al. (2018) sample includes 55 galaxies of all kind and suggests a much more complicated and realistic picture. Moreover, Pinna et al. (2018) calculated the mean value of $\sigma_z/\sigma_R = 0.70 \pm 0.20$ from all the values in literature, while the mean value from the simulated galaxies is $\sigma_z/\sigma_R = 0.60 \pm 0.15$. The lack of a tight correlation between morphological type and
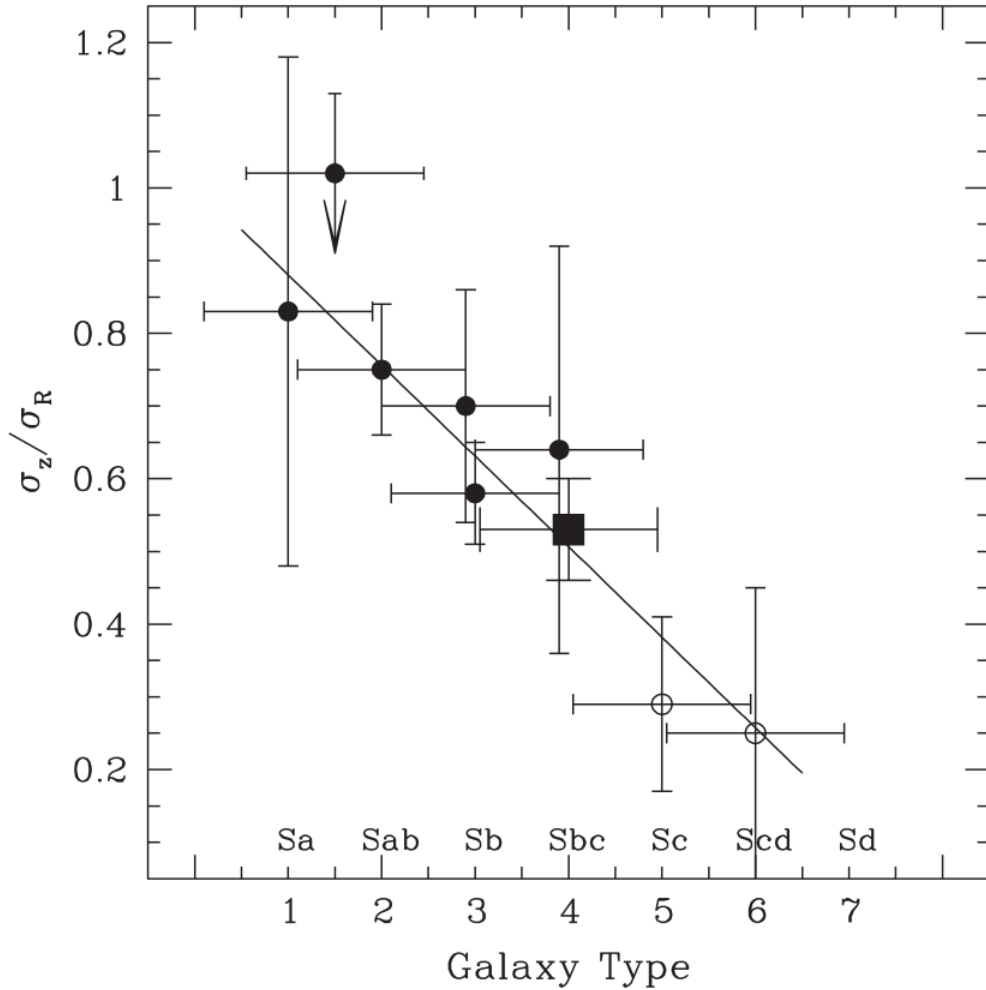
Figure 1.4: The σ_z/σ_R ratio as a function of Hubble type. The solid and open circles are the results of Shapiro et al. (2003). The filled square is the value in the solar neighborhood by Dehnen & Binney (1998). (Gerssen & Shapiro Griffin, 2012).

disk heating mechanism was confirmed by Walo-Martín et al. (2021). They studied the σ_z/σ_R ratio by looking at 40 spiral galaxies taken from the *Auriga* cosmological zoom-in simulations of late-type galaxies (Grand et al., 2017). However, they found that *Auriga* galaxies present an average value of $\sigma_z/\sigma_R = 0.80 \pm 0.08$, which is higher with respect to the ones found by Pinna et al. (2018). They concluded, that this apparent discrepancy is not caused by differences in the stellar mass distribution of the samples, but the results differ slightly because each simulation uses its own sub-grid modules to implement the physics of process.

Another aspect that was studied by means of cosmological simulations is the evolution of the SVE shape with time (Martig et al., 2014; Pinna et al., 2018; Walo-Martín et al., 2021). This gives us information about how long a particular disk heating mechanism influences the SVE shape. Pinna et al. (2018) studied the time evolution of the SVE shape of five simulated galaxies finding that the time when we look at the SVE is relevant. In four of them, they found an isotropic or anisotropic SVE depending on time. However, they concluded that changes in the SVE shape are not necessarily related to disk heating in the vertical direction but can be also caused by a decrease in radial or vertical dispersions, or an increase (or decrease) in both directions but with different amounts. On the other hand, the time evolution studied by Walo-Martín et al. (2021) using the *Auriga* galaxies shows that in absence of mergers the formation of stars in colder orbits causes σ_R and σ_z to steadily decrease with time. Simultaneously, the SVE ratio reaches a steady value quite early and then it does not evolve too much. So, the only disk heating mechanism that causes a major change in the shape of the SVE is a merger event. However, Walo-Martín et al. (2021) concluded that the global σ_z/σ_R ratio of the
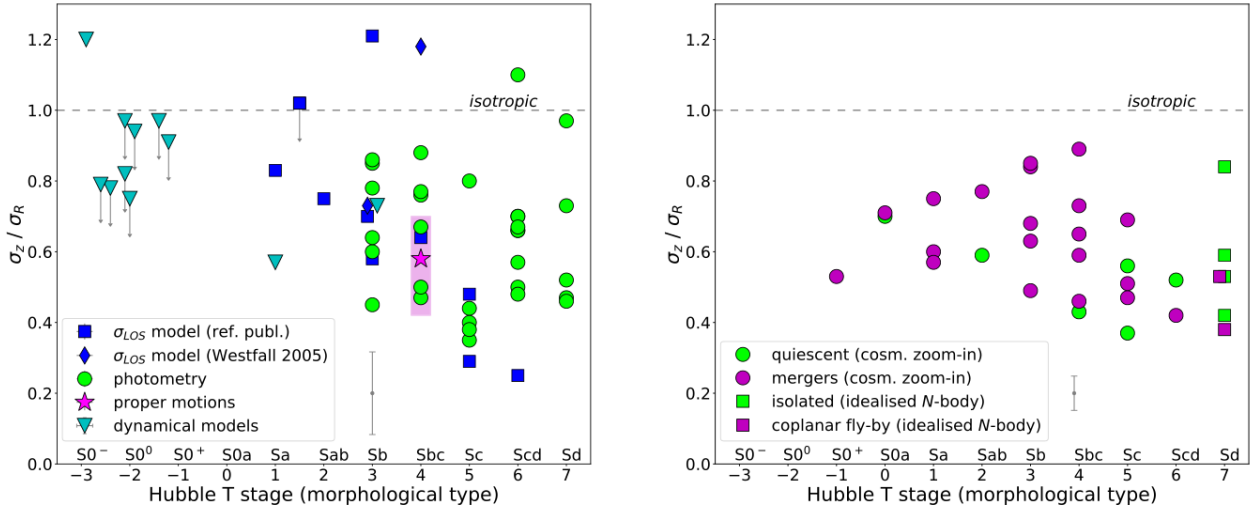
Figure 1.5: The σ_z/σ_R ratio as a function of Hubble type from observations and simulations. The horizontal dotted line indicates the isotropic case ($\sigma_z = \sigma_R$) *Left panel*: values obtained from the observations of 55 galaxies. Different symbols and colors are used for different techniques and methods. A mean error bar is shown on the right of the legend. *Right panel:* values obtained from cosmological simulations of 32 galaxies. Different symbols and colors indicate different types of simulations. A mean error bar is shown at the right side of the legend (Pinna et al., 2018).

whole galaxy is not useful to determine the dynamical evolution of the galaxy, since similar ratios can be obtained through different mechanisms. On the other hand the spatial variations of the SVE are important because they can be used to reconstruct parts of the evolution history of a galaxy. They concluded that their results show the necessity of methods capable of revealing the local variations of the SVE in observations and simulations to investigate the dynamical heating history of galaxies. The SVE time evolution of an interacting and no-interacting galaxy taken from Walo-Martín et al. (2021) is shown in Figure 1.6.

1.4   Aim and summary of the thesis

The purpose of this thesis is to address the disk heating mechanism of the late-type spiral galaxy NGC 7664, whose SVE was already studied by Cuomo (2015) who found a controversial result ($\sigma_z/\sigma_R = 1.34 \pm 0.07$).

NGC 7664 is a late-type galaxy classified as Sc by de Vaucouleurs et al. (1991). The Sc galaxies are characterized by a very small nucleus, the arms have an open pattern, defined as a large angle between the spiral locus and the osculating circle at any given point in the spiral, and present an high rate of recent star formation in the arms (Sandage & Bedke, 1994). Its equatorial coordinates (J2000.0) are RA = $23^{\mathrm{h}}26^{\mathrm{m}}39.76^{\mathrm{s}}$ and Dec = $25°4'48.5''$. It is characterized by an apparent magnitude $B_T = 13.42$ mag (Kent, 1988), which corresponds to a total absolute magnitude $M^0_{B_{\mathrm{T}}} = -20.4$ mag, obtained adopting a distance $D = 46.1 \pm 3.2$ Mpc from the radial velocity with respect to the cosmic microwave background reference frame $V_{\mathrm{CMB}} = 3474 \pm 1$ km s^{-1}(Huchra et al., 1999) and assuming $H_0 = 67.8$ km s^{-1} Mpc^{-1} (Planck Collaboration et al., 2014). The redshift z of NGC 7664 is $z = 0.01159$. The apparent isophotal major and minor diameters measured at a surface brightness level of $\mu_B = 25$ mag arcsec^{-2} are $D_{25} \times d_{25} = 2.5$ arcmin $\times$ 1.5 arcmin (de Vaucouleurs et al., 1991), which correspond to a galaxy size of 20.1 kpc $\times$ 8.0 kpc.

The thesis is organized in the following way:

1. In the first chapter we introduce the dynamical heating in galaxies and the mechanisms that produce it. In Section 1.1 we introduce the case of the dynamical heating of galactic disks, which is unveiled by assessing the shape of the stellar velocity ellipsoid. In Section 1.2 we present the
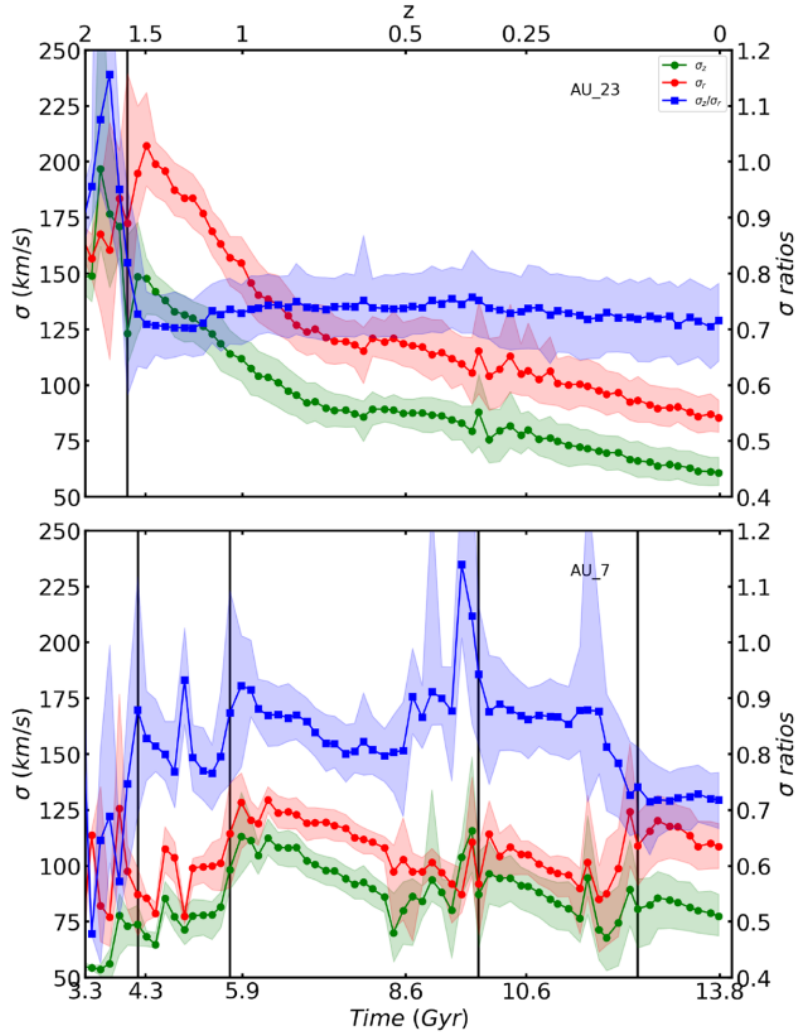
Figure 1.6: Evolution of σ_z (green circles), σ_R (red circles), and σ_z/σ_R (blue squares) as function of time (bottom axis) and redshift (top axis). *Top panel:* evolution for an isolated galaxy with no strong interactions. *Bottom panel:* evolution for a galaxy which experienced multiple mergers. The epoch of the mergers is marked by vertical lines. The left and right-hand vertical axes indicate the amplitude of the velocity dispersions and σ_z/σ_R, respectively (Walo-Martín et al., 2021).

main mechanisms responsible for disk heating in galaxies, that are the giant molecular clouds, density waves of spiral arms, mergers with satellite galaxies, and instabilities due to a bar. In Section 1.3 we explore the controversial relation between the shape of the stellar velocity ellipsoid and galaxy morphology. Lastly, in Section 1.4 we present the aim of this thesis, namely addressing the disk heating mechanism of the late-type spiral galaxy NGC 7664 and a summary of this work.

2. In the second chapter we present the acquisition and analysis of the photometric data. In Section 2.1 we briefly describe the *Sloan Digital Sky Survey*. In Section 2.2 we present the acquisition and the sky subtraction of the NGC 7664 *i*-band image. In Section 2.3 we present the ellipse fitting results. In Section 2.4 we explain the multi-Gaussian expansion decomposition formalism and in Section 2.5 we present the results of our photometric modelling.

3. In the third chapter we describe how the spectroscopic data were retrieved and reduced to measure the stellar and ionized-gas kinematics of NGC 7664. In Section 3.1 we briefly describe the *Gemini North* telescope and in Section 3.2 we present the spectroscopic observations of NGC 7664. Then, in Section 3.3 we describe the steps of the spectra reduction. Lastly, in Section 3.4 we describe the procedures to extract the stellar and ionized-gas kinematics and in Section 3.5

we present the measurement of the NGC 7664 stellar and ionized-gas kinematics.

4. In the fourth chapter we present how the σ_z/σ_R ratio was calculated using the asymmetric drift modelling. In Section 4.1 we describe the derivation of the asymmetric drift equation from the second Jeans equation. In Section 4.2 we present how to link the vertical and radial components of the velocity ellipsoid with observable quantities. Then, in Section 4.3 we describe the procedure used to measure the σ_z/σ_R ratio with the asymmetric-drift equation from the kinematic data and the obtained results for NGC 7664.

5. In the fifth chapter we describe the dynamical modelling on the photometric and kinematic data that we used to derive the shape of the SVE of NGC 7664. In Section 5.1 we describe the Jeans anisotropic model. In Section 5.2 we explain how we applied the Jeans modelling, while in Section 5.3 we present our results.

6. In the sixth chapter we discuss the obtained results and we present the future perspectives and conclusions of this thesis. In Section 6.1 we summarize the results we obtained. In Section 6.2 we discuss these results and we present the galaxies we found in literature with a SVE possibly elongated along the vertical direction. In Section 6.3 we describe the future perspectives of this thesis, that are the application of integral-field spectroscopy and orbit-superposition dynamical modelling. Finally, in 6.4 we present the conclusions.

Chapter 2

Photometric data

In this chapter we present the acquisition and analysis of the photometric data. In Section 2.1 we briefly describe the *Sloan Digital Sky Survey*. In Section 2.2 we present the acquisition and the sky subtraction of the NGC 7664 *i*-band image. In Section 2.3 we present the ellipse fitting results. In Section 2.4 we explain the multi-Gaussian expansion decomposition formalism and in Section 2.5 we present the results of our photometric modelling.

2.1 *Sloan Digital Sky Survey*

The *Sloan Digital Sky Survey* (SDSS) is a major multi-band imaging and spectroscopic survey using a dedicated optical telescope at the *Apache Point Observatory* (APO) in New Mexico, United States. The telescope has a Ritchey-Chrétien design with a 2.5 meters ($f/2.25$) primary mirror, a 1.08 meters secondary mirror, a Gascoigne astigmatism corrector, and one pair of interchangeable highly aspheric correctors near the focal plane (one for imaging and the other for spectroscopy). The resulting final focal ratio is $f/5$. The SDSS telescope is instrumented by a wide-area, multi-band CCD camera and a pair of fiber-fed double spectrographs (Gunn et al., 2006). The optical configuration is shown in Figure 2.1. Since 2017, the SDSS collects images also in the southern emisphere, using the *du Pont Telescope* located at the *Las Campanas Observatory*.

Data collection began in 1998 and since then the telescope observed in both imaging and spectroscopic modes until 2009. Then, in late 2009 the imaging camera was retired and the telescope observed only in spectroscopic mode. Images were taken using a photometric system of five bands: u, g, r, i and z, centered at the wavelengths 3551 Å, 4686 Å, 6165 Å, 7481 Å, and 8931 Å, respectively (Fukugita et al., 1996). The corresponding efficiency curves are shown in Figure 2.2. The imaging camera was made up of 30 CCDs, with 2048×2048 pixel each. The CCDs are arranged in five rows composed by six detectors, where each row has a different filter. The spatial scale of the CCDs is $s = 0.3961 \ \mathrm{arcsec\,pixel^{-1}}$; the properties of the CCDs are listed in Table 2.1. This corresponds to a total field size of 2.5° (each CCD has a field of view of 13.53×8.98 arcmin). Using the photometric data, part of the stars, galaxies, and quasars observed with the SDSS telescope were selected for spectroscopy. The spectrograph operates by feeding an individual optical fiber for each target (Newman et al., 2004). The original spectrograph was capable of recording 640 spectra simultaneously, while the updated one can record 1000 spectra at once. The wavelengths of the spectra taken with the SDSS telescope ranges between $3500 - 10000$ Å.

The Data Release 17 (DR17) is the final data release of the fourth phase SDSS observative campaigns (Abdurro'uf et al., 2022) started in 2014. In particular, the DR17 was focused on the following three campaigns:

1. the *Extended Barion Oscillation Spectroscopic Survey* (eBOSS), that aims to detect red bright galaxies and quasars to measure the characteristic scale on the primordial Universe from the acustic barionic oscillation (Percival, 2017);
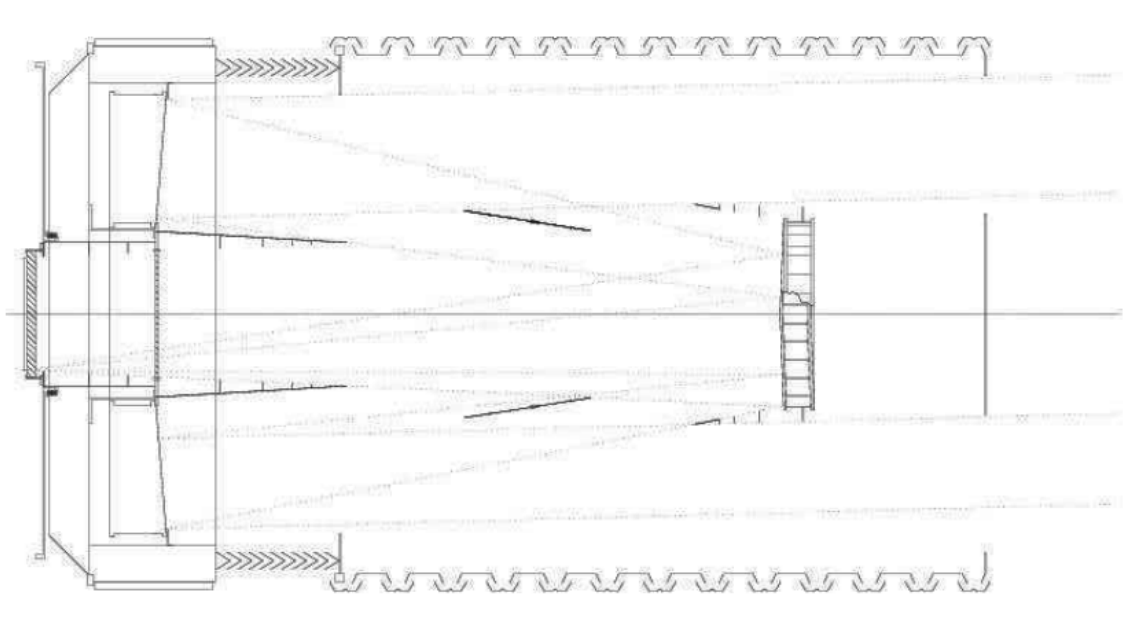
Figure 2.1: SDSS telescope optical configuration. The light baffles and a set of rays from the field edge are shown. The Gascoigne corrector is nearly coincident with the vertex of the primary mirror. The second transmissive corrector, which forms the main structural element of the SDSS mosaic camera is just before the focal plane (Gunn et al., 2006).

2. the *APO Galactic Experiment* (APOGEE-2), that produces high resolution spectra of red giant stars in the Milky Way disk and spheroid, to study chemical abundances and radial velocities (Majewski et al., 2017);

3. the *Mapping Nearby Galaxies at APO* (MaNGA), that explored the detailed internal structure of nearly 10000 nearby galaxies to study their properties, such as radial velocities and star formation regions (Bundy et al., 2015);

The DR17, released in December 2021, encompasses more then one-third of the entire celestial sphere (14555 square degrees) with over 1.2 billion objects contained in the image catalog. The spectroscopic catalog contains also more then 5.7 million spectra of different astrophysical sources (Abdurro'uf et al., 2022).

2.2   Image acquisition and reduction

We retrieved the i-band multilayer image of NGC 7664 from the Data Archive Server (DAS) of the SDSS Data Release 17 (Abdurro'uf et al., 2022). The NGC 7664 image was already bias-subtracted,

Table 2.1: Properties of the 30 CCDs used for the SDSS imaging. The column are: (1) filter used on the CCD; (2) gain of the CCD; (3) read out noise; (4) mean quantum efficiency. (Gunn et al., 1998, 2006).

Filter	Gain $[e^- \text{ ADU}^{-1}]$	Noise $[e^- \text{ rms}]$	$\langle \text{ QE } \rangle$
(1)	(2)	(3)	(4)
u	2	7	0.36
g	5	7	0.72
r	6	9	0.82
i	6	20	0.69
z	6	16	0.18

Figure 2.2: Efficiency curves for the SDSS photometric fiters. The response of the u (green line), g (blue line), r (black line), i (red line), and z (purple line) filters are shown as a function of the wavelength (Doi et al., 2010).
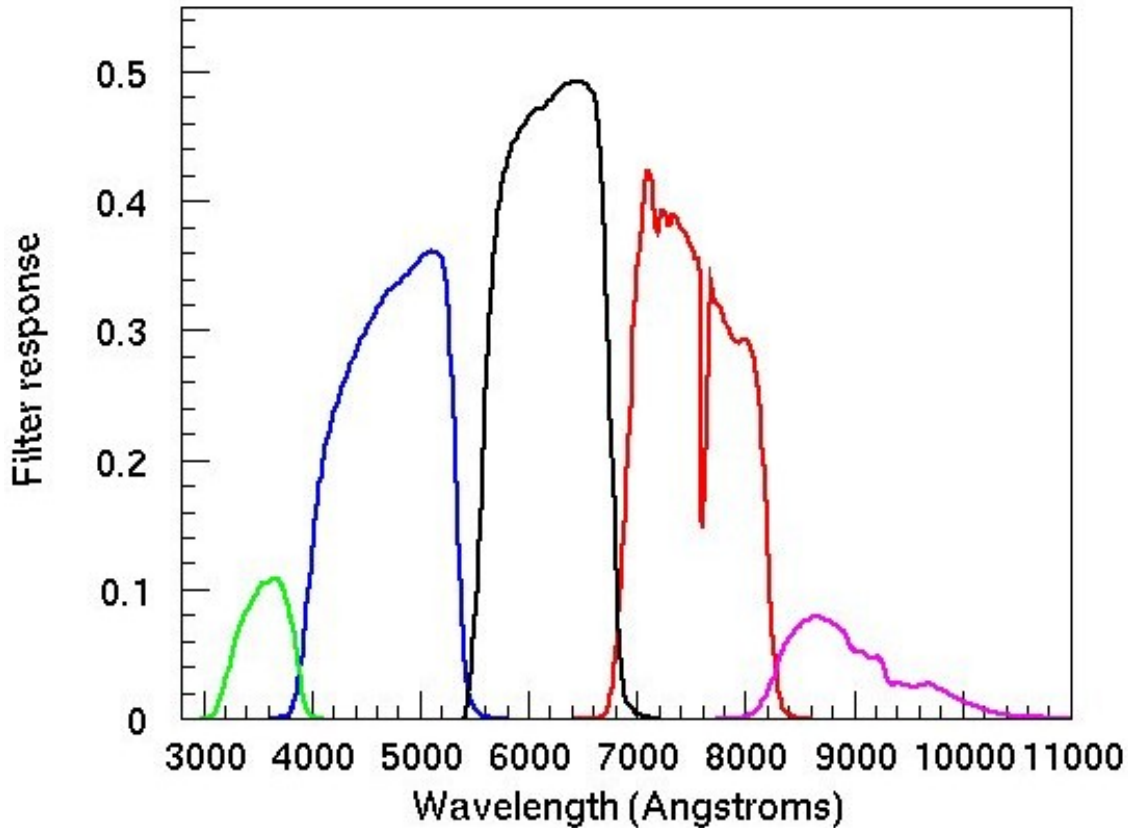
flat-field corrected, sky-subtracted and flux-calibrated according to the associated calibration infor-mation stored in the DAS. We processed the multilayer image with the `python3` script `read_sdss` by C. Buttitta (the original IDL script was written by E.M. Corsini and L. Costantin), that decompose the layers and gives as output:

- an uncalibrated image in count of the galaxy NGC 7664 not subtracted for the surface brightness of the sky;

- an uncalibrated image in count of the galaxy subtracted for the surface brightness of the sky;

- a calibration image in nanomaggies count^{-1}. The nanomaggies are a linear unit for the luminous flux. They are linked to the apparent magnitude with the relation $m = 22.5 - 2.5 \log f$, where m is the apparent magnitude in mag and f is the flux in nanomaggies;

- a calibration file, that contains the constants of calibration for the i band in magnitude units and surface brightness units, the mean value and root mean square (rms) of the sky automatically calculated by the SDSS.

With a `python3` script, we rotated the image by an angle $\alpha = -84.322°$, that is the opposite of the camera angle with respect to the north. In addition to that, we trimmed the rotated image in a region 800 pixel $\times$ 800 pixel centered in the center of the galaxy (estimated by eye). Moreover, before performing the analysis, we masked all the spurious sources in the image (i.e. field stars and nearby galaxies). Since we want to trace the radial surface brightness profile, it is important to mask all the sources located both near the galaxy and in the outer regions of the image. We created the mask starting from circular regions manually selected on the image with the software `SAOImage DS9`[1] (DS9).

---

[1]The image viewer software `SAOImage DS9` is available at the following link: `http://ds9.si.edu/site/Home.html`
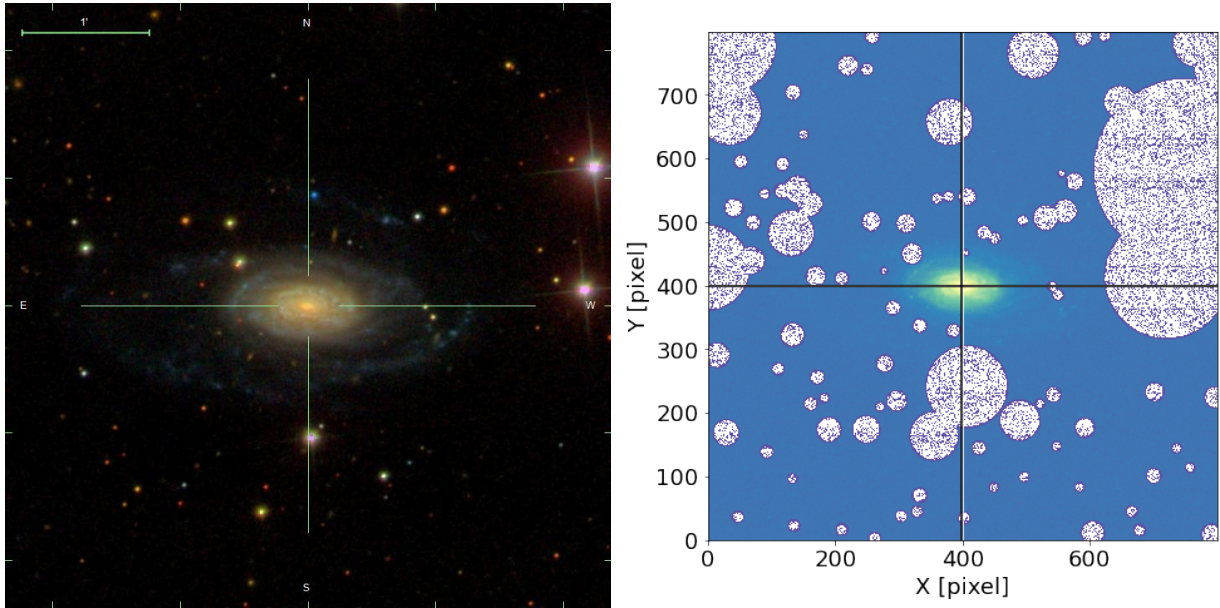
Figure 2.3: Images and mask of NGC 7664. *Left panel:* SDSS multi-band image. The scale is shown in the top left corner. *Right panel:* SDSS *i*-band image with white circles marking the masked pixels.

Then, with a `python3` script, these regions were used to create the mask to be applied to galaxy image. The masked *i*-band image of NGC 7664 is shown in the right panel of Figure 2.3.

2.2.1   Sky level estimation

The images obtained from the SDSS are already subtracted from the mean sky surface brightness. However, in some cases the correction is not sufficiently good. The sky subtraction performed by the SDSS consists in a global estimation on the whole field of view, while the most luminous sources are masked (Aihara et al., 2011). Sometimes, this procedure does not properly work, and for this reason we estimated the sky level and subtracted the image for its contribution.

In order to estimate the sky level and check if it is consistent with the value given in the SDSS image, we modeled the luminosity of the galaxy by fitting elliptical isophotes to the NGC 7664 uncalibrated masked image; in particular, we focused on the galaxy outer regions, where the galaxy contribution to the image luminosity is negligible with respect to the sky contribution. We used the subpackage `photoutils.isophote` (Jedrzejewski, 1987) of the `python3` library `photoutils`[2]. The isophotal fitting with ellipses was done by imposing the ellipses to have semi-major axis of length that goes from 40 pixels (15.8 arcesc) to 450 pixels (178.2 arcsec), since we wanted to analyze the outer regions of the galaxy, where the sky contribution starts to dominate. The step between two consecutive ellipses was set to 1 pixel, to have a sufficiently large number of data. We also provided the parameters for an initial guess ellipse to be fitted: these are the semi-major axis $a = 40$ pixel, ellipticity defined as $\epsilon = 1 - \frac{b}{a} = 0.4$, where a and b are the semi-major and semi-minor axes of the ellipse respectively, and position angle PA $= 0°$ defined as the angle between the semi-major axis of the ellipse and directed to the north celestial pole, turning positive eastward. The center coordinates of the guess ellipse were set to the values of light peak of the NGC 7664. They were calculated using the algorithm `centroid_com` of subpackage `photoutils.centroids` of the `photoutils` library, which calculates the object "center of light" from the image moments. We also checked if the coordinates x_0 and y_0 of the ellipses center did not vary within the uncertainties as function of the ellipse semi-major axis, by performing an ellipse fitting in the inner regions where the center coordinates were left as free parameters (Figure 2.4). Then, we fixed x_0 and y_0 to the value of the guess ellipse, that coincided with the galaxy center.

The fitting procedure produces a file that contains the surface brightness I, PA, and ϵ of the fitted

---

[2]The `photoutils` source code can be found at the following link: `https://github.com/astropy/photoutils`.
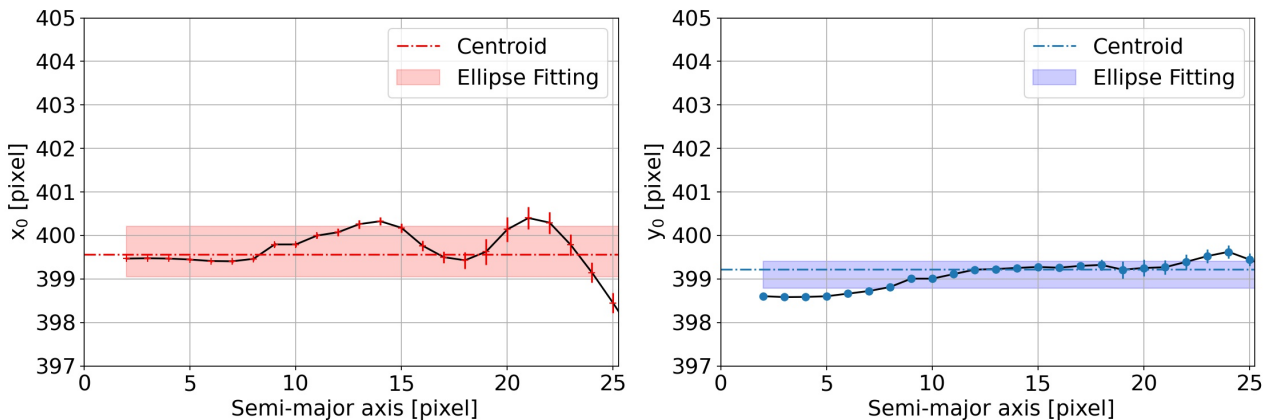
Figure 2.4: Variation of center coordinates x_0 (*left panel*) and y_0 (*right panel*) of the fitted ellipses on the i-band image of NGC 7664 as a function of the ellipse semi-major axis. The red and blue points are the fitted coordinates, while the red and blue strips are the confidence regions centered on the mean values. The horizontal dashed and dotted red blue lines are the values of the galaxy center coordinates obtained with the algorithm `centroid_com`.

ellipses with their associated errors. Then, we used the surface brightness of the fitted ellipses in count pixel^{-1} as a function of the semi-major axis length to estimate the sky level. We fitted the surface brightness of the isophotes with a straight line of the form $I = m \cdot r + I_{\mathrm{sky}}$, where I is the luminosity as a function of the ellipse semi-major axis a, m is the angular coefficient and I_{sky} is the level of the sky; the fitting is done until the angular coefficient is above $|m| > 10^{-5}$. The resulting sky level is $I_{\mathrm{sky}} = 137.37 \pm 0.16$ count, compatible with the value of 137.51 ± 0.26 count that can be found in the SDSS calibration file. The value we found for the sky was subtracted to the image.

2.3 Ellipse fitting

To derive the surface brightness (μ_i), PA and ϵ radial profiles of NGC 7664 we fitted elliptical isophotes to the sky subtracted i-band image, using the `python3` package `photoutils.isophotes`, used for the sky background estimation (Section 2.2.1). For the initial guess ellipse, we provided the same parameters adopted in Section 2.2.1. However, since we now want to fit the region in which the galaxy dominates the surface brightness, we imposed the semi-major axis of the fitted ellipses to range from 1 pixel (0.4 arcsec) to 420 pixels (166.4 arcsec), with a length step between consecutive ellipses of 1 pixel. The coordinates x_0 and y_0 of the ellipse center were fixed to the values of the initial guess ellipse, that coincides with the galaxy center found using the `centroid_com` package.

The fitted ellipses are overplotted to the i-band image of NGC 7664 in Figure 2.6, together with the model of the galaxy surface brightness derived from the fitted ellipses and the map of the relative residuals, derived for each point $P(x,y)$ of the image as:

$$residuals = \frac{image - model}{model}, \qquad (2.1)$$

where *image* is the observed surface brightness and *model* is the surface brightness derived from the fitted elliptical isophotes.

Moreover, we derived the *rms* of the sky from the sky-subtracted image of NGC 7664. We calculated the mean value and standard deviation *rms* of the surface brightness (in count pixel^{-1}) inside five square regions of 5 pixel × 5 pixel located in parts of the image where only the background is present, and we averaged these values, to obtain:

$$rms = 5.16 \text{ count pixel}^{-1}. \qquad (2.2)$$
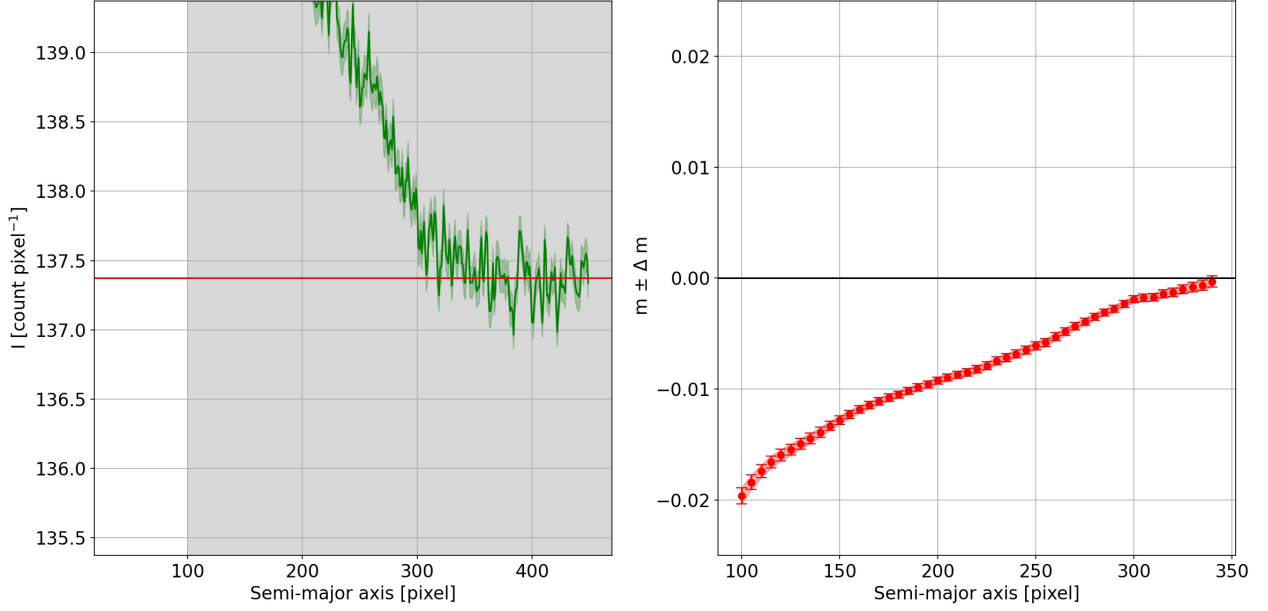
Figure 2.5: Sky level estimate from ellipse fitting of the i-band image of NGC 7664. *Left panel*: surface brightness of the fitted ellipses as a function of their semi-major axis. The red horizontal line indicates the sky level. *Right panel*: angular coefficient of the straight line that fits the ellipse surface brightness as a function of the ellipse semi-major axis with the associated errors (red points). The black horizontal line marks the null angular coefficient.

The parameters of the fitted ellipses are now used to derive the μ_i, PA, and ϵ radial profiles of NGC 7664. We converted the surface brightness from count pixel^{-1} into mag arcsec^{-2}:

$$\mu_i = -2.5 \log m + zpt_{\mathrm{mu,\,i}}, \tag{2.3}$$

where m are the count pixel^{-1} and $zpt_{\mathrm{mu,\,i}}$ is the zero point for the i-band SDSS image in units of mag arcsec^{-2}:

$$zpt_{\mathrm{mu,\,i}} = 25.88 \text{ mag arcsec}^{-2}. \tag{2.4}$$

We calculated the asymmetric errors associated to the surface brightness by first summing in quadrature the error from the ellipse fitting σ_m with the rms of the sky (Equation 2.2), to obtain:

$$\sigma_{m,\mathrm{tot}} = \sqrt{\sigma_m^2 + rms^2} \text{ count pixel}^{-1}, \tag{2.5}$$

which we converted into the upper and lower errors of the surface brightness with these formulas:

$$\sigma_{\mu,\mathrm{sup}} = |\mu_i - [-2.5 \log(m + \sigma_{m,\mathrm{tot}}) + zpt_{mu,i}]| \text{ mag arcsec}^{-2} \tag{2.6}$$

$$\sigma_{\mu,\mathrm{inf}} = |\mu_i - [-2.5 \log(m - \sigma_{m,\mathrm{tot}}) + zpt_{mu,i}]| \text{ mag arcsec}^{-2}, \tag{2.7}$$

where μ_i is the surface brightness in i band, m is the surface brightness in count pixel^{-1}, $\sigma_{m,\mathrm{tot}}$ is the luminosity error in count pixel^{-1}, and $zpt_{mu,i}$ is the i-band zero point in surface brightness given by Equation 2.4. Moreover, we calculated the mean PA and ϵ, with the associated standard deviation in the radial range that goes from 50 to 125 pixels:
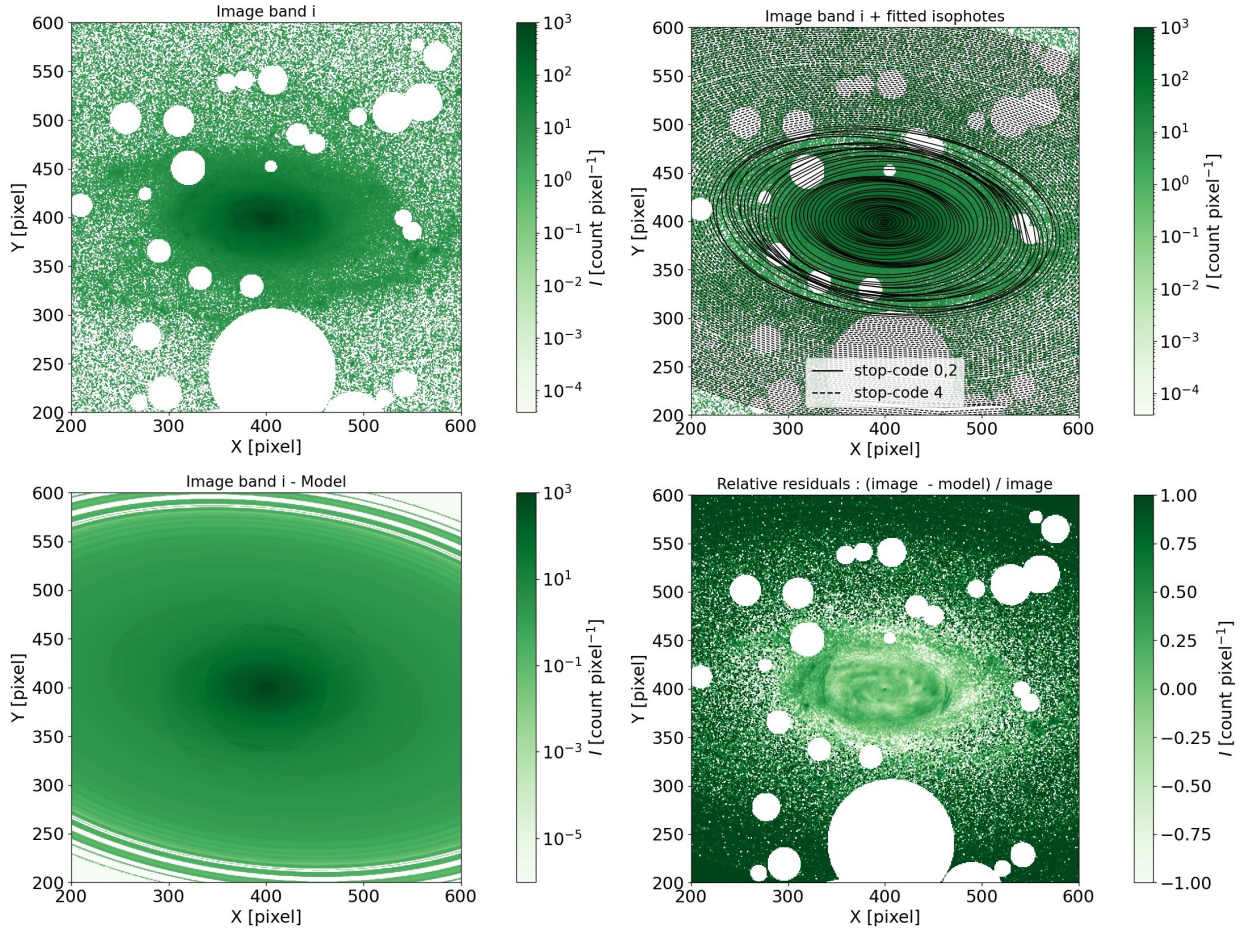
Figure 2.6: Sky-subtracted *i*-band image NGC 7664. *Top left panel:* image of the galaxy with the white circles masking the masked regions. *Top right panel:* same as the previous panel but with the fitted ellipses with stop code 0, 2 (black solid lines), and 4 (dashed lines). *Bottom left panel:* image of the galaxy derived from the model. *Bottom right panel:* map of the relative residuals.

$$\langle PA \rangle = 86.75° \pm 0.36°, \tag{2.8}$$

$$\langle \epsilon \rangle = 0.45 \pm 0.01; \tag{2.9}$$

we used this values as the mean PA and ϵ for the galactic disk of NGC 7664. The latter is slightly different from the value of $\epsilon = 0.4$ found by Kent (1985) using photometric bulge/disk decomposition. The surface brightness, PA and ϵ radial profiles of NGC 7664 are shown in Figure 2.7.

2.4   Multi Gaussian expansion photometric modelling

The ellipse fitting method to describe the surface brightness of galaxies gives us a meaningful description of a galaxy in terms of ellipticity and position angle at each radius. However, one limitation of this method is that strong deviations of the isophotes from ellipses cannot be modelled in a proper way. This makes the ellipse fitting method not well suited to photometric modelling of multicomponent objects such as lenticulars and spirals. More important, if the deviations from ellipses are not negligible, it becomes not-trivial to use the fitted isophotes for the construction of realistic dynamical models due to the complexity of the deprojection of the light distribution and evaluation of the gravitational potential. Another approach to photometric modelling that overcomes these limitations is
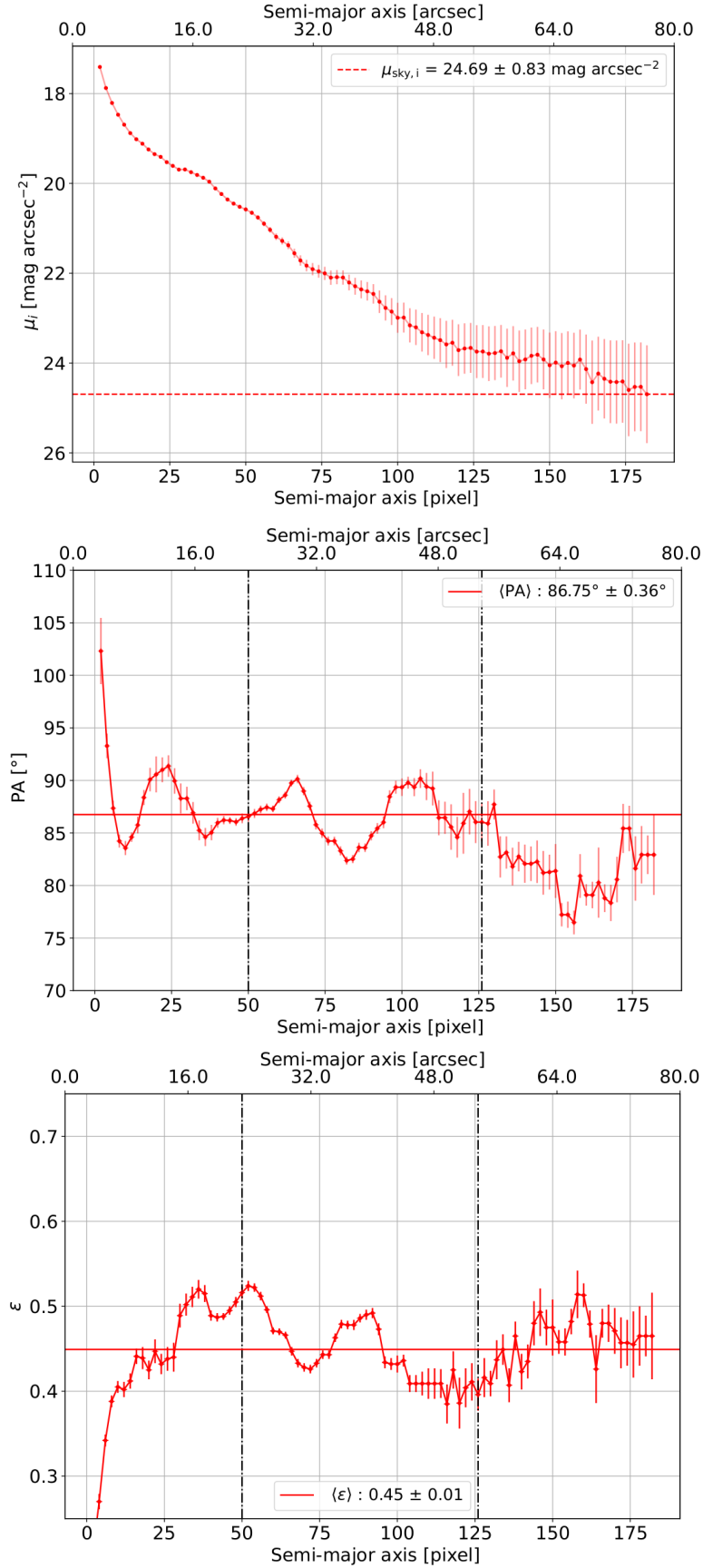
Figure 2.7: Photometric profiles from the ellipse fitting of the i-band image of NGC 7664. *Top panel*: surface-brightness radial profile with corresponding errors as a function of the ellipse semi-major axis. The horizontal red line indicates the sky surface-brightness level. *Middle and bottom panels*: PA and ϵ radial profiles with their associated errors as a function of the ellipse semi-major axis, respectively. The dotted vertical black lines indicate the region used to calculate the mean PA and ϵ of the galactic disk. The mean values are indicated by the solid red lines.

the Multi-Gaussian Expansion (MGE) method (Bendinelli, 1991; Monnet et al., 1992; Emsellem et al., 1994; Cappellari, 2002).

The MGE method consists of a series expansion of galaxy images using two-dimensional (2D) Gaussian functions. Let (x', y', z') be a system of coordinates centered on the galaxy nucleus, with the z' axis pointing towards the observer. The MGE projected surface brightness of the galaxy can be written as:

$$\Sigma(R', \theta') = \sum_{j=1}^{N} \frac{L_j}{2\pi \sigma_j'^2 q_j'} \exp\left[-\frac{1}{2\sigma_j'^2}\left(x_j'^2 + \frac{y_j'^2}{q_j'^2}\right)\right], \tag{2.10}$$

with:

$$\begin{cases} x_j' = R' \sin(\theta' - \psi_j) \\ y_j' = R' \cos(\theta' - \psi_j) \end{cases} \tag{2.11}$$

where (R', θ') are the polar coordinates on the sky plane (x', y'), N is the number of adopted Gaussian components, each of them having total luminosity L_j, observed axial ratio $0 \leq q_j' \leq 1$, dispersion σ_j' along the major axis, and PA ψ_j, measured counterclockwise from the y' axis to the major axis of the Gaussian. The results for the complete MGE model are obtained by summing the contributions over the N Gaussian components. Moreover, the MGE surface brightness has to be convolved with the instrumental point spread function (PSF) before the comparison with the observed surface brightness. The normalized PSF can be described as the sum of M circular gaussians:

$$\text{PSF}(R') = \sum_{k=1}^{M} \frac{G_k}{2\pi \sigma_k^{*2}} \exp\left(-\frac{R'^2}{2\sigma_k^{*2}}\right), \tag{2.12}$$

with $\sum_{k=1}^{M} G_k = 1$.

The total luminosity L of one Gaussian, having surface brightness Σ, does not change after convolution with the PSF $\bar{\Sigma} = \Sigma \otimes \text{PSF}$. The convolved Gaussian can be written as:

$$\bar{\Sigma}(R', \theta') = L \sum_{k=1}^{M} \frac{G_k}{2\pi \bar{\sigma}_k'^2 \bar{q}_k'} \exp\left[-\frac{1}{2\bar{\sigma}_k'^2}\left(x'^2 + \frac{y'^2}{\bar{q}_k'^2}\right)\right], \tag{2.13}$$

where:

$$\begin{cases} \bar{\sigma}_k'^2 = \sigma'^2 + \sigma_k^{*2} \\ \bar{\sigma}_k'^2 \bar{q}_k'^2 = \sigma'^2 q'^2 + \sigma^{*2k} \end{cases} \tag{2.14}$$

The resulting surface brightness distribution must be deprojected to match the observations. Generally, the deprojection is non-unique (Franx, 1988). However, the MGE deprojection represents a possible solution to the problem. If an acceptable MGE model can be obtained by fixing the PA of all the Gaussians to the same value ψ, then the object can be deprojected by assuming it is axisymmetric. In this case, once an inclination $i > 0$ is assumed for the galaxy ($i = 90°$ corresponds to edge-on), one has, for the oblate axisymmetric case:

$$q^2 = \frac{\sin^2 i}{1/q_j'^2 - \cos^2 i}, \tag{2.15}$$
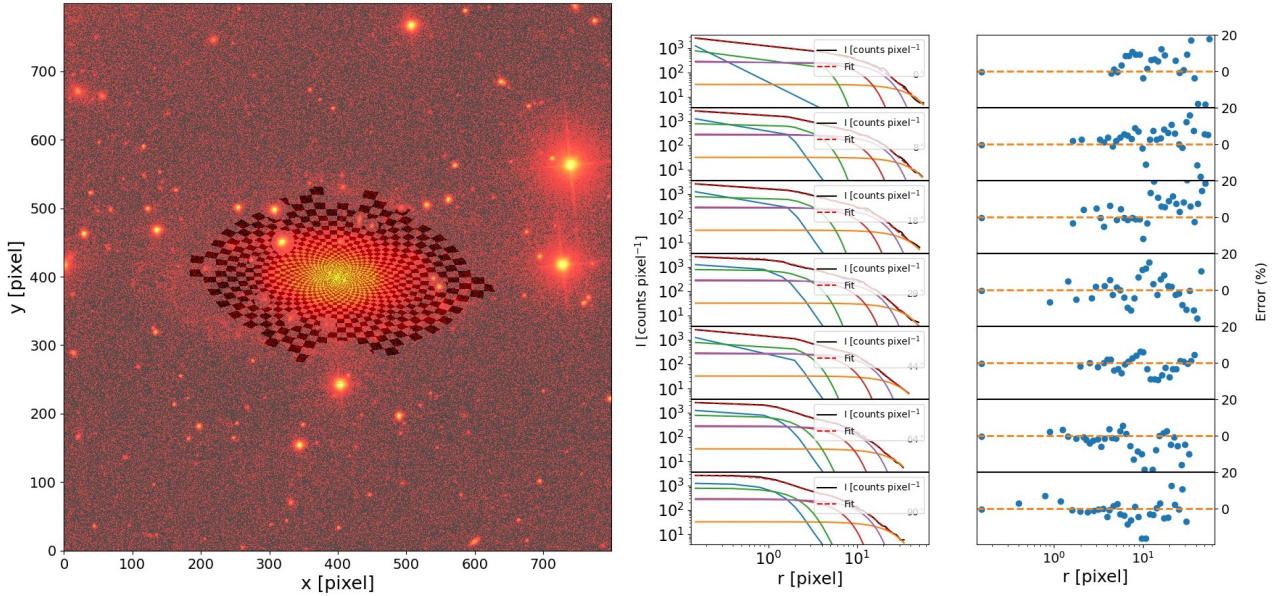
Figure 2.8: Surface brightness radial profiles from the MGE fit of the *i*-band image of NGC 7664. *Left panel*: *i*-band image with sectors. *Central panels:* comparison between the observed surface-brightness radial profiles (solid black lines) and those of the MGE model (dashed red lines). The six Gaussian components are shown (colored solid lines). Seven profiles spaced in angle between the major (upper panel) and minor (lower panel) axis are shown. *Right panels:* radial profiles of the percentage error variation of the MGE model with respect to the measured surface brightness.

which is defined only if $\cos^2 i < q_j'^2$ for all Gaussians. This means that the flattest Gaussian in an MGE fit dictates the minimum possible inclination for which the MGE model can be used in a dynamical model. However, since the Gaussian components do not necessarily have physical meaning, one does not want to base any conclusion of a dynamical model on this minimum value. Nevertheless, this minimum value $q_{\min}'$ provides a good estimate of the minimum inclination for which the galaxy, assumed to be axisymmetric, can be deprojected.

To obtain the parameters of the Gaussian components (L_j, σ_j, q_j) that best fits the data, it is necessary to interpolate the MGE model with the radial surface brightness profile, or its 2D distribution. Cappellari (2002) describes various methods to perform this, two of them are discussed here after. The first method consists in an algorithm to obtain a model for the radial profiles, while the second is the extension of the first method to the 2D case. We started by logarithmically sampling the profile in radius. This is usually done in galaxy photometry to improve the signal-to-noise (S/N) ratio at large radii, while maintaining all the information at the smaller radial scales. Then the algorithm requires the fit to optimize the relative error, namely minimize:

$$\chi^2 = \sum_{j=1}^{K} \left[\frac{C_j - \Sigma(R_j)}{C_j} \right]^2, \tag{2.16}$$

where K is the number of photometric observed data points C_j in the profile, R_j is the corresponding isophotal major axis and $\Sigma(R)$ is the 1D version of Equation 2.10.

To determine the model, we took into account that Equation 2.10 is linear in the total luminosity L_j, so with any given combination of the non linear variables σ_j, it is possible to find a simple solution to the problem. In practice, the non-linear minimization of least squares is solved for the σ_j, that must be logarithmically spaced in radius between a minimum ($R_{\min}$) and a maximum radius ($R_{\max}$) defined from the PSF and extension of the photometric data, respectively. This operation is done using the Levenberg-Marquardt method. Now, for each group of σ_j considered in the previous step, the best value for the total luminosity is found. This is a *non negative least square* problem (NNLS), that can

be solved with the algorithm developed by Lawson & Hanson (1974).

To extend the one-dimensional algorithm, defined for the radial profiles, to a 2D surface brightness distribution, it is necessary to impose that the 2D algorithm solution is the same of the 1D one. It is possible to meet this condition by fitting the MGE model in polar coordinates along a series of $N_{\rm sec}$ photometric profiles measured along sectors uniformly spaced in angle from the major to the minor axis, averaging the sectors of each quadrant. The sampling along the sectors is logarithmically spaced in the elliptical radius defined by $m'^2 = x'^2 + \frac{y'^2}{q'^2}$, where q'^2 is the isophotal axial ratio. This is fundamental because it ensures that the solution obtained by the minimization process coincides with the numerical approximation, guaranteeing that the given solution is a global minimum of the χ^2.

The MGE algorithm allows to operate a non-parametric photometric decomposition starting from the model itself, providing an efficient and robust description for the galaxy surface brightness.

2.5   Multi Gaussian expansion model of NGC 7664

We used the `python3` library `mgefit`[3], which is the implementation by Cappellari (2002) of the algorithms that produce an MGE model of the surface brightness distribution of a galaxy from its image. It requires the user only to input, in addition to the galaxy image, the coordinates of the galaxy center, PA and a range for the characteristic flattening, $q = 1 - \epsilon$, where ϵ is the ellipticity. For the input image, we used the sky-subtracted masked i-band image of NGC 7664. The input parameters requested by the `mgefit` algorithm are the mean PA and ϵ of the disk (2.8, 2.9), rms of the sky (2.2, coordinates of the galaxy center, number of sectors for the sector photometry, maximum number of Gaussians to fit, minimum and maximum values of the axial ratio allowed in the MGE fit and coordinates of a star that will be used to determine the PSF. The values of all parameters used in the MGE fitting of NGG 7664 can be found in Table 2.2. The sectors used for the photometry of NGC 7664, together with the surface brightness radial profiles taken along seven of the 19 sectors taken into account and the radial variations between the model and data are shown in Figure 2.8. The MGE fitting gives the parameters (total luminosity of the Gaussian in count, dispersion of the Gaussian in pixels and the axial ratio) of the $M = 6$ 2D Gaussian components adopted to model the surface brightness distribution of NGC 7664 (Equation 2.10). They are listed in Table 2.3. The map of the isophotes and corresponding fitted ellipses generated by the MGE model are shown in Figure 2.9.

The axial ratio q'_j is a dimensionless quantity, while the Gaussian total luminosity L_j and dispersion σ'_j are expressed in count and pixel, respectively. To be used for the dynamical modelling, these quantities must corrected and converted into physical units. The first step is converting the surface brightness from count pixel^{-1} to mag arcsec^{-2}. However, this it still represents an observed quantities and it is necessary to move from mag arcsec^{-2} to L$_\odot$ pc^{-2}.

We did the conversion from the total Gaussian luminosity in count to the observed surface brightness at the Gaussian peak C_0 in count pixel^{-1}, using the following relation:

---

[3]The `mgefit` source code is publicly available at the following link: `https://pypi.org/project/mgefit/`

Table 2.2: Input parameters of the MGE fit of the sky-subtracted i-band image of NGC 7664. The columns are: (1),(2) coordinates of the galaxy center; (3) root mean square of the sky; (4) mean position angle of the galaxy disk; (5) mean ellipticity of the galaxy disk; (6) number of sectors used for the photometry; (7) maximum number of Gaussians; (8) minimum and maximum value of the axial ratio; (9),(10) coordinates of the star used to calculate the PSF.

$x_{\rm c}$ [pixel] (1)	$y_{\rm c}$ [pixel] (2)	rms [count pixel^{-1}] (3)	$\langle$PA$\rangle$ [°] (4)	$\langle\epsilon\rangle$ (5)	$n_{\rm sec}$ (6)	$n_{\rm gauss}$ (7)	$q_{\rm bounds}$ (8)	$x_\star$ [pixel] (9)	$y_\star$ [pixel] (10)
399.56	399.28	5.16	85.75	0.45	19	30	[0.56, 1.00]	491	197

$$C_0 = \frac{L_j}{2\pi \sigma_j'^2 q_j'}. \tag{2.17}$$

At this point, we converted the surface brightness C_0 in mag arcsec^{-2} with the relation:

$$\mu_0 = -2.5 \log C_0 + zpt_{mu}, \tag{2.18}$$

where $zpt_{mu,i} = 25.883$ mag arcsec^{-2} is the SDSS i-band calibration constant in units of surface brightness that allows to pass from instrumental to observed units. Moreover, we converted the Gaussian dispersion σ_j' from pixel to arcsec. We multiplied σ_j' for the CCD angular scale $s = 0.3961$ arcec pixel^{-1}:

$$\sigma_j' \text{ [arcsec]} = \sigma_j' \text{ [pixel]} \, s. \tag{2.19}$$

The surface brightness, defined as the luminosity flux F coming from an extended source over the solid angle Ω, can be written as a function of the luminosity L and surface S of the source, as:

$$I = \frac{F}{\Omega} = \frac{L/4\pi \, d_l^2}{S/d_a^2}, \tag{2.20}$$

where I is the surface brightness in linear units, while d_l and d_a are the luminosity and angular distance, respectively. The quantities d_l and d_a are equivalent only in first approximation and in this case the surface brightness is independent from the distance of the source. In reality, these two quantities are linked to the redshift z as $d_a = d_l(1 + z)^{-2}$, because of the non-Euclidian structure of the Universe. From the previous relation, we obtained that $I \propto d_a^2 d_l^2 = (1 + z)^{-4}$. So, the observed surface brightness decreases as $(1 + z)^{-4}$ as the distance increases. We moved from the observed surface brightness to the intrinsic one by substituting C_0 with $C_{0,\text{intr}} = C_0(1 + z)^4$, where we adopted the redshift of NGC 7664 $z = 0.01159$. The Equation 2.18 becomes:

$$\mu_{0,\text{intr}} = -2.5 \log C_{0,\text{intr}} + zpt_{mu,i}. \tag{2.21}$$

An astrophysical source at redshift z, observed at a particular frequency ν_0, did not emit the photons at ν_0 but at a lower frequency $\nu = \nu_0(1+z)$. This effect can be extended to all the photometric bands. The frequency shift is caused by the cosmological redshift, associated to the particular Universe expansion dynamics, that reddens the emitted photons of the observed object. So, the observed i-band surface brightness does not coincide with the emitted one in a particular frequency. The so-called K correction is introduced to correct this effect and the Equation 2.21 becomes:

Table 2.3: Parameters of the Gaussian components of the MGE fitting of the sky-subtracted i-band image of NGC 7664. The columns are: (1) total luminosity of the Gaussian; (2) central corrected intrinsic surface brightness; (3),(4) dispersion of the Gaussian; (5) observed axial ratio.

L	I_{intr}	σ	σ	q_{obs}
[count pixel^{-1}]	[L$_\odot$ pc^{-2}]	[pixel]	[arcsec]	
(1)	(2)	(3)	(4)	(5)
4.25×10^4	1.97×10^3	1.90	0.72	1.00
5.20×10^4	6.91×10^2	4.74	1.87	0.56
7.87×10^4	4.51×10^2	7.21	2.85	0.56
4.29×10^5	3.38×10^2	19.46	7.71	0.56
9.10×10^5	2.37×10^2	33.81	13.39	0.56
5.95×10^5	2.63×10^1	79.92	31.66	0.59
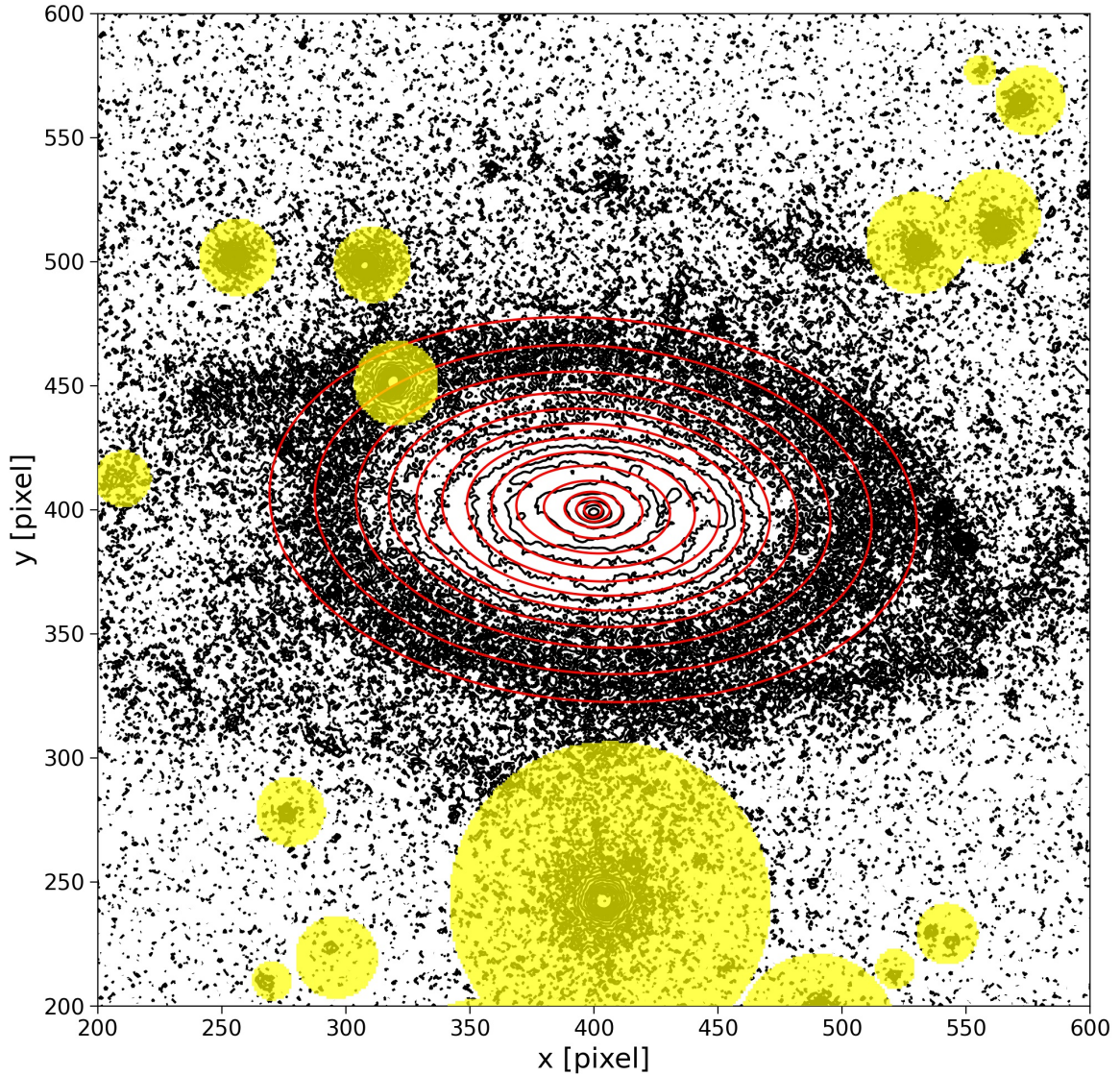
Figure 2.9: Sky-subtracted i-band image of NGC 7664 with MGE model. The MGE fitted isophotes are overplotted as red lines and the yellow circles mark the masked regions.

$$\mu_{0,\text{intr}} = -2.5 \log C_{0,\text{intr}} + zpt_{mu,i} - K_i, \qquad (2.22)$$

where $\mu_{0,\text{intr}}$ is the intrinsic surface brightness expressed in mag arcsec^{-2}, $C_{0,\text{intr}}$ is the corrected surface brightness, $zpt_{mu,i}$ is the calibration constant of the i-band photometric band in surface brightness units, and K_i is the K correction term. The K_i term depends on the redshift of the galaxy z, on the band adopted to observe it, and on the shape of its spectrum, as defined by the color index. To retrieve the value for the K correction, we used the program K-Correction Calculator[4] (Chilingarian & Zolotukhin, 2012). The chosen color index for the calculation is the value of $(g$ - $i)$ corrected for Galactic extinction in the i and g bands of the SDSS. It results $K_i = 0.01$ mag arcsec^{-2}.

The galactic extinction is another factor that must be taken into account and it is due to the surface brightness absorption caused by gas and dust in the Milky Way disk. This correction does not depend on the intrinsic properties of the object, but only on the adopted photometric band and object coordinates. To correct for the Galactic extinction, it is necessary to subtract the corresponding i-band absorption coefficient for NGC 7664, which is $A_i = 0.116$ (Schlafly & Finkbeiner, 2011). From the Equation 2.22 we obtained:

---

[4]The program is available at the following link: http://kcor.sai.msu.ru/.

$$\mu_{0,\text{intr}} = -2.5 \log C_{0,\text{intr}} + zpt_{mu,i} - K_i - A_i. \tag{2.23}$$

After these corrections, we converted the surface brightness measured in mag arcsec^{-2} to L$_\odot$ pc^{-2}. This was done using the relation:

$$I_{0,intr} = 10^{-0.4(\mu_{0,\text{intr}} - \mu_{\odot,i})}, \tag{2.24}$$

where $\mu_{0,\text{intr}}$ is the corrected intrinsic surface brightness and $\mu_{\odot,i}$ is the Sun i-band surface brightness defined by the relation:

$$\mu_{\odot,i} = M_{\odot,i} + 5 \log 206265 = 25.76 \text{ mag arcsec}^{-2}, \tag{2.25}$$

where $M_{\odot,i} = 4.19$ mag is the Sun's absolute magnitude in i band (Willmer, 2018).

The total luminosity of the fitted Gaussian components is now corrected and converted into intrinsic surface brightness $I_{0,\text{intr}}$, while the values of the dispersion are converted in arcsec. The corresponding corrected and converted results of the MGE fitting are given in Table 2.3.

Chapter 3

Spectroscopic data

In this chapter we describe how the spectroscopic data were retrieved and reduced to measure the stellar and ionized-gas kinematics of NGC 7664. In Section 3.1 we briefly describe the *Gemini North* telescope and in Section 3.2 we present the spectroscopic observations of NGC 7664. Then, in Section 3.3 we describe the steps of the spectra reduction. Lastly, in Section 3.4 we describe the procedures to extract the stellar and ionized-gas kinematics and in Section 3.5 we present the measurement of the NGC 7664 stellar and ionized-gas kinematics.

3.1 *Gemini North* telescope

The spectroscopic observations of NGC 7664 used were carried out in the first semester of 2012 with the *Gemini North* telescope at the *Gemini Observatory*. The *Gemini Observetory* consists of two twin optical/infrared telescopes. The *Gemini South* (GS) telescope is located on the Cerro Pachón in Chile. The *Frederick C. Gillet Gemini North* (GN) telescope was build on the Mauna Kea vulcano in Hawaii. From their locations on mountains in Hawaii and Chile, Gemini Observatory's telescopes can collectively access almost the entire sky. They are operated by a partnership of six countries including United States, Canada, Chile, Brazil, Argentina, and Korea.

Each telescope has a set of instruments capable of investigating the optical and infrared wavelength ranges. Many of these instruments are mounted on the Cassegrain focal point at the same time. The GN telescope has a Ritchey-Chrétien Cassegrain optical configuration and an altazimuthal mount. The primary mirror is an *f/1.8* and has a diameter of 8.1 m. while the secondary mirror has a diameter of 1.0 m. The effective focal lenght is 128.15 m (*f/16*). The field of view on the instrumental focal plane has a diameter that ranges from 7 to 10 arcmin, depending on the mounted instrument. The GN telescope is equipped with an adaptive optics (AO) system that corrects image blurring due to atmospheric turbulence in the infrared bands and produces images nearly at the diffraction limit.

The spectrograph used to obtain the long-slit spectra of NGC 7664 is the *Gemini Multi-Object Spectrograph* (GMOS), mounted on the GN telescope (Hook et al., 2004). The optical configuration and spectrograph structure are shown in Figure 3.1. The GMOS spectrograph is able to perform long-slit spectroscopy in the spectral range 3600-9400 Å, multi-object spectroscopy, and images with a field of view larger than 5.5 arcmin^2. It is also equipped with an integral field unit (IFU), that uses 0.2 arcsec fibers to obtain spectra from an area larger then 35 arcsec^2. GMOS was build thanks a collaboration between the *Astronomy Technology Center* in Edinburg, the *Duhram University* in Great Britain, and the *Herzberg Institute of Astropyhsics* in Canada. The spectrograph is equipped with three CCDs of 2048 × 4608 pixel each. The spaces between the CCDs produce small blind gaps in the wavelength sampling of 2.8 arcsec (39 pixel), whose dimension in Å depends on the grating used in the observation. The CCD properties are reported in Table 3.1 and 3.2.

The available slits which can be used on the GMOS spectrograph are IFU-2, IFU-R, 0.25, 0.5, 0.75, 1.0, 1.5, 2.0, 5.0, NS0.75, and NS1.0, while the gratings are B1200/G5301, R831/G5302, B600/G5303,
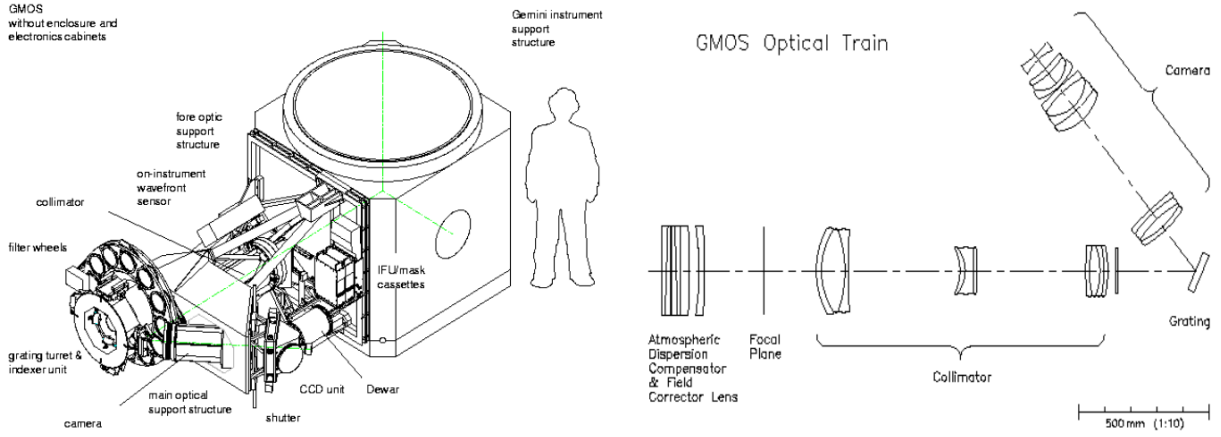
Figure 3.1: The GMOS instrument. *Left panel:* layout of GMOS. *Right panel:* optical configuration of GMOS.

B600/G5304, R400/G5305, and R150/G5306. The information on the available gratings are listed in Table 3.3, while the corresponding efficiency curves are shown in Figure 3.2.

3.2 Spectra acquisition

The spectroscopic observations of NGC 7664 were obtained using the B1200/G5301 grating in combination with the slit of width $L = 0.75$ arcsec. The instrumental velocity dispersion of the observation can be calculated using the formula:

$$\sigma_{\mathrm{instr}} = \frac{W}{0.5} \frac{c}{2.355R} \ \mathrm{km\,s^{-1}}, \tag{3.1}$$

where W is the slith width in arcsec, $c = 299792 \ \mathrm{km\,s^{-1}}$ is the speed of light and R $= 3744$ is the resolution of the grating. The value obtained for the 0.75 arcsec slit is $\sigma_{\mathrm{instr}} = 50 \ \mathrm{km\,s^{-1}}$. The $L = 5.5$ arcmin slit is sufficiently long to cover all the galaxy extension, that has a diameter of $D_{25} = 2.5$ arcmin (de Vaucouleurs et al., 1991). There is also enough space to estimate the sky background from the outer regions of the spectra. The wavelength range of the B1200/G5301 grating has an extension of 1430 Å. The chosen central wavelength was 4700 Å, to study the interval between 4000 and 5400 Å. So, the spectra will contain the emission lines of H$\beta\lambda$4861.32Å and [OIII]$\lambda\lambda$4958.83, 5006.77Å. To obtain good spectra we need a signal-to-noise ratio S/N $= 50$ for every element of spectra resolution in the region of the galactic disk, therefore the observation was divided in more frames. For this reason, 8 spectra of NGC 7664 with exposure time $t_{\mathrm{exp}} = 2000$ s were taken, four for the major axis and four for the minor one. For the major axis, the slit was positioned with a position angle PA $= 270°$, while for the minor axis the slit position angle was PA $= 0°$. In addition to that, a series of calibration images were taken. They were obtained with the same instrumental setup of the galaxy spectra. The

Table 3.1: Properties of the detector mounted on GMOS spectrograph. The rows are: (1) name of the detector; (2) total area; (3) configuration of the CCD on the detector; (4) size of the pixels; (5) angular scale of the pixel; (6) spectral range (Hook et al., 2004).

Equipment	(1)	e2v DD ML2AR CCD42-90-1-F43
Size	(2)	6144×4608 pixel
Configuration	(3)	3 CCDs of 20485×4608 in line
Pixel size	(4)	13.5 μm^2
Pixel scale	(5)	0.0728 arcsec pixel^{-1}
Spectral range	(6)	3600 - 10300 Å

bias images are very stable, so they can be taken once a month and used for the calibration when needed. In this case, 21 *bias* images were available. The *flatfield* images were taken with the *Gemini Facility Calibration Unit* (GCAL), that supplies light sources with constant emission and absorption lines to be used for *flatfield* and wavelength calibrations, respectively. For this series of observations, about 30 *flatfield* images were taken using a quartz-tungsten halogen lamp and about 10 spectra using a copper-argon lamp were used.

For the flux calibration of the spectra taken with GMOS, it is necessary to observe a standard spectrophotometric star. For observations in the wavelength range between 3200 and 8100 Å the standard stars are usually selected from the catalog of Massey et al. (1988). In this case the standard star was Wolf 1346 with spectral type DA, characterized by an absolute magnitude $M_V = 11.54$ mag, a color $(B - V) = -0.07$ mag, and an apparent magnitude at $\lambda = 5556$ Å equal to $m_{\lambda 5556} = 11.59$ mag (Massey et al., 1988). Three spectra of Wolf 1356 with exposure time $t_{\exp} = 150$ s and the same instrumental setup of the galaxy spectra were obtained.

3.3 Spectra reduction

The spectra reduction was performed by Cuomo (2015) with dedicated routines written for the software IRAF[1]. The images have a dimension of 6144×4608 pixel. The wavelength dispersion direction is along the image rows (x axis), while the spatial direction is along the rows (y axis). The wavelength increases from right to left. The preliminary reduction was performed using the IRAF package `Gemini-GMOS`[2].

3.3.1 *Masterbias* creation

The *bias* is a threshold value introduced by the electronic that reads the CCD. This value is added to the luminous signal coming from the celestial sources and need to be subtracted. The *bias* images are obtained with exposure time of zero seconds, closed shutter, and lights off to avoid any light contamination. The *bias* images are affected by the read-out noise (RON), that increases the noise of the science frames. To minimize this noise, it is necessary to acquire many *bias* images and build the mean image, the so-called *masterbias*, that has noise:

$$N_{\mathrm{masterbias}} = \frac{N_{\mathrm{bias}}}{\sqrt{n}}, \tag{3.2}$$

where n is the number of *bias* images and N_{bias} is the noise of every single bias image (that is equal to the RON of the CCD). The noise of the bias-subtracted science frame is:

$$N_{\mathrm{image-masterbias}} = \sqrt{N_{\mathrm{bias}}^2 + N_{\mathrm{image}}^2}, \tag{3.3}$$

---

[1]IRAF is distributed by the *National Opical Astronomy Observatories* (NOAO), managed by the *Association of Universities for Research in Astronomy* (AURA), Inc. in collaboration with the *National Science Foundation* (NSF). It is available at the following link: `http://iraf.noao.edu/`.

[2]The IRAF package devoted to the reduction of *Gemini Observatory* data is available at the following link: `http://www.gemini.edu/sciops/data-and-results/processing-software`.

Table 3.2: Gain and read-out noise of the CCDs of GMOS. The column are: (1) reading speed; (2) gain; (3) read-out noise. (Hook et al., 2004)

Reading	Gain	Noise
	[e⁻ ADU⁻¹]	[e⁻ rms]
(1)	(2)	(4)
slow	2.27	3.32
fast	5.27	6.5
fast	2.49	4.2

the IRAF command `gbias` was used to calculate the *masterbias* from the single *bias* image, in order to subtract it from the NGC 7664 and other calibration frames.

3.3.2 *Masterflat* creation

Since the different pixels in the CCD present small quantum efficiency differences, it is necessary to uniform the relative response of each pixel as much as possible. To do that, some *flatfield* images are used. These calibration images are the spectra of an homogeneous luminous source, like the one produced by a lamp or a screen placed in the telescope dome, and from the crepuscolar light coming from a portion of sky without stars. These images have short exposure time to not saturate the CCD. From their analysis, it is possible to distinguish the regions of the CCD that are more or less sensitive. The science frames must be divided by the *flatfield*, which must be normalized since it corrects the percentage non-uniformities of the CCD response. To be normalized, the *flatfield* is divided by its mean value. In order to minimize the noise coming from the *flatfield* correction and maximize its S/N, many *flatfield* images are required. These images are averaged together to create the *masterflat*. The noise decreases like the one of the *masterbias* (Equation 3.3). The IRAF command `gsflat` was used to calculate the *masterflat* to calibrate the NGC 7664 spectra.

3.3.3 *Bias* and *flatfield* corrections

Once the *masterbias* and *masterflat* images were obtained, the *bias* and *flatfield* corrections were applied to all the spectra. These corrections were done using the IRAF commands `gsreduce` (that subtracts the images for the *masterbias* and divide them for the *flatfield*), `gireduce` (that multiplies the images for the gain of the CCD), and `gmosaic` (that interpolates the gaps between the CCDs).

3.3.4 Wavelength calibration

Because of the deformations caused by the telescope and instrument optics, the spectra result to be curved. The wavelength calibration consists in finding a function to convert from the pixel space (x, y) to the wavelength space (λ, y). Indeed, because of the curvature, the wavelength is function of both the x and y coordinates. So, it is necessary to map the spectra using an interpolating polynomial and measure the dispersion relation that associates each pixel to a given wavelength. This is done using a series of copper-argon lamp calibration spectra. The IRAF commands `gswavelength`, `gsappwave`, and `fitcoords`, were used to obtain the dispersion relation for the calibration spectra. An example of wavelength calibration on a calibration lamp is shown in Figure 3.3.
The IRAF command `gstransform` is used to apply the wavelength calibration function to the science frames of NGC 7664.

Table 3.3: Properties of the gratings of GMOS. The column are: (1) name of the grating; (2) number of the grating; (3) density of the lines; (4) blaze wavelength; (5) spectral resolution (6) wavelength range; (7) dispersion (Gimeno et al., 2016).

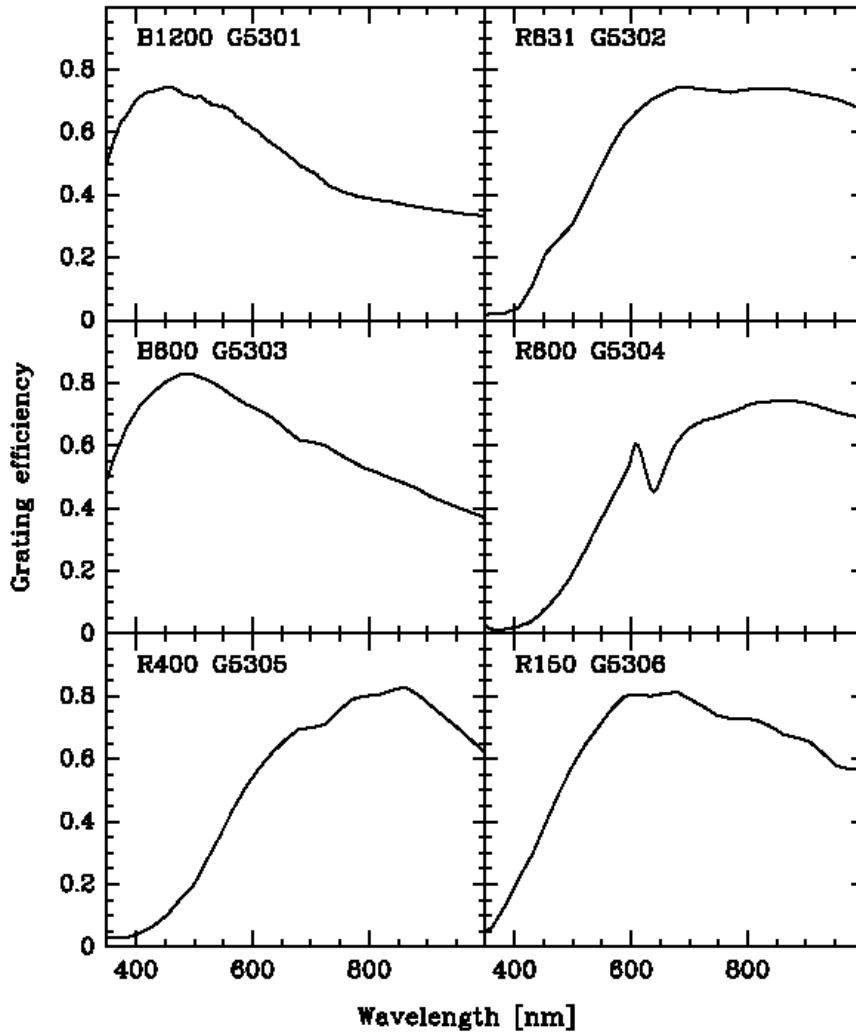| Name	Number	Line density [lines mm^{-1}]	λ_b [nm]	R	Simultaneous coverage [nm]	Dispersion [nm pixel^{-1}]
(1)	(2)	(3)	(4)	(5)	(6)	(7)
B1200	G5301	1200	463	3744	143	0.023
R841	G5302	831	757	4396	207	0.034
B600	G5303	600	461	1688	276	0.045
R600	G5304	600	926	3744	286	0.047
R400	G5305	400	764	1918	416	0.067
R150	G5308	150	717	631	1071	0.174

Figure 3.2: Efficiency curves of the GMOS gratings. The response of the B1200/G5301 (*top left panel*), R831/G5302 (*top right panel*), B600/G5303 (*middle left panel*), R800/G5304 (*middle right panel*), R400/G5305 (*bottom left panel*), and R150/G5308 (*bottom right panel*) gratings is shown as a function of the wavelength (Gimeno et al., 2016).

3.3.5 Spectra combination and cosmic ray correction

To increase the S/N of the scientific spectra, it is useful to combine together more spectra of the same galaxy, obtained in the same position and with the same slit orientation. This step can be done with the IRAF command `gemscombine`, that also correct the frames for cosmic rays. Indeed, the electrons generated by the observed photons from astrophysical objects are present as well as the contribution of high energy particles, like protons and α particles, with energies between 10^6 and 10^{20} eV. They interact with the detector and creates spurious counts, called cosmic rays, in random pixels. To avoid that the cosmic rays count saturate the image, the observations are divided in different frames with relatively short exposure time.

For NGC 7664, four spectra along its major axis and four along the minor one were taken. The two axis correspond to two different position angles of the GMOS slit. For the major axis, the slit was oriented with PA = 270°, and for the minor axis it was PA = 0°. Then, the command `gemcombine` calculates the mean of the four spectra and interpolates the pixel where the cosmic rays are present. For every axis, we obtain the cosmic-ray corrected final spectrum, characterized by a factor two improved S/N ratio.
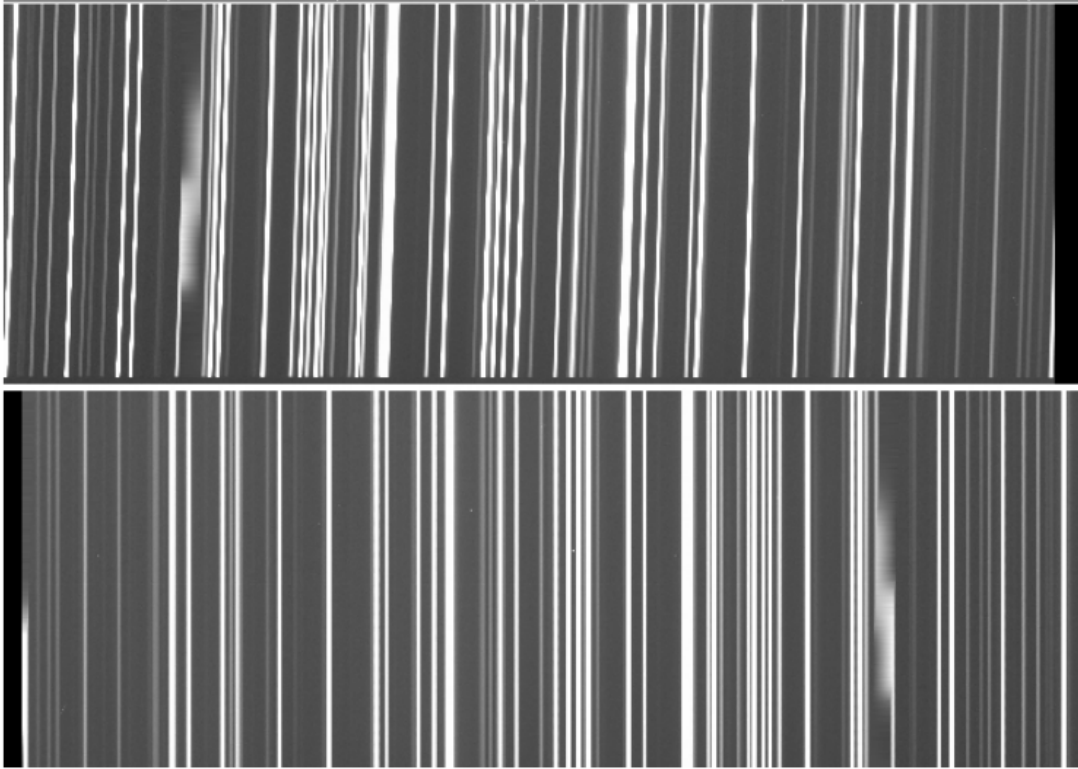
Figure 3.3: Example of wavelength calibration of the GMOS spectra. A region of a calibration lamp spectrum before (*upper panel*) and after (*bottom panel*) the wavelength calibration (Cuomo, 2015).

3.3.6   Sky subtraction

The galaxy spectra shows emission and absorption lines due to the sky contribution that must be recognized and subtracted. The first step is to identify the radial intervals where only the sky signal is present. Then, the IRAF command `gsskysub` is used to fit the sky trend and subtract it from all the wavelength-calibrated spectra. An example of a galaxy spectrum before and after the sky subtraction is shown in Figure 3.4.

3.3.7   Flux calibration

The last reduction step of the galaxy spectra is the flux calibration. This is done by determining the instrument response function in order to convert the flux from instrumental units (count) to physical units (erg cm^{-2} sec^{-1} Å^{-1}), removing the non-uniformity of the CCD response at different wavelengths. To build this function, it is necessary to use the spectra of a standard spectrophotometric star, whose flux is known and tabulated as a function of the wavelength. The ratio between the measured and tabulated flux allows to create the response function. The star used to flux calibrate the NGC 7664 spectra is Wolf 1346. Its three available spectra were calibrated with the same procedure presented in the previous paragraphs. After the reduction, they can be used for the flux calibration. The first step consists in extracting the star one-dimensional spectra from the 2D one using the IRAF command `gsextract`. Then, with the command `gsstandard`, the instrument response function is created. The command `sensfunc` calculates the ratio between the observed and tabulated flux and interpolates this ratio in a proper way over the full spectral range. Lastly, the command `gscalibrate` applies the instrument response function to the NGC 7664 spectra, that are therefore flux calibrated.
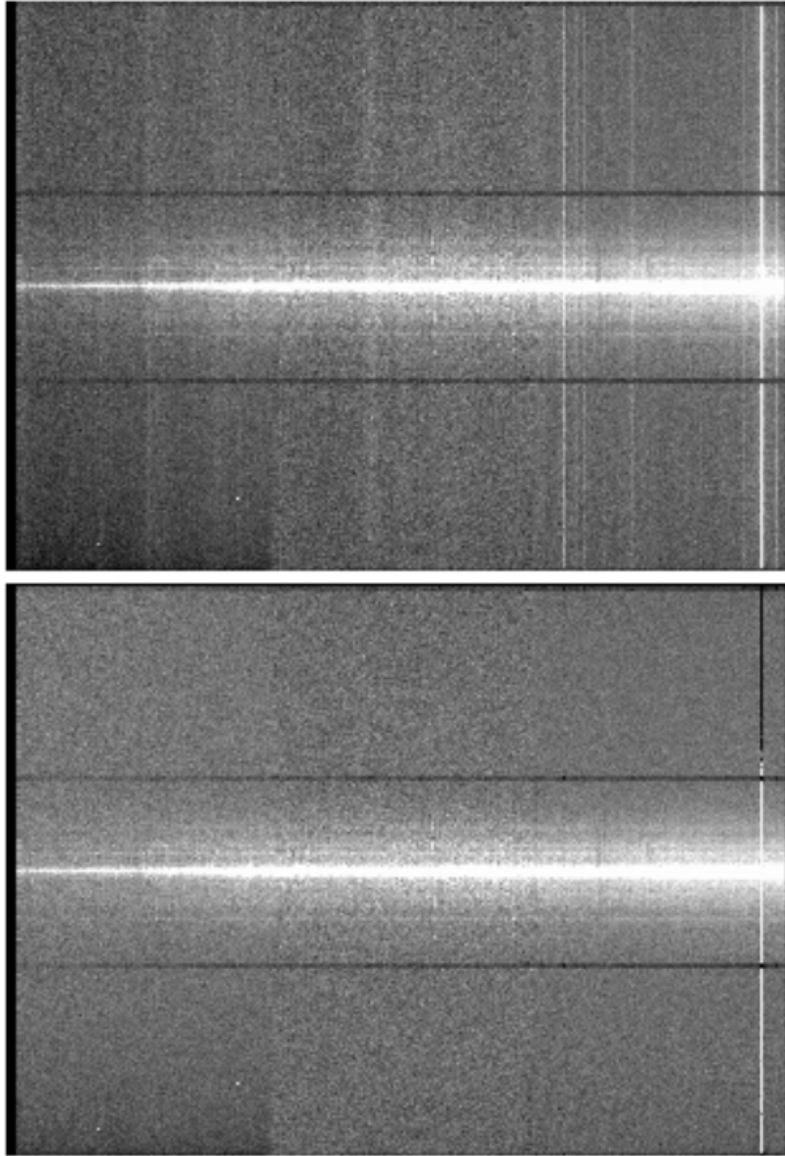
Figure 3.4: Example of sky subtraction of the GMOS spectra. Comparison between the galaxy spectrum galaxy before (*top panel*) and after (*bottom panel*) the subtraction of the sky sky contribution (Cuomo, 2015).

3.4   Stellar and ionized-gas kinematics

To measure the stellar and ionized-gas kinematics of NGC 7664, Cuomo (2015) used the following IDL programs:

- `snratio`, sums the adjacent lines of the reduced galaxy spectrum, to obtain a final spectrum whose rows have a fixed S/N;

- `gandalf`, simultaneously measures the kinematics of the stars and ionized gas;

- `pPXF`, is used by `gandalf` to measure the stellar kinematics.

3.4.1   `snratio` procedure

The IDL procedure `snratio` was written by L. Morelli. It generates a spectum, whose rows are the sum of several adjacent rows of the starting spectrum to ensure a fixed minimum S/N in each row of the final spectrum. This procedure is necessary since the actual S/N of the spectrum is not known

and the errors on the stellar kinematic parameters depend on this ratio. The estimation of the signal S is done in the row, while the estimation of the noise N is done by measuring the *rms* of the counts in external regions of the spectra. The final spectrum is assembled and given as output by summing the rows until the final S/N ratio reaches the target value of S/N = 20.

3.4.2   `gandalf` procedure

To extract the kinematics from the long-slit spectra along the major and minor axis of NGC 7664, the IDL program *Gas AND Absorption Line Fitting* (`gandalf`[3] , Sarzi et al., 2006) was used. This is a direct interpolation code that separates the relative contribution of the stellar continuum from the ionized gas emission in the galaxy spectra, while measuring at the same time the stellar and ionized-gas kinematics. This is generally done in two steps. The first step is to interpolate the stellar continuum, masking the spectral regions which are potentially contaminated by the emission lines coming from the gas. Then, the gas emission lines are measured from the residual spectra coming from the interpolation. The stellar continuum and kinematics of the stellar component are measured with a linear combination of stellar spectra used as reference templates. This combination is then convolved with the stellar line-of-sight velocity distribution (LOSVD) using the program *Penalized Pixel Fitting* (`pPXF`[4], Cappellari & Emsellem, 2004). The ionized-gas emission and kinematics are derived by assuming a Gaussian LOSVD.

3.4.3   `pPXF` procedure

If we imagine the galaxies as systems composed entirely by stars, their observed spectra in a certain region of the sky are the weighted sum of single star spectra which are redshifted or blueshifted, according to the galaxy velocity along the line of sight. Assuming that the spectra of all the stars are given by a single template spectrum or the linear combination of some of them it is necessary to convolve the template spectra with the LOSVD to reconstruct the spectrum of a galaxy. On the other hand, we can solve the inverse problem by deconvolving the galaxy spectrum using the template ones and derive the LOSVD of the stars. Many techniques were developed to derive the LOSVD from the spectra of galaxies. The most recent ones are based on the direct interpolation of the LOSVD on the pixel space (e.g. Rix & White, 1992; van der Marel, 1994; Gebhardt et al., 2000). The motivations for this choice (Cappellari & Emsellem, 2004) are that:

- in the pixel space, it is easy to mask the ionized-gas emission lines and bad pixels. In this way, only the stellar absorption lines can be considered;

- the present-day computer can manage the needed computational time;

- the availability of high-resolution libraries of stellar spectra allows an accurate comparison with galacy spectra.

The different techniques are also divided according to the type of adopted LOSVD, that can be non-parametric or parametric. The method proposed by Cappellari & Emsellem (2004) falls into this last category, working in the pixel space and adopting a LOSVD described by the parameterization with Gauss-Hermite polynomials by van der Marel & Franx (1993) and Gerhard (1993).

The parametric recovery of the LOSVD in pixel space starts with the creation of a galaxy model spectrum $G_{\mathrm{mod}}(x)$ by convolving a template spectrum $T(x)$ with a parametrized LOSVD. Both the galaxy and template spectra are rebinned in wavelength to a linear scale $x = \ln \lambda$, while preserving the number spectral pixels. The best-fitting of the parametrized LOSVD are determined by minimizing the χ^2, that measures the agreement between the observed galaxy spectra and the model spectrum over a set of N pixels:

---

[3]The `gandalf` program can be retrieved at the following link: `https://www.strw.leidenuniv.nl/sauron/software.html`.

[4]The `pPXF` program can be retrieved at the following link `http://www-astro.physics.ox.ac.uk/~cappellari/idl/#ppxf`.

$$\chi^2 = \sum_{n=1}^{N} r_n^2 = \sum_{n=1}^{N} \frac{G_{\mathrm{mod}}(x_n) - G(x_n)}{\Delta G(x_n)}, \tag{3.4}$$

where r_n are the residuals, and $\Delta G(x_n)$ the measurement errors on the observed spectrum $G(x_n)$. Moreover, the following model is adopted for the galaxy spectrum:

$$G_{\mathrm{mod}}(x) = \sum_{k=1}^{K} w_k [B \otimes T_k](x) + \sum_{l=0}^{L} b_l P_l(x) \qquad w_k \geq 0, \tag{3.5}$$

where T_k is a library of K galaxy or stellar templates, w_k are the weights, $B(x) = L(cx)$ is the broadening function where $L(v)$ is the LOSVD and c is the speed of light. The symbol $\otimes$ denotes the convolution. $P_l(x)$ are chosen to be the Legendre polynomials of orded l and account for low-frequency differences in the spectral shape between the galaxy and templates. In this case we are interested in the determination of the parameters that defines $L(v)$. Therefore we assume that the weights of Equation 3.5 are always optimized in this way. To describe the LOSVD, it has become standard to expand it as a Gauss-Hermite series (van der Marel & Franx, 1993; Gerhard, 1993):

$$L(v) = \frac{e^{-0.5y^2}}{\sigma \sqrt{2\pi}} \Big[1 + \sum_{m=3}^{M} h_m H_m(y) \Big], \tag{3.6}$$

where $y = (v - V)/\sigma$ and H_m are the Hermite polynomials.

With these definitions the minimization of the χ^2 in Equation 3.4 is a non-linear optimization problem for the M parameters $(V, \sigma, h_3,...,h_m)$ of the LOSVD. This is solved using the Levenberg-Marquardt method for non-linear least-squares problems. The galaxy LOSVD is in first approximation generally well reproduced by a Gaussian function (Bender et al., 1994). For this reason, when the S/N is large, the LOSVD is interpolated with a technique in which the solution is free to reproduce the details of the velocity profile, while, when the S/N is small, it approaches to a Gaussian shape. In this case, this formalism is applied to the situation in which the LOSVD is parametrically expanded as a Gauss-Hermite series.

The idea is to simultaneously interpolate the $(V, \sigma, h_3,..., h_m)$ parameters, but adding a penalizing term adaptable to χ^2 to try to bring the solution towards a Gaussian shape. The penalized χ^2 can be written as:

$$\chi_p^2 = \chi^2 + \alpha P, \tag{3.7}$$

where P is the penalty function and α is the penalty factor. A natural form for P is given by the integrated square deviation of the line profile $L(v)$ from its best-fitting Gaussian $G(v)$:

$$D^2 = \frac{\int_{-\infty}^{\infty} [L(v) - G(v)]^2 dv}{\int_{-\infty}^{\infty} G(v)^2 dv}. \tag{3.8}$$

This penalty does not suppress noisy dominated solutions, which are already excluded by the use of low-order parametric expansion of $L(v)$. It was shown by van der Marel & Franx (1993) that in the case that $L(v)$ has the form of Equation 3.6, the previous equation is well approximated by:

$$D^2 \simeq \sum_{m=3}^{M} h_m^2. \tag{3.9}$$

Cappellari & Emsellem (2004) found a simple solution to optimize the non-linear least squares minimization which consists in using the following perturbed residuals as input:

$$r'_n = r_n + \lambda\sigma(r)D, \tag{3.10}$$

where the variance σ is defined as:

$$\sigma^2(r) = \frac{1}{N}\sum_{n=1}^{N}r_n^2. \tag{3.11}$$

The qualitative interpretation of this formula is that a deviation D of the LOSVD from a Gaussian shape will be accepted as an improvement of the fit only if it is able to correspondingly decrease the scatter $\sigma(r)$ by an amount related to D. To quantify this, one can compute the objective function of the fit:

$$\chi_p^2 = \sum_{n=1}^{N}r_n^2 + 2\lambda\sigma(r)D\sum_{n=1}^{N}r_n + N[\lambda\sigma(r)D]^2. \tag{3.12}$$

The sum of the second term residuals is zero by construction, because of the fact that weights are optimized for a given $L(v)$. So, considering the definition of variance, one can write:

$$\chi_p^2 = \chi^2(1 + \lambda^2 D^2), \tag{3.13}$$

which is the desired form of Equation 3.7 with $\alpha = \lambda^2 D^2$ which automatically scales according to the χ^2 of the fit.

In summary, the algorithm structure is the following:

1. it starts providing the input values for the parameters (V, σ), while putting the initial Gauss-Hermite parameters $h_3, ..., h_M = 0$;

2. the sub-problem of Equation 3.5 is solved for the weights $(w_1, ..., w_k, b_0, ..., b_t)$;

3. the residuals r_n are calculated from interpolation using Equation 3.4;

4. the residuals are perturbed as in Equation 3.10 to obtain r'_n;

5. the perturbed residuals r'_n are provided in a optimization cycle for the non-linear least squares, iterating the procedure from the step 2 to interpolate the parameters $(V, \sigma, h_3, ..., h_M)$.

3.5   Measurement of the stellar kinematics

To measure the stellar kinematics of NGC 7664, Cuomo (2015) used a set of stellar spectra from the library ELODIE (Prugniel & Soubiran, 2001; Moultaka et al., 2004). This contains high-resolution spectra ($R \sim 10000$) obtained with the ELODIE spectrograph, mounted on the 1.93 meters telescope at the *Observatorie de Haute-Provence*. The available 1963 stellar spectra cover the spectral region that goes from 4000 to 6800 Å and were obtained from stars with different atmospheric parameters (T_{eff} between 3000 and 60000 K, $\log g$ between -0.3 and 5.9, and [Fe/H] between -3.2 and +1.4). After extensive testing, 25 ELODIE stars were used to derive the NGC 7664 stellar kinematics. From the output data of `gandalf`, the stellar kinematics was extracted using the IDL program `extr_kin`, written by L.Morelli. The spectrum taken with the slit at the position angle PA = 270° was used to derive the stellar kinematics along the major axis, while the slit was rotated with a position angle PA = 0° for the minor axis.
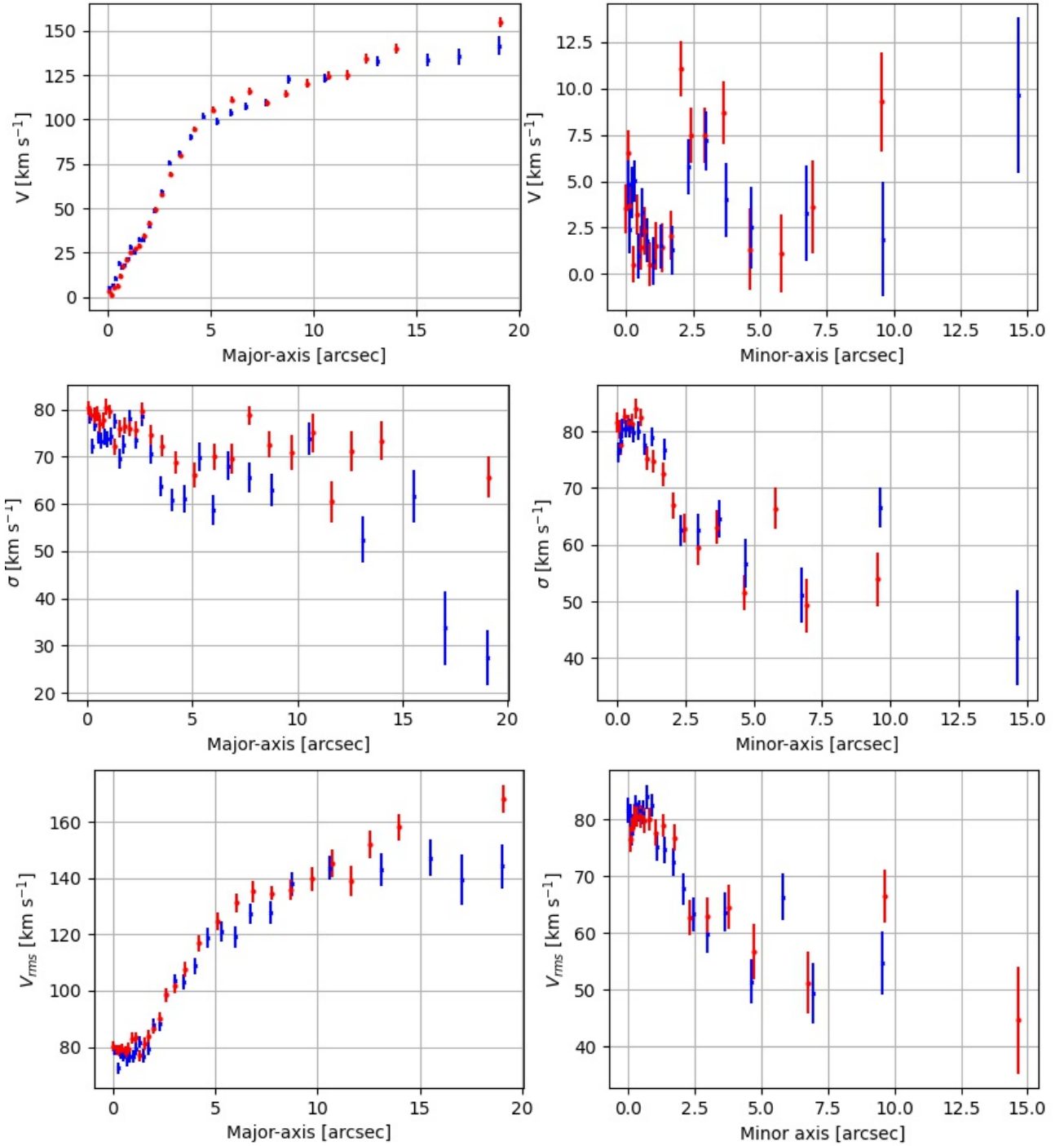
Figure 3.5: The stellar kinematics of NGC 7664. The kinematic radial profiles obtained along the major (*left panels*) and minor axis (*right panels*) are shown. The red dots and blue crosses refer to the data measured along the receding and approaching side, respectively. The LOS velocity V after the subtraction of the system velocity (*top panels*), velocity dispersion σ (*middle panels*), corrected for the instrumental velocity dispersion and root mean square velocity V_{rms} (*bottom panel*) radial profiles are shown.
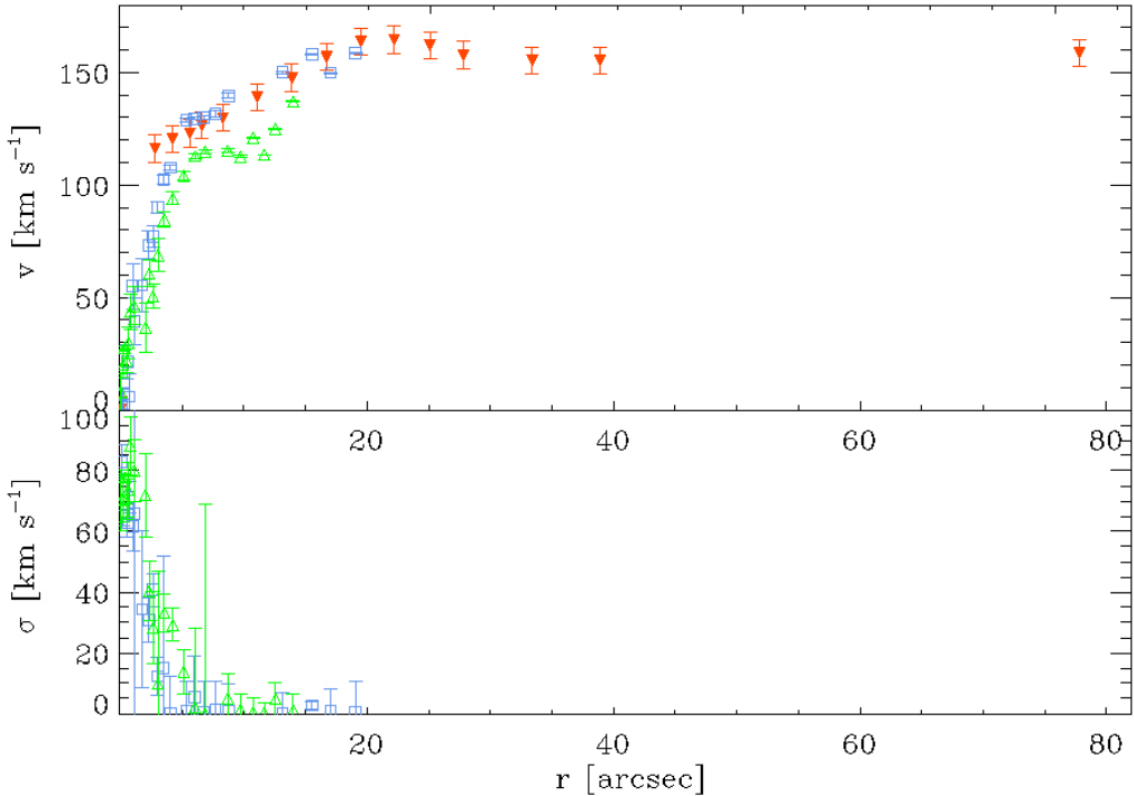
Figure 3.6: Ionized-gas kinematics measured along the major axis of NGC 7664. The LOS velocity v, after the subtraction of the system velocity (*top panel*) and LOS velocity dispersion σ (*bottom panel*) are symmetrized with respect to the galaxy center. The empty symbols are the measurements by Cuomo (2015), while the triangles correspond to the measurements by Rubin et al. (1980). The green triangles and blue squares refers to the data measured along the receding and approaching side, respectively (Cuomo, 2015).

We symmetrized the rotation curve and velocity dispersion profile along both axis with respect to the center. With a `python3` script, we rewrote $R = |r - r_s|$ and $V = |v - v_s|$, where r_s is the radius of the system center, and v_s is the system velocity, obtained from the mean radial velocities. In this way, R represents the distance from the galaxy center. For NGC 7664, the resulting system velocity is $v_s = 3462$ km s^{-1}. On the other hand, the velocity dispersion profile was simply reflected with respect to the origin $\sigma = |\sigma(r - r_s)|$. Then we calculated the root mean square velocity radial profiles, defined as:

$$V_{\mathrm{rms}} = \sqrt{V^2 + \sigma^2}. \tag{3.14}$$

The stellar kinematics V, σ and V_{rms} radial profiles obtained along the NGC 7664 major and minor axis are shown in Figure 3.5.

As it can be seen from the profiles, the measurements on the major axis extend up to $|r| \simeq 19$ arcsec. The rotation curve reaches a value of $V \simeq 130$ km s^{-1} at $R \simeq +12$ arcsec and then it remains constant outwards. The velocity dispersion has a central value of $\sigma \simeq 80$ km s^{-1} and it decreases until it reaches the value of $\sigma \simeq 40$ km s^{-1}. The V_{rms} profile has a central value of $V_{\mathrm{rms}} \simeq 80$ km s^{-1} and reaches a value of $V_{\mathrm{rms}} \simeq 150$ km s^{-1} at $R \simeq +12$ arcsec and then it remains almost constant outwards. The measurement on the minor axis extend up to $|r| \simeq 15$ arcsec. The rotation velocity is $V \simeq 0$ km s^{-1}, with a maximum value of $V \simeq 11$ km s^{-1}. at $R \simeq +12$ arcsec and then it remains constant outwards. The velocity dispersion has a central value of $\sigma \simeq 80$ km s^{-1} and it decreases until it reaches the value of $\sigma \simeq 40$ km s^{-1}. The V_{rms} profile has a central value of $V_{\mathrm{rms}} \simeq 80$ km s^{-1} and decreases down to a value of $V_{\mathrm{rms}} \simeq 40$ km s^{-1}.

In both the two axes, the values of V refer to observative measures. This means that they are not corrected for PA and inclination of the galaxy i. On the other hand, the values of σ are corrected for the instrumental dispersion σ_{inst}.

3.5.1   Measurement of the ionized gas kinematics

Cuomo (2015) also measured the kinematics of the ionized gas component along the major axis of NGC 7664. This was done starting from the output files that contains the ionized-gas emission and kinematic parameters produced by `gandalf`. They were analyzed with the IDL program `extr_gas_kin` written by L. Morelli. The kinematics can be obtained from the different emission lines produced by the ionized gas. In this case, the available emission lines that can be used to extract the ionized gas kinematics were H$\beta\lambda$4861.32Å, and [OIII]$\lambda\lambda$4958.83, 5006.77Å. The latter is a doublet and the associated errors were larger. For this reason, Cuomo (2015) chose to construct the ionized-gas rotation curve obtained from the H$\beta\lambda$4861.32Å line only. Moreover, this rotation curve was compared with the results of Rubin et al. (1980). They used the emission lines of H$\alpha\lambda$6562.81Å and of [NII]$\lambda\lambda$6548.03, 6583.41Å to measure the ionized-gas velocity. The two ionized-gas kinematics are similar to each other and they are shown in Figure 3.6.

As it can be seen from the ionized-gas profile, the measurements of Cuomo (2015) extend up to $|r| \simeq 19$ arcsec, while the ones of Rubin et al. (1980) extend up to $|r| \simeq 78$ arcsec. The rotation curve reaches a value of $V \simeq 150$ km s^{-1} at $R \simeq +15$ arcsec and then it remains constant outwards. The velocity dispersion has a central value of $\sigma \simeq 80$ km s^{-1} and it decreases until it becomes zero.

Chapter 4

Asymmetric-drift dynamical modelling

In this chapter we present how the σ_z/σ_R ratio was calculated using the asymmetric drift dynamical modelling. In Section 4.1 we describe the derivation of the asymmetric drift equation from the second Jeans equation. In Section 4.2 we present how to link the vertical and radial components of the velocity ellipsoid with observable quantities. Then, in Section 4.3 we describe the procedure used to measure the σ_z/σ_R ratio with the asymmetric-drift equation from the kinematic data and the obtained results for NGC 7664.

4.1 Asymmetric-drift equation

Any stellar system in the solar surroundings rotates around the galactic center more slowly then the local standard of rest (that is, the local circular speed). We can define the asymmetric drift velocity v_a of a stellar population to be the difference between the local circular velocity v_c and the mean streaming velocity $\bar{v_\phi}$ of this population:

$$v_a = v_c - \bar{v_\phi}, \tag{4.1}$$

which can be calculated using the second Jeans equation (Binney & Tremaine, 2008). In Figure 4.1 the distribution of differences between the observed azimuthal velocities v_ϕ and circular velocity v_c of stars located in the solar neighborhood is shown. The tail of negative velocities proves that many of them move at lower speed with respect to the circular velocity. This phenomenon holds also for disks of external galaxies.

We consider now the second Jeans equation in scalar form, expressed in cylindrical coordinates (R, ϕ, z), and calculated for the radial velocity component v_R:

$$\frac{\partial}{\partial t}(\nu\overline{v_R}) + \frac{\partial}{\partial R}(\nu\overline{v_R^2}) + \frac{\partial}{\partial z}(\nu\overline{v_R v_z}) + \nu\Big(\frac{\overline{v_R^2} - \overline{v_\phi^2}}{R} + \frac{\partial\Phi}{\partial R}\Big) = 0, \tag{4.2}$$

where $\overline{v_R}$, $\overline{v_z}$, and $\overline{v_\phi}$ and are the mean radial, vertical and azimuthal velocities in cylindrical coordinates, Φ is the gravitational potential that influences the star movement, and ν is the numerical spatial density of the stars defined as:

$$\nu \equiv \int f d^3 v, \tag{4.3}$$

where $f(\vec{x}, \vec{v}, t)$ is the distribution function that defines the number of stars at the time t confined in a certain volume $d^3 x$ centered in $\vec{x}$ and in the velocity interval $d^3 v$ centered in $\vec{v}$. With this definition, the $i^{-\text{th}}$ component (R, ϕ, or z) of the mean stellar velocity can be written as:
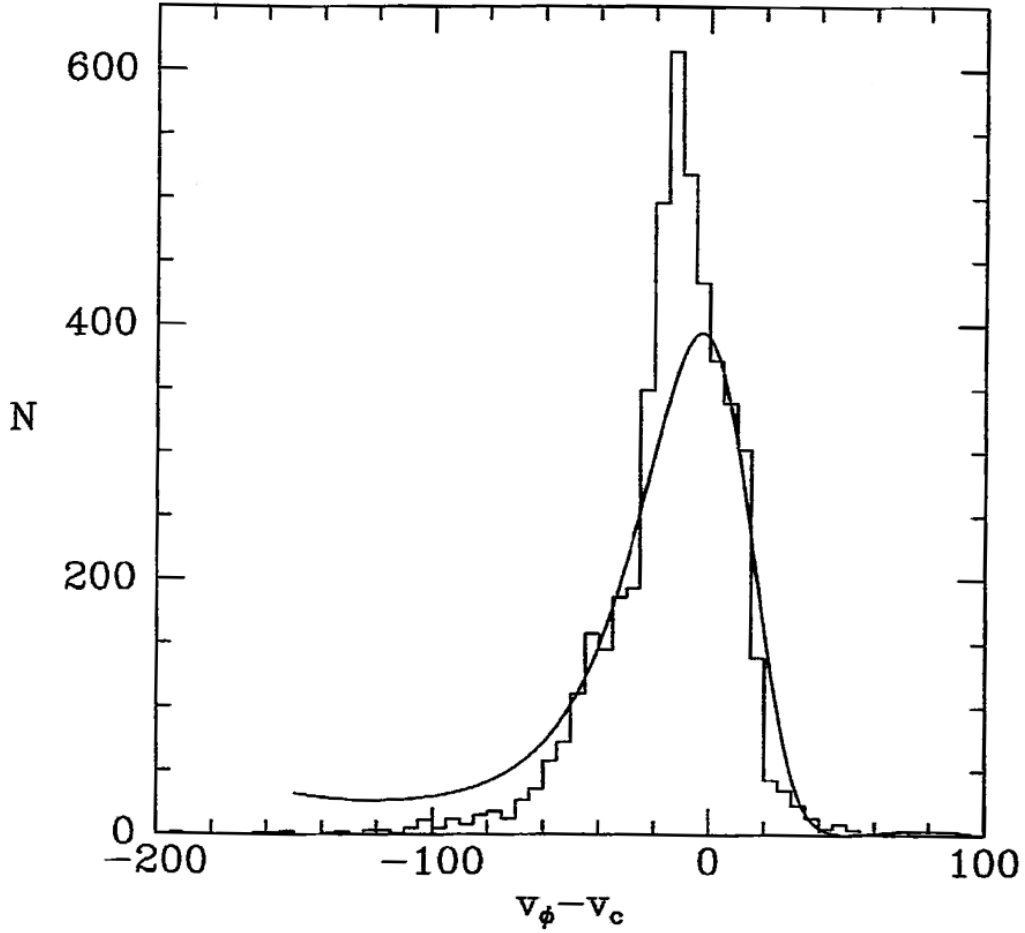
Figure 4.1: Distribution of the differences between the observed mean azimuthal velocity v_ϕ and circular velocity v_c of a sample of stars in the solar neighborhood (Nordström et al., 2004).

$$\overline{v_i} = \frac{1}{\nu} \int f v_i d^3 v. \tag{4.4}$$

At this point it is necessary to simplify the Equation 4.2 making some hypotheses:

1. the system is in steady state, so the Equation 4.2 becomes:

$$\frac{\partial}{\partial R}(\nu \overline{v_R^2}) + \nu \frac{\partial}{\partial z}(\overline{v_R v_z}) + \frac{\partial \nu}{\partial z}(\overline{v_R v_z}) + \nu \left(\frac{\overline{v_R^2} - \overline{v_\phi^2}}{R} \right) = -\nu \frac{\partial \Phi}{\partial R}; \tag{4.5}$$

2. we suppose to be confined onto the galactic plane ($z \simeq 0$) where the numerical volume density is almost constant ($\frac{\partial \nu}{\partial z}|_{z_\odot} \simeq 0$), so the previous equation becomes:

$$\frac{\partial}{\partial R}(\nu \overline{v_R^2}) + \nu \frac{\partial}{\partial z}(\overline{v_R v_z}) + \nu \left(\frac{\overline{v_R^2} - \overline{v_\phi^2}}{R} \right) = -\nu \frac{\partial \Phi}{\partial R}; \tag{4.6}$$

3. we suppose that SVE σ_{ij}^2 has the axes that are aligned with the reference system (R, ϕ, z) and it is diagonalized, so:

$$\sigma_{ij}^2 = \overline{v_i v_j} - \overline{v_i}\,\overline{v_j} = 0, \tag{4.7}$$

for $i \neq j$; that is, for the radial and vertical components:

$$\overline{v_R v_z} = \overline{v_R}\,\overline{v_z}. \tag{4.8}$$

Multiplying all the terms of Equation 4.7 for R/ν and noticing that the gradient of the potential multiplied for the radius corresponds to the square of the circular velocity:

$$R\frac{\partial \Phi}{\partial R} = v_c^2, \tag{4.9}$$

we obtain the following expression:

$$\frac{R}{\nu}\frac{\partial}{\partial R}(\nu \overline{v_R^2}) + R\frac{\partial}{\partial z}(\overline{v_R\,v_z}) + (\overline{v_R^2} - \overline{v_\phi^2}) = -v_c^2. \tag{4.10}$$

The previous equation can be rewritten considering that:

$$\frac{1}{\nu}\frac{\partial}{\partial R}(R\nu \overline{v_R^2}) = \frac{R}{\nu}\frac{\partial}{\partial R}(\nu \overline{v_R^2}) + \overline{v_R^2}; \tag{4.11}$$

so we obtain:

$$v_c^2 - \overline{v_\phi}^2 = -\overline{v_R^2} - \frac{R}{\nu}\frac{\partial}{\partial R}(\nu \overline{v_R^2}) - R\frac{\partial}{\partial z}(\overline{v_R\,v_z}) + \sigma_\phi^2, \tag{4.12}$$

and:

$$v_c^2 - \overline{v_\phi}^2 = -\overline{v_R^2}\left(1 + \frac{R}{\nu \overline{v_R^2}}\frac{\partial}{\partial R}(\nu \overline{v_R^2}) + \frac{R}{\overline{v_R^2}}\frac{\partial}{\partial z}(\overline{v_R\,v_z}) - \frac{\sigma_\phi^2}{\overline{v_R^2}}\right). \tag{4.13}$$

Expanding the mixed term we obtain:

$$\frac{\partial}{\partial z}(\overline{v_R\,v_z}) = \frac{\partial \overline{v_R}}{\partial z}\overline{v_z} + \overline{v_R}\frac{\partial \overline{v_z}}{\partial z} = 0, \tag{4.14}$$

where $\frac{\partial \overline{v_R}}{\partial z} = 0$ because they are independent variables and $\frac{\partial \overline{v_z}}{\partial z} = 0$ for the symmetry of the system. The second term of Equation 4.13 can be expanded as:

$$\frac{R}{\nu \overline{v_R^2}}\frac{\partial}{\partial R}(\nu \overline{v_R^2}) = \frac{\partial \ln(\nu \overline{v_R^2})}{\partial \ln R} = \frac{R}{\nu}\frac{\partial \nu}{\partial R} + \frac{R}{\overline{v_R^2}}\frac{\partial \overline{v_R^2}}{\partial R}, \tag{4.15}$$

so, the Equation 4.13 becomes:

$$v_c^2 - \overline{v_\phi}^2 = -\overline{v_R^2}\left(1 + \frac{R}{\nu}\frac{\partial \nu}{\partial R} + \frac{R}{\overline{v_R^2}}\frac{\partial \overline{v_R^2}}{\partial R} - \frac{\sigma_\phi^2}{\overline{v_R^2}}\right). \tag{4.16}$$

Since the numerical volume density ν is proportional to the luminosity volume density of the stars and to the luminosity surface density (i.e., the surface brightness) of the galaxy, we adopt an exponential law for ν:

$$\nu = \nu_0 e^{-R/h}, \tag{4.17}$$

where ν_0 is the central density and h is the scale length. The Equation 4.16 becomes:

$$v_c - \overline{v_\phi}^2 = -\overline{v_R^2}\left(1 - \frac{R}{h} + \frac{R}{\overline{v_R^2}}\frac{\partial \overline{v_R^2}}{\partial R} - \frac{\sigma_\phi^2}{\overline{v_R^2}}\right). \tag{4.18}$$

If we assume that the stars move onto circular orbits, characterized by a null mean radial velocity $\overline{v_R}$, the radial and azimuthal components of the velocity dispersion can be written as:

$$\sigma_R^2 = \overline{v_R^2} - \overline{v_R}^2 = \overline{v_R^2}, \tag{4.19}$$

$$\sigma_\phi^2 = \overline{v_\phi^2} - \overline{v_\phi}^2, \tag{4.20}$$

the Equation 4.18 can be rewritten as:

$$v_c^2 - \overline{v_\phi}^2 = -\sigma_R^2\left(1 + \frac{R}{\nu\sigma_R^2}\frac{\partial}{\partial R}(\nu\sigma_R^2) - \frac{\sigma_\phi^2}{\sigma_R^2}\right). \tag{4.21}$$

If we parametrize the radial velocity dispersion as:

$$\sigma_R^2 = \sigma_{R,0}^2 e^{-2R/l}, \tag{4.22}$$

where $\sigma_{R,0}$ is the central radial velocity dispersion and l is the scale length. The equation 4.21 becomes:

$$v_c^2 - \overline{v_\phi}^2 = -\sigma_{R,0}^2 e^{-2R/l}R\left(1 + \frac{1}{h} + \frac{2}{l} - \frac{\sigma_\phi^2}{\sigma_R^2}\right) \tag{4.23}$$

that is the asymmetric drift equation.

4.2   Detemination of the σ_z/σ_R ratio

To measure the ratio σ_z/σ_R of a galaxy characterized by an inclination angle i, we consider a cylindrical coordinate system (R,ϕ,z) centered on the galaxy with the disk on the (x, y) plane, and the x axis coinciding with the line of nodes (LON), that describes the intersection between the sky and galactic planes. Given a generic point P on the galaxy, the coordinate z describes the distance between this point and its projection on the (x, y) plane; R represents the distance of the projected point from the origin, while ϕ describes the angle between R and the x axis. It is possible to describe the SVE in any point P of the disk from the measurement of the velocity dispersion along the line of sight (LOS). Suppose that the observer is located on the disk plane: the LOS crosses the disk in P(r,ϕ) where we want to obtain the SVE (Figure 4.2). In this configuration, we measure the projections of the velocity dispersion components σ_R and σ_ϕ along the LOS. They are:

$$\sigma_R \sin\phi, \tag{4.24}$$

$$\sigma_\phi \cos\phi. \tag{4.25}$$

In this case, the vertical velocity dispersion σ_z is perpendicular to the LOS, so its projection is null. In general, the galactic disk appears to be tilted with respect to the observer. In this configuration, that can be seen in Figure 4.3, the three components of the velocity dispersion measured along the LOS are:

$$\sigma_R \sin\phi \sin i, \tag{4.26}$$

$$\sigma_\phi \cos\phi \sin i, \tag{4.27}$$
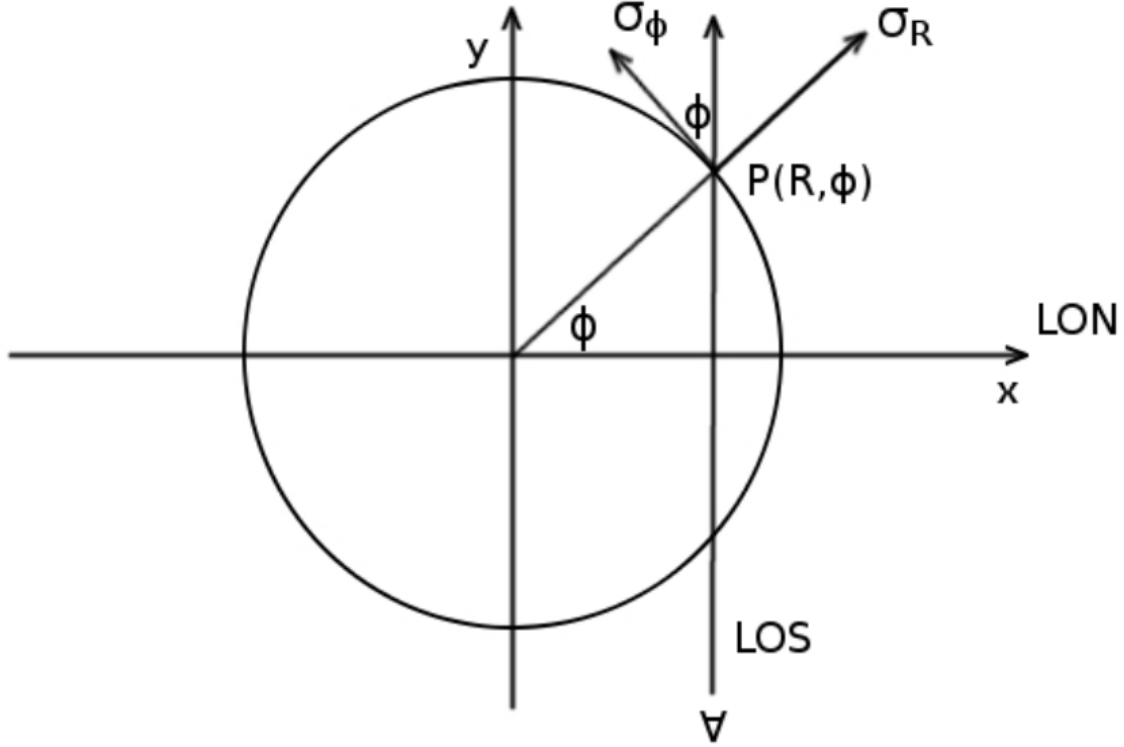
$$\sigma_z \cos i. \tag{4.28}$$

Figure 4.2: Geometry of a disk system. The disk is onto the (x, y) plane. The observer is onto the disk plane and the LOS crosses the disk in the point $P(R, \phi)$. The observer measures the projections of σ_R and σ_ϕ of the SVE in the point P, while the projection of σ_z is null in this configuration, because it is perpendicular to the LOS.

We notice that the velocity dispersion along the LOS σ_{LOS} is given by:

$$\sigma_{\text{LOS}}^2 = \sigma_R^2 \sin^2 \phi \sin^2 i + \sigma_\phi^2 \cos^2 \phi \sin^2 i + \sigma_z^2 \cos^2 i = (\sigma_R^2 \sin^2 \phi + \sigma_\phi^2 \cos^2 \phi) \sin^2 i + \sigma_z^2 \cos^2 i. \quad (4.29)$$

The velocity dispersion along the disk major ($\phi = 0°$) and minor ($\phi = 90°$) axis is:

$$\sigma_{\text{maj}}^2(R) = \sigma_\phi^2 \sin^2 i + \sigma_z^2 \cos^2 i, \quad (4.30)$$

$$\sigma_{\text{min}}(R \cos i) = \sigma_R^2 \sin^2 i + \sigma_z^2 \cos^2 i, \quad (4.31)$$

respectively. On the major axis, the radial component σ_R of the SVE is not measurable because it is perpendicular to the LOS; for the same reason, the tangential component σ_ϕ is not measurable on the minor axis. Unfortunately, it is not possible to obtain the three components of the velocity dispersion using only the Equations 4.30 and 4.31 since the observables (σ_{maj}, σ_{min}) are less then the unknowns (σ_R, σ_ϕ, and σ_z), so we need to add at least another relation.

Since we are studying the motion of stars located in the disk, we can assume they move onto nearly circular orbits, so their mean radial velocity $\overline{v_R}$ can be assumed to be zero and we can rely onto the epicyclic approximation. According to it, the ratio between the tangential and radial components of the SVE depends on the Oort's constant A and B:

$$\frac{\sigma_\phi^2}{\sigma_R^2} = \frac{-B}{A - B}, \quad (4.32)$$
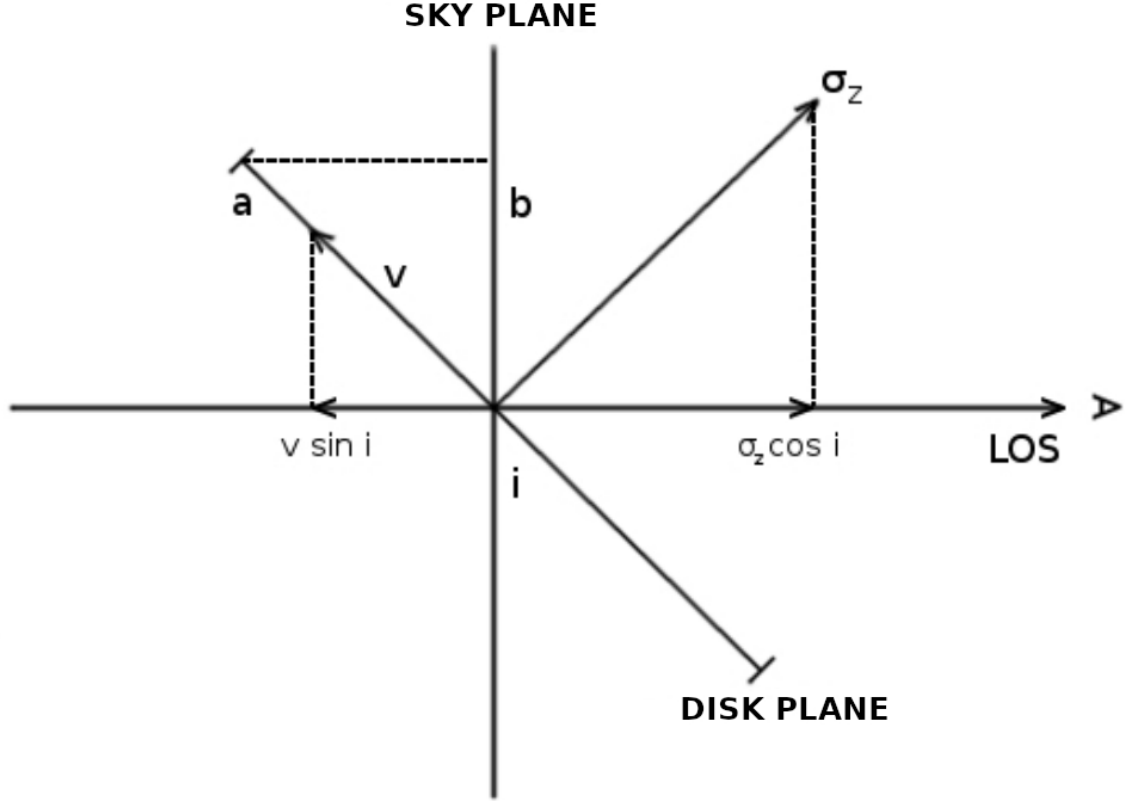
Figure 4.3: Geometry of a disk system. The disk is inclined with an angle i with respect to the sky plane. The lengths a and $b = a\cos i$ represent the semi-major and semi-minor axes projected onto the sky, respectively. The observer is outside the disk plane and the intersection between the LOS and disk plane is $(90° - i)$. The velocity along the LOS $v_{\mathrm{LOS}} = v\sin i$ and velocity dispersion $\sigma_{\mathrm{LOS}} = \sigma_z\cos i$ are shown.

where:

$$A = \frac{1}{2}\left(\frac{v_{\mathrm{c}}}{R} - \frac{dv_{\mathrm{c}}}{dR}\right), \tag{4.33}$$

$$B = -\frac{1}{2}\left(\frac{v_{\mathrm{c}}}{R} + \frac{dv_{\mathrm{c}}}{dR}\right). \tag{4.34}$$

Thanks to this relation, we can derive the σ_ϕ^2/σ_R^2 ratio in epyciclic approximation:

$$\frac{\sigma_\phi^2}{\sigma_R^2} = \frac{-B}{A - B} = \frac{1}{2}\left(1 + \frac{R}{v_{\mathrm{c}}}\frac{dv_{\mathrm{c}}}{dR}\right) = \frac{1}{2}\left(1 + \frac{d\ln v_{\mathrm{c}}}{d\ln R}\right). \tag{4.35}$$

At this point, the Equations 4.30, 4.31, and 4.35 allow us to obtain the values of σ_R, σ_ϕ, and σ_z, once the inclination of the disk i and the circular velocity v_{c} are known. From a photometric analysis we can derive the disk inclination i by measuring the major a and minor b axis of the projected disk, as shown in Figure 4.3:

$$i = \arccos\left(\frac{b}{a}\right). \tag{4.36}$$

We adopt a power law parametrization for the circular velocity v_{c}, that can be measured from the gas rotation curve:

$$v_{\mathrm{c}} = v_0 R^\alpha \tag{4.37}$$

where v_0 represent the scale velocity and α is the power index. By substituting it into Equation 4.35 we get:

$$\frac{\sigma_\phi^2}{\sigma_R^2} = \frac{1}{2}(1 + \alpha). \tag{4.38}$$

Then, we assume an exponential law with the same scale length l for σ_R and σ_z:

$$\sigma_R = \sigma_{R,0} e^{-R/l}, \tag{4.39}$$

$$\sigma_z = \sigma_{z,0} e^{-R/l}. \tag{4.40}$$

Therefore, the shape of the SVE does not vary with the radius, while its size decreases. The size is longer in the center of the galaxy, where the velocity dispersion is larger. So, putting the Equations 4.35, 4.39, and 4.40 in Equations 4.30 and 4.31 we get:

$$\sigma_{\mathrm{maj}}^2(R) = \frac{1}{2}(1 + \alpha)\sigma_{R,0}^2 e^{-2R/l} \sin^2 i + \sigma_{z,0}^2 e^{-2R/l} \cos^2 i \tag{4.41}$$

$$\sigma_{\mathrm{min}}^2(R \cos i) = \sigma_{R,0}^2 e^{-2R/l} \sin^2 i + \sigma_{z,0}^2 e^{-2R/l} \cos^2 i. \tag{4.42}$$

Moreover, we use the stellar component as tracer for the potential of the galaxy and applying the asymmetric drift equation we get $\overline{v_\phi}$ as:

$$v_{\mathrm{c}}^2 - \overline{v_\phi}^2 = -\sigma_R^2 \left(1 + \frac{R}{\nu\sigma_R^2}\frac{\partial}{\partial R}(\nu\sigma_R^2) - \frac{\sigma_\phi^2}{\sigma_R^2} \right). \tag{4.43}$$

We adopt an exponential law for the numerical volume density ν:

$$\nu = \nu_0 e^{-R/h}, \tag{4.44}$$

where h is the scale length. Therefore, substituting the Equations 4.37 4.39, and 4.44 in Equation 4.43, we get:

$$\overline{v_\phi}^2 = v_0^2 R^{2\alpha} + \sigma_{R,0}^2 e^{-2R/a}\left[\frac{1}{2}(1 - \alpha) - R\left(\frac{1}{h} + \frac{2}{a}\right) \right]. \tag{4.45}$$

From the photometic observations we can estimate the values of the scale length h and disk inclination i, while from the spectroscopic observations we can measure the rotation velocity of the stars along the major axis $v_{\star,\mathrm{maj}} = \overline{v_\phi}$, the velocity dispersion of the stars on the major and minor axis σ_{maj}, and σ_{min}, respectively. Since the streaming velocity of the stars is measured from its component projected along the LOS, their velocity on the minor axis $v_{\star,\mathrm{min}} = 0$, since it is perpendicular to the LOS. Interpolating this results with the Equations 4.37, 4.41 and 4.42, we obtain the values of $\alpha, v_0, \sigma_{R,0}, \sigma_{z,0}$, and l. Finally, from the parametrization that we assumed for the radial and vertical components of the velocity dispersion, we have:

$$\frac{\sigma_z}{\sigma_R} = \frac{\sigma_{z,0}}{\sigma_{R,0}} = \mathrm{constant}. \tag{4.46}$$

4.3   Determination of the σ_z/σ_R ratio from the asymmetric drift

4.3.1   `disk_heating` procedure

To determine the shape of the SVE of the NGC 7664 disk, Cuomo (2015) used the IDL program `disk_heating` written by E.M. Corsini which adopt the methods described in Section 4.2. The inputs requested by the program are the ionized-gas velocity curve along the major axis (Section 3.5.1), the velocity curve of the stellar component along the major axis, and the velocity dispersion of the stellar component along the major and minor axis (Section 3.5). Moreover, it is necessary to provide the values for the scale radius h and inclination i. Starting from these data, the program returns the values for the parameters $v_0, \alpha, a, \sigma_{R,0}$, and $\sigma_{z,0}$, from which we obtain the ratio between the vertical and radial components of the disk SVE σ_z/σ_R. To do that, we neglect the part of the galaxy dominated by the spheroid and assume that the ionized gas is located onto a dynamically cold disk, where rotation velocity traces the circular velocity. To determine the values of the free parameters $v_0, \alpha, a, \sigma_{R,0}$, and $\sigma_{z,0}$, the `disk_heating` program uses the IDL procedure `CURVEFIT`, that computes a non-linear least squares interpolation of the functions that contain the free parameters. These functions must have partial derivatives that are known or approximable. The algorithm is based on the minimization method of the non-linear least squares of Levenberg-Marquardt (Press et al., 1992), which is based on the minimization of the χ^2 function given by:

$$\chi^2 = \frac{1}{N_{\mathrm{dof}}} \sum_{i=1}^{n} \frac{(Y_{\mathrm{mod,\,i}} - Y_i)^2}{\sigma_i^2}, \tag{4.47}$$

where N_{dof} is the number of degrees of freedom given by the difference between the number of data points of and the number of free parameters to be calculated, Y_i are the n values of the dependent variable vector, $Y_{\mathrm{mod,\,i}}$ are the corresponding values found with the interpolation, and σ_i are the terms of the weight function. The procedure is iterated until the χ^2 function reaches a fixed minimum value or the maximum number of iterations is reached.

The first step done by the program is interpolating the ionized-gas kinematics data to estimate the initial values of v_0 and α, required to best fit the global kinematics of the stars and ionized gas. For the ionized-gas velocity curve, it uses:

$$v_{\mathrm{c}} = v_0 R^{\alpha} \tag{4.48}$$

where v_0 is a scale velocity, α is the power index, and v_{c} is the velocity obtained by deprojecting the observed gas velocity $v_{\mathrm{gas,\,maj}}$ on the galactic plane (that corresponds to the one obtained in Section 3.5.1):

$$v_{\mathrm{c}} = \frac{v_{\mathrm{gas,\,maj}}}{\sin i}. \tag{4.49}$$

Once the program found the values of v_0 and α, it proceeds with the determination of the σ_z/σ_R ratio. This is obtained using the ionized-gas rotation curve, the stellar component rotation curve along the major axis and the radial velocity dispersion profiles along the major and minor axes. The parametric laws that interpolate these data are:

1. For the ionized-gas velocity along the major axis:

$$\frac{v_{\mathrm{gas,\,maj}}}{\sin i} = v_{\mathrm{c}} = v_0 R^{\alpha}. \tag{4.50}$$

2. For the stellar velocity along the galaxy major axis:

$$\frac{v_{\star,\mathrm{maj}}^2}{\sin i} = \overline{v_\phi}^2 = v_0^2 R^{2\alpha} + \sigma_{R,0}^2 e^{-2R/a}\left[\frac{1}{2}(1-\alpha) - R\left(\frac{1}{h}+\frac{2}{a}\right)\right]. \tag{4.51}$$

3. For the stellar velocity dispersion along the major axis:

$$\sigma_{\mathrm{maj}}(R) = \sqrt{\frac{1}{2}(1+\alpha)\sigma_{R,0}^2 e^{-2R/l}\sin^2 i + \sigma_{z,0}^2 e^{-2R/l}\cos^2 i}. \tag{4.52}$$

4. For the stellar velocity dispersion along the minor axis:

$$\sigma_{\mathrm{min}}(R\cos i) = \sqrt{\sigma_{R,0}^2 e^{-2R/l}\sin^2 i + \sigma_{z,0}^2 e^{-2R/l}\cos^2 i}. \tag{4.53}$$

We notice that $R\cos i$ is the projection of the radius on the minor axis, so it must be deprojected before the interpolation, as the stellar velocity measured on the major axis used in Equation 4.51.

To interpolate the data, the program requires as input the initial guess values for l in arcsec, $\sigma_{R,0}$ and $\sigma_{z,0}$ in km s^{-1}, the scale velocity of the ionized gas v_0 in km s^{-1}, and α. It also requires the values of the galaxy inclination i and the disk scale length h. The program finds the best values of the parameters, by evaluating the minimum χ^2, that corresponds to:

$$\chi^2 = \chi_{v_{\mathrm{gas}}}^2 + \chi_{v_\star}^2 + \chi_{\sigma_{\mathrm{maj}}}^2 + \chi_{\sigma_{\mathrm{min}}}^2 \tag{4.54}$$

where $\chi_{v_{\mathrm{gas}}}^2$ corresponds to the ionized-gas velocity, $\chi_{v_\star}^2$ to the stellar velocity, while $\chi_{\sigma_{\mathrm{maj}}}^2$ and $\chi_{\sigma_{\mathrm{min}}}^2$ correspond to the stellar velocity dispersion along the major and minor axis.

For each component we have:

$$\chi_j^2 = \sum_{i=1}^n \frac{(Y_{\mathrm{mod,i}} - Y_{\mathrm{oss,i}})^2}{\sigma_i^2}, \tag{4.55}$$

where $j = v_{\mathrm{gas}}, v_\star, \sigma_{\mathrm{maj}}, \sigma_{\mathrm{min}}$, and Y_{mod} is the value obtained from the interpolation, $Y_{\mathrm{oss,i}}$ is the observed value, and σ is the error on each measure. To normalize this function, we calculate the normalized $\chi_{\mathrm{red}}^2 = \chi^2/\mathrm{dof}$. Once the minimum is found, the program returns the values of $v_0, \alpha, l, \sigma_{R,0}$ and $\sigma_{z,0}$ that better fits the data, with their corresponding errors.

4.3.2   Results for NGC 7664

To determine the vertical and radial components of the disk velocity dispersion σ_z and σ_R of NGC 7664 with the `disk_heating` program, Cuomo (2015) selected the region of the galaxy in which the disk is dominating with respect to the spheroid, estimating the radius r_{bd} in which the surface brightness of the spheroid is equal to the one of the disk from the photometric decomposition by Kent (1985)(Figure 4.4). It is $r_{\mathrm{bd,maj}} = 5$ arcsec for the major axis, while for the minor one it corresponds to $r_{\mathrm{bd,min}} = r_{\mathrm{bd,maj}}\cos i = 2.8$ arcsec. Therefore, the kinematic data points taken on the major axis for $R < 5$ arcsec and on the minor axis for $R < 2.8$ arcsec were excluded. However, the results obtained from this choice were still contaminated by the presence of the spheroid. So, the final choice was to exclude the kinematic data points taken on the major axis for $R < 10$ arcsec and on the minor axis for $R < 5.6$ arcsec.

Since the measurements of the ionized gas kinematics performed by Cuomo (2015) extends out to $R \sim 20$ arcsec, the circular velocity curve cannot be parametrized by $v_{\mathrm{gas,maj}}/\sin i = v_0 R^\alpha$. Therefore, it was necessary to include the ionized-gas data obtained by Rubin et al. (1980), which extends up to $R \sim 70$ arcsec.
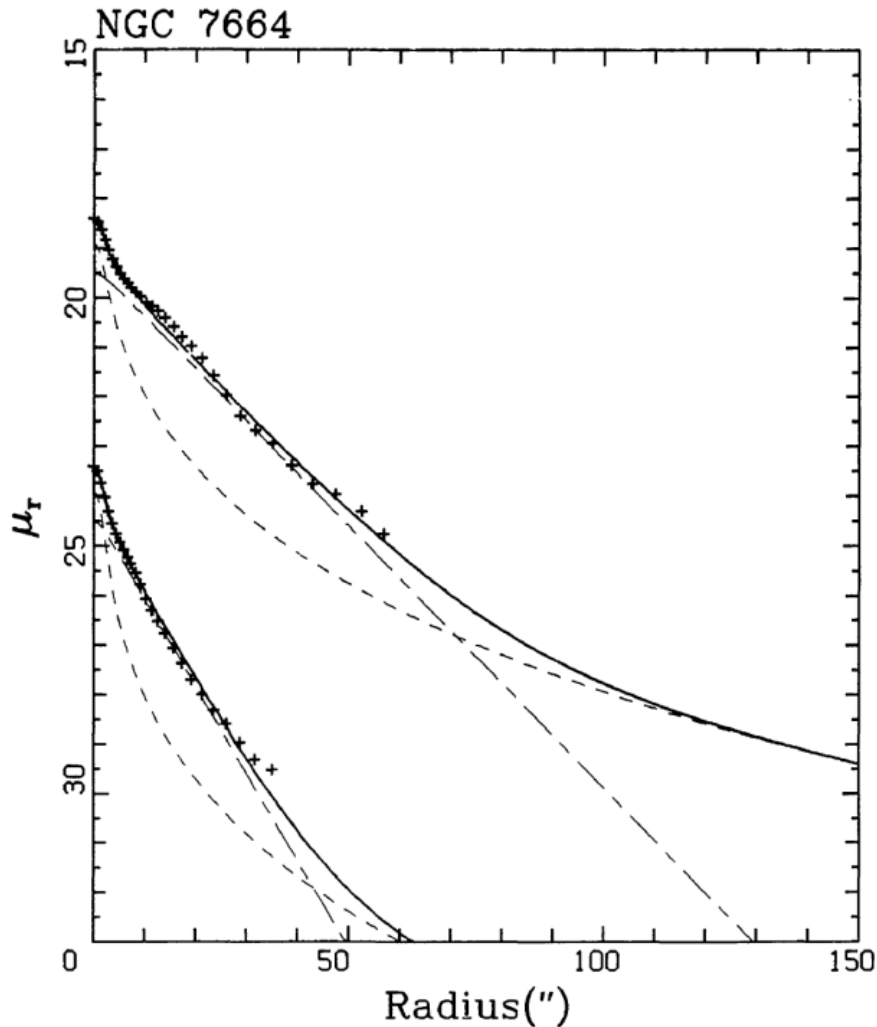
Figure 4.4: r-band surface-brightness radial profiles observed along the major (upper plot) and minor (lower plot, increased by 5 mag arcsec^{-2}) axes of NGC 7664. The dotted lines represent the spheroid contribution, dashed lines give the disk contribution, and solid lines mark their total contribution (Kent, 1985).

The inclination was retrieved using the formula:

$$\cos^2 i = \frac{q^2 - q_0^2}{1 - q_0^2}, \tag{4.56}$$

where q is the observed axial ratio and q_0 is the intrinsic one. In this case, $q = 0.44$ was retrieved from de Vaucouleurs et al. (1991), and $q_0 = 0.20$ was assumed following Guthrie (1992). Using these values from literature, the inclination of NGC 7664 used for this analysis was $i = 56°$.

The disk scale radius $h = 10$ arcsec was retrieved from the r-band photometry obtained by Kent (1985) and shown in Figure 4.4. The limit surface brightness is approximately 25 mag arcsec^{-2}. The analysis performed by Kent (1985) led to a decomposition along the major and minor axis of NGC 7664 assuming a spheroid that follows the $r^{1/4}$ law and an exponential disk.

The parameters α and v_0 were retrieved through a preliminary interpolation of the ionized-gas velocity curve; then, the global interpolation of the 5 parameters $v_0, \alpha, l, \sigma_{R,0}$, and $\sigma_{z,0}$ was performed. However, in this way the results of the preliminary estimation of the parameters v_0 and α were not consistent with the ones obtained from the global interpolation. Therefore it was chosen to fix v_0 and α to the values retrieved in the first preliminary analysis to only retrieve the remaining parameters

$l, \sigma_{R,0}$ and $\sigma_{z,0}$ from the global interpolation.

The results of the `disk_heating` procedure for NGC 7664 are:

- $\alpha = 0.04 \pm 0.01$

- $v_0 = 166.03 \pm 5.27$ km s^{-1}

- $a = 22.04 \pm 1.10$ arcsec

- $\sigma_{R,0} = 108.70 \pm 2.35$ km s^{-1}

- $\sigma_{z,0} = 145.33 \pm 6.44$ km s^{-1}

from which Cuomo (2015) retrieved the ratio between the vertical and radial components of the SVE of the NGC 7664 disk:

$$\sigma_z/\sigma_R = 1.34 \pm 0.07. \tag{4.57}$$

The result of the interpolation is shown in Figure 4.5.
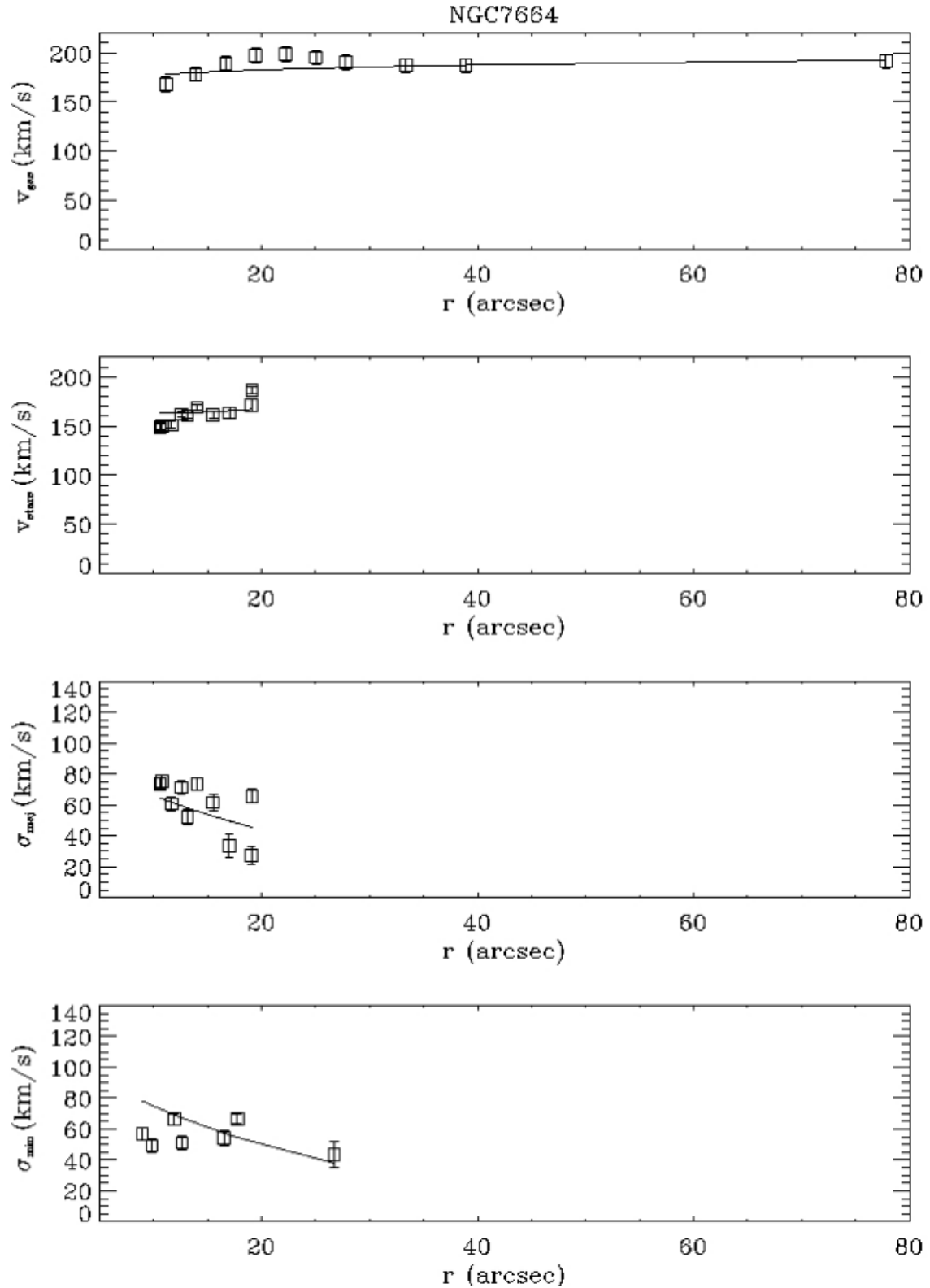
Figure 4.5: Asymmetric drift dynamical model of NGC 7664. *From top to bottom panels*: model of the ionized-gas velocity curve along the major axis, stellar velocity curve along the major axis, and stellar velocity dispersion along the major and minor axis, respectively. The ionized gas and stellar component velocities along the major axis and values of the radius along the minor axis are deprojected onto the disk plane (Cuomo, 2015).

Chapter 5

Jeans dynamical modelling

In this chapter we describe the dynamical modelling of the photometric and kinematic data that we used to derive the shape of the SVE of NGC 7664. In Section 5.1 we describe the Jeans anisotropic model. In Section 5.2 we explain how we applied the Jeans modelling, while in Section 5.3 we present our results.

5.1 Jeans anisotropic model formalism

The large majority of the galaxies in the Universe are nearly axisymmetric and present a disk component. They include fast-rotator early-type galaxies and spiral galaxies (Emsellem et al., 2007). Both of them appear dominated by stellar matter inside one half-light radius, that is the radius inside which half of the total galaxy luminosity is emitted (e.g. Gerhard et al., 2001, Cappellari et al., 2006). Observations suggest that they have a dynamical structure characterized by a flattening of the velocity ellipsoid in the vertical direction (Gerssen et al., 1997).

Cappellari (2008) proposed a simple and efficient anisotropic generalization of the semi-isotropic axisymmetric Jeans formalism, which is used to model the stellar kinematics of galaxies. This Jeans Anisotropic Modelling (JAM) allows to know the structure of the fast-rotator and spiral galaxies. It can be applied to measurements of both the mass-to-light ratio and amount of rotation in the central regions of these galaxies. It also allows for the inclusion of dark matter and study multiple kinematical components.

5.1.1 Jeans anisotropic solution

To find the solution of the Jeans equations to be compared to observed data, Cappellari (2008) started from the general axysimmetric second Jeans equations in cylindrical coordinates (R, ϕ, z) for the radial and vertical components:

$$\frac{\partial}{\partial R}(\nu \overline{v_R^2}) + \nu \frac{\partial}{\partial z}(\overline{v_R v_z}) + \frac{\partial \nu}{\partial z}(\overline{v_R v_z}) + \nu \left(\frac{\overline{v_R^2} - \overline{v_\phi^2}}{R}\right) = -\nu \frac{\partial \Phi}{\partial R}, \tag{5.1}$$

$$\frac{\nu \overline{v_R v_z}}{R} + \frac{\partial (\nu \overline{v_z^2})}{\partial z} + \frac{\partial (\nu \overline{v_R v_z})}{\partial R} = -\nu \frac{\partial \Phi}{\partial z}, \tag{5.2}$$

respectively, where we assumed the steady state and axial symmetry. The following additional assumptions were made:

- the SVE is aligned with the cylindrical coordinate system (R, ϕ, z);
- the anisotropy is constant and quantified by $b = \overline{v_z^2}/\overline{v_R^2}$.

In this case, the Jeans equations can be written as:

$$\frac{b\nu\overline{v_z^2} - \nu\overline{v_\phi^2}}{R} + \frac{\partial(b\nu\overline{v_z^2})}{\partial R} = -\nu\frac{\partial\Phi}{\partial R},$$
(5.3)

$$\frac{\partial(\nu\overline{v_z^2})}{\partial z} = -\nu\frac{\partial\Phi}{\partial z},$$
(5.4)

which corresponds to the semi-isotropic case when $b = 1$.

With the boundary condition $\nu\overline{v_z^2} = 0$ at $z \to \infty$ the solution is:

$$\nu\overline{v_z^2}(R, z) = \int_z^\infty \nu\frac{\partial\Phi}{\partial z}dz,$$
(5.5)

and hence:

$$\nu\overline{v_\phi^2}(R, z) = b\Big[R\frac{\partial(\nu\overline{v_z^2})}{\partial R} + \nu\overline{v_z^2}\Big] + R\nu\frac{\partial\Phi}{\partial R}.$$
(5.6)

To derive the solutions of the Jeans equations, Cappellari (2008) chose the MGE parametrization (Section 2.4) to model the stellar luminosity density and total mass density (which can include dark matter and a central supermassive black hole), due to its flexibility in reproducing the surface brightness of real galaxies and availability of robust routines to fit the galaxy photometry (Cappellari, 2002). From this parametrization of the galaxy surface brightness we can describe the total mass density ρ of the galaxy by a different set of M Gaussian components:

$$\rho(R, z) = \sum_{j=1}^M \frac{M_j}{(\sqrt{2\pi}\sigma_j)^3 q_j} \exp\Big[-\frac{1}{2\sigma_j^2}\Big(R^2 + \frac{z^2}{q_j^2}\Big)\Big].$$
(5.7)

In the self-consistent case, where the mass follows light, the Gaussians are the same as the ones used to describe the surface brightness distribution of the galaxy given by Equation 2.10 and we have $M = N$, $\sigma_j = \sigma_j'$, $q_j = q_j'$ and the mass $M_j = \Upsilon_j L_j$, where Υ_j is the M/L ratio, which can have different values for each Gaussian component.

In the non self-consistent case the density can be described with the sum of two sets of Gaussians: the first set is derived by deprojecting the surface brightness of the galaxy given by Equation 2.10 and the second can be obtained by fitting a MGE model to some adopted analytic parametrization for the dark matter halo.

The gravitational potential generated by the mass density distribution of Equation 5.7 is given by Emsellem et al. (1994):

$$\Phi(R, z) = -\sqrt{2/\pi}G\int_0^1 \sum_{j=1}^M \frac{M_j H_j(u)}{\sigma_j}du$$
(5.8)

where G is the gravitational constant and:

$$H_j(u) = \frac{\exp\Big\{-\frac{u^2}{2\sigma_j^2}\Big[R^2 + \frac{z^2}{1-(1-q_j^2)u^2}\Big]\Big\}}{\sqrt{1-(1-q_j^2)u^2}}.$$
(5.9)

On the other hand, a supermassive black hole with mass $M_\bullet$ can be modeled by adding a point-mass potential:

$$\Phi_\bullet(R, z) = -\frac{GM_\bullet}{\sqrt{R^2 + z^2}} \tag{5.10}$$

to the one of Equation 5.8.

The MGE formalism is applied to the solution of axisymmetric anisotropic Jeans equations. Substituting Equations 2.10 and 5.8 into Equations 5.5 and 5.6, the integral in z can be analytically computed, obtaining:

$$[\nu\overline{v_R^2}]_k = b_k[\nu\overline{v_z^2}]_k, \tag{5.11}$$

$$[\nu\overline{v_z^2}]_k = 4\pi G \int_0^1 \sum_{j=1}^M \frac{\sigma_k^2 q_k^2 \nu_k q_j \rho_{o,j} H_j(u) u^2}{1 - Cu^2} du, \tag{5.12}$$

$$[\nu\overline{v_\phi^2}]_k = b_k[\nu\overline{v_z^2}]_k + 4\pi G \int_0^1 \sum_{j=1}^M \frac{\nu_k q_j \rho_{0,j} H_j(u) u^2}{1 - Cu^2} DR^2 du = 4\pi G \int_0^1 \sum_{j=1}^M \frac{\nu_k q_j \rho_{0,j} H_j(u) u^2}{1 - Cu^2}(DR^2 + b_k \sigma_k^2 q_k^2) du, \tag{5.13}$$

where $\nu_k = \nu_k(R, z)$, $\rho_{0,j} = \rho_j(0,0)$ and:

$$C = 1 - q_j^2 - \frac{\sigma_k^2 q_k^2}{\sigma_j^2}, \tag{5.14}$$

$$D = 1 - b_k q_k^2 - [(1 - b_k)C + (1 - q_j^2)b_k]u^2. \tag{5.15}$$

In all the previous equations, the index k refers to the parameters (or the anisotropy) of the Gaussians describing the galaxy luminosity density (Equation 2.10), while the index j refers to the parameters of the Gaussians describing the total mass density (Equation 5.7), from which the potential is obtained. The total luminosity-weighted anisotropy at a certain spatial location (R, z) of an MGE model is given by the standard definition of Binney & Mamon (1982) combined with the Equation 5.11:

$$\beta_z(R, z) = 1 - \frac{\overline{v_z^2}}{\overline{v_R^2}} = 1 - \frac{\sum_k[\nu\overline{v_z^2}]_k}{\sum_k b_k[\nu\overline{v_z^2}]_k} \simeq 1 - \frac{\sum_k \nu_k}{\sum_k b_k \nu_k}. \tag{5.16}$$

The last approximation comes from the fact that $[\overline{v_z^2}]_k$, being mostly a function of the total MGE potential, varies relatively little for the different Gaussian components, while ν_k varies by many orders of magnitude for the various luminous MGE components. This allows the global anisotropy of an MGE model, at a certain spatial location in the meridional plane, to be approximately estimated from a simple luminosity-weighted sum of b_k.

5.1.2   Line-of-sight integration of the second velocity moment

The intrinsic quantities have to be integrated along the LOS to generate the observables that can be compared with kinematic data of the galaxies. A system of sky coordinates is defined with the z' axis along the LOS and x' axis aligned with the galaxy projected major axis. The galaxy coordinates (x, y, z) are related to the projected ones in the sky plane by:

$$
\begin{pmatrix} x \\ y \\ z \end{pmatrix} = \begin{pmatrix} 1 & 0 & 0 \\ 0 & -\cos i & \sin i \\ 0 & \sin i & \cos i \end{pmatrix} \begin{pmatrix} x' \\ y' \\ z'' \end{pmatrix}, \tag{5.17}
$$

where the $z-$axis coincides with the galaxy symmetry axis and cylindrical radius is given by $R^2 = x^2 + y^2$. The projected velocity second moment along the LOS $\overline{v_{\text{los}}^2} = \overline{v_z^2}$, for one luminous Gaussian component, is given by:

$$
[\Sigma\overline{v_{\text{los}}^2}]_k = \int_{-\infty}^{\infty} \left\{ [\nu\overline{v_z^2}]_k \cos^2 i + \left([\nu\overline{v_R^2}]_k \sin^2 \phi + [\nu\overline{v_\phi^2}]_k \cos^2 \phi \right) \sin^2 i \right\} dz', \tag{5.18}
$$

where $\cos \phi = x/R$. The total observed second moment for the whole MGE model is:

$$
\Sigma\overline{v_{\text{los}}^2} = \sum_{k=1}^{N} [\Sigma\overline{v_{\text{los}}^2}]_k. \tag{5.19}
$$

After the substitution of Equations 5.11, 5.12, and 5.13, the z' integral in Equation 5.18 can be explicitly written. Summing over all the N luminous Gaussian components we obtain the final expression:

$$
\begin{aligned}
\Sigma\overline{v_{\text{los}}^2}(x', y') = 4\pi^{3/2}G \int_0^1 \sum_{k=1}^{N} \sum_{j=1}^{M} \nu_{0,k} q_j \rho_{0,j} u^2 & \frac{\sigma_k^2 q_k^2(\cos^2 i + b_k \sin^2 i) + Dx'^2 \sin^2 i}{(1 - Cu^2)\sqrt{(A + B\cos^2 i)[1 - (1 - q_j^2)u^2]}} \\
& \times \exp\left\{ -A\left[x'^2 + \frac{(A+B)y'^2}{A + B\cos^2 i} \right] \right\} du,
\end{aligned} \tag{5.20}
$$

where $\nu_{o,k} = \nu_k(0,0)$ and:

$$
A = \frac{1}{2}\left(\frac{u^2}{\sigma_j^2} + \frac{1}{\sigma_k^2} \right), \tag{5.21}
$$

$$
B = \frac{1}{2}\left\{ \frac{1 - q_k^2}{\sigma_k^2 q_k^2} + \frac{(1 - q_j^2)u^4}{\sigma_j^2[1 - (1 - q_j^2)u^2]} \right\}. \tag{5.22}
$$

This equation is quick to evaluate as it still requires a single numerical quadrature and involves no special functions. This is done starting directly from the fit to the galaxy surface brightness, without the requirement for numerical deprojection or PSF deconvolution. The second moment $\overline{v_{\text{los}}^2}$ is a good approximation for the observed quantity $V_{\text{rms}}^2 = V^2 + \sigma^2$, where V and σ are the stellar mean velocity and velocity dispersion, respectively.

5.1.3   Line of sight integration of the first velocity moment

On the other hand, the projected first velocity moment $\overline{v_{\text{los}}} = \overline{v_{z'}}$ is given by:

$$
\Sigma\overline{v_{\text{los}}} = \int_{-\infty}^{\infty} \nu\overline{v_\phi} \cos \phi \sin i dz'. \tag{5.23}
$$

In this case, the two assumptions we made at the beginning of this section are not sufficient to provide a unique prediction and additional assumptions are needed. The Jeans equations 5.1 and 5.2 in fact

give a prediction for $\overline{v_\phi^2}$ and one has to decide how the second moments separate into the contribution of ordered streaming and random motion, as:

$$\overline{v_\phi^2} = \overline{v_\phi}^2 + \sigma_\phi^2. \tag{5.24}$$

Therefore, an extra assumption is needed to decide how to separate the contributions of $\overline{v_\phi}$ and σ_ϕ and derive the first moment. The first moment equations are very useful to quantify the amount of rotation in galaxies. To parametrize the separation between $\overline{v_\phi}$ and σ_ϕ, Cappellari (2008) adopted the analogue in the anisotropic case of Satoh (1980) approach, that has the advantage of providing a direct measure of the amount of rotation. For every Gaussian component it is defined as:

$$[\overline{v_\phi}]_k = \kappa \left([\overline{v_\phi^2}]_k - [\overline{v_R^2}]_k \right)^{1/2}. \tag{5.25}$$

Here, $\kappa = 0$ when the k-th Gaussian component is not rotating and $|\kappa| = 1$ when the SVE is a circle in the (v_r, v_ϕ) plane. An upper limit to $|\kappa|$ is set by the physical requirement $\sigma_\phi > 0$. When summed over all the luminous Gaussians of the MGE model:

$$\nu\overline{v_\phi^2} = \sum_{k=1}^{N} [\nu\overline{v_\phi}^2]_k. \tag{5.26}$$

Equation 5.25 implies:

$$\nu\overline{v_\phi} = \left[\nu \sum_{k=1}^{N} \kappa_k^2 \left([\nu\overline{v_\phi}^2]_k - [\nu\overline{v_R^2}]_k \right) \right]^{1/2}. \tag{5.27}$$

Substituting Equation 5.27 into Equation 5.23, and using Equations 5.11, 5.12, and 5.13 the projected first velocity moment of the whole MGE model is obtained:

$$\Sigma\overline{v_{\mathrm{los}}}(x', y') = 2\sqrt{\pi G} x' \sin i \int_{-\infty}^{\infty} \left[\nu \int_0^1 \sum_{k=1}^{N} \sum_{j=1}^{M} \frac{\kappa_k^2 \nu_k q_j \rho_{0,j} H_j(u) u^2 D}{1 - Cu^2} \right]^{1/2} dz'. \tag{5.28}$$

When κ is assumed to be constant for the whole MGE, this integral has to be evaluated only once with $\kappa_k = 1$ at the best fitting parameters $(i, \beta_z, \text{and } \Upsilon)$ previously determined from a fit to the more general second moment equation, and then $\overline{v_{los}}$ can be linearly scaled by κ to fit the data.

In summary, Cappellari (2008) presented with JAM an efficient description of the anisotropic axisymmetric Jeans formalism which is used to model kinematic data of galaxies, by assuming the following:

1. a constant mass-to-light ratio M/L;

2. a SVE that is aligned with the cylindrical coordinates (R, z) and characterized by the anisotropy parameter defined by Equation 5.16.

Once a detailed description of the surface brightness is given, the model provides a good description of the shape of the first (V) and second $(V_{\mathrm{rms}} = \sqrt{V^2 + \sigma^2})$ velocity moments that better fit the kinematic data. This formalism allows also for the inclusion of dark matter halos, supermassive black holes and multiple kinematic components.

5.2   Jeans anisotropic modelling of NGC 7664

To derive the σ_z/σ_R ratio of NGC 7664 we modelled the stellar kinematic data with the `python3` programs `run_jam` and `wrap_jam` written by C. Buttitta. These programs use the `python3` package `jampy`[1], which implements the JAM formalism of Cappellari (2008). The code takes as input the stellar kinematic parameters V, σ, and $V_{\rm rms}$ (in km s^{-1}) (Figure 3.5) with their associated errors and parameters $I_{\rm intr}$ (in L$_\odot$ pc^{-2}), σ (in arcsec), and $q_{\rm obs}$ coming from the MGE fitting (Table 2.3). The code creates a gravitational potential for the mass that follows light starting from the MGE surface brightness parametrization (Equation 5.8), whose free parameters are the mass-to-light ratio Υ, galaxy inclination i, and the anisotropy parameter defined as:

$$\beta_z = 1 - \frac{\sigma_z^2}{\sigma_R^2}. \tag{5.29}$$

We can also add a potential for a supermassive black hole (Equation 5.10), that has only as free parameter the black hole mass $M_\bullet$, and a potential for a spherical dark matter halo whose free parameters depend on its parametrization of the mass density $\rho_{\rm DM}(R)$.

Then we provided a set of values for each free parameter $(p_0, p_1, ..., p_k)$, that create a grid in which the code computes the model prediction for $\sqrt{v_{\rm los}^2} = V_{\rm rms}$ inside each bin in which the kinematic data are mapped. This step is done for each combination of the parameter values. The model and data are now compared by computing the χ^2 function given by:

$$\chi^2 = \sum_{i=i}^{n} \left[\frac{G_{{\rm mod},i} - G_i}{G_j} \right]^2, \tag{5.30}$$

where n is the number of kinematic data points G_j and $G_{{\rm mod},i}$ are the values generated by the JAM model. The code selects the set of parameters where the χ^2 is minimized and starts using them as initial values to fit the $V_{\rm rms}$ data until the difference $\Delta\chi^2$ between the computed χ^2 and the one obtained with the previous fitting reaches a minimum fixed value.

For the whole analysis, we fixed the inclination of the galaxy at $i = 57°$ using the relation:

$$i = \arccos\left(1 - \langle\epsilon\rangle\right) \tag{5.31}$$

where $\langle\epsilon\rangle = 0.45$ is the mean ellipticity of the NGC 7664 disk measured with the ellipse fitting. Moreover, we fixed the mass of the central supermassive black hole using the $M_\bullet - \sigma$ relation of Kormendy & Ho (2013). Since the radius of influence is not resolved, for the calculation of $M_\bullet$ we used the central velocity dispersion value $\sigma_0 = 80.3$ km s^{-1}. The obtained value for the black hole mass is $M_\bullet = 5.6 \times 10^6$ M$_\odot$, in line with other supermassive black hole masses of late-type (Kormendy & Ho, 2013).

The JAM code is able to implement also the convolution with the PSF of the kinematic observations. However, since the value of the PSF was not indicated in the available observing log, we adopted a conservative estimation of FWHM = 0.85 arcsec, which is the maximum value of the seeing allowed to start the observation with the GN telescope. So, the kinematic data points with galactocentric distance $R < 0.85$ arcsec were excluded from the fit.

The first step before performing the JAM modelling is the preparation of the stellar kinematic data to give as input to the code. For the measurement of the kinematic along the major axis, the slit of the spectrograph was rotated with an angle of 270°, while for the minor axis it was rotated of 0°. However, from the ellipse fitting we measured the mean PA of the NGC 7664 disk $\langle\text{PA}\rangle = 86.75°$

---

[1]The `jampy` package can be retrieved at the following link: `https://pypi.org/project/jampy/`.

Table 5.1: Parameters of the best-fitting JAM models. The rows are: (1) mass-to-light ratio; (2) anisotropy parameter; (3) mass of the dark matter halo; (4) mass density of the dark matter halo at the scale radius; (5) scale radius; (6) power index of the gNFW halo density profile; (7) central mass density of the dark matter; (8) core radius; (9) chi square; (10) reduced chi square.

Parameter	Units		Self	NFW	gNFW	QIS
Υ	$[\mathrm{M}_\odot\,\mathrm{L}_\odot^{-1}]$	(1)	2.90 ± 0.05	2.12 ± 0.07	2.12	2.14 ± 0.11
β_z		(2)	-0.68 ± 0.18	0.03 ± 0.06	0.07 ± 0.04	0.08 ± 0.07
M_{DM}	$[\mathrm{M}_\odot]$	(3)	...	$10^{(14.14\pm0.16)}$	...	...
ρ_{s}	$[\mathrm{M}_\odot\,\mathrm{pc}^{-3}]$	(4)	...	...	$10^{(-4.04\pm0.17)}$	...
R_{s}	$[\mathrm{pc}]$	(5)	...	...	$(3.56 \pm 0.43) \times 10^5$	...
γ		(6)	...	...	-1.05 ± 0.07	...
ρ_0	$[\mathrm{M}_\odot\,\mathrm{pc}^{-3}]$	(7)	...	...	...	$10^{(-0.44\pm0.15)}$
R_{c}	$[\mathrm{pc}]$	(8)	...	...	...	$(1.12 \pm 0.22) \times 10^5$
χ^2		(9)	434.45	142.05	177.05	134.03
χ_R^2		(10)	6.58	2.15	2.36	2.03

$\pm 0.36°$. Therefore the kinematic data were not taken exactly along the major and minor axis, but they are tilted with respect to them by an angle $\Delta\mathrm{PA} = 3°$. To correct this offset, we used the a `python3` script written by C. Buttitta that takes as input the kinematic data along the major and minor axes written as a function of their distance from the center R (Figure 3.5) and map them into a coordinate system (x, y), where the x and y axes correspond to the major and minor axes of NGC 7664 and rotate with an angle of $\Delta\mathrm{PA} = 3°$, that corresponds to the offset between the position of the spectrograph slit and the major axis of the galaxy.

5.2.1   Self-consistent model

We fitted the data with JAM with a model where the potential is given only by the mass density coming from the surface brightness distribution and a supermassive black hole of mass $M_\bullet = 5.6 \times 10^6\ \mathrm{M}_\odot$, while there is no dark matter. The mass density is given by Equation 5.7. In this case the only free parameters fitted by JAM were Υ and β_z. Then, using the parameters of the MGE parametrization of the galaxy surface brightness, galaxy inclination $i = 57°$, distance $D = 46.1$ Mpc, and the fitted Υ, we calculated the enclosed mass $M_{\mathrm{L}}(< R)$, mass density $\rho_{\mathrm{L}}(R)$ and circular velocity $v_{\mathrm{c,L}}(R)$ radial profiles for the luminous component with the functions `mge_radial_mass,` `mge_radial_density`, and `mge_vcirc` of the `mgefit` library, respectively.

5.2.2   Navarro, Frenk, & White model

In this case, in addition to the mass density given by the luminous component and supermassive black hole, we added to the model a spherical Navarro, Frenk, & White (NFW) dark-matter halo (Navarro et al., 1997), whose mass density is given by the parametrization of Klypin et al. (2011):

$$\rho_{\mathrm{DM}}(R) = \frac{M_{\mathrm{DM}}}{4\pi A_{\mathrm{c,vir}}} \frac{1}{R(r_{\mathrm{s}} + R)^2}, \tag{5.32}$$

where M_{DM} is the total mass of the halo and:

$$A_{\mathrm{c,vir}} = \log(1 + c_{\mathrm{vir}}) - \left(\frac{c_{\mathrm{vir}}}{1 + c_{\mathrm{vir}}}\right), \tag{5.33}$$

$$c_{\mathrm{vir}} = 9.6 \Big(\frac{0.7 M_{\mathrm{DM}}}{10^{12}} \Big)^{-0.075}, \tag{5.34}$$

$$r_{\mathrm{s}} = \Big(\frac{3 M_{\mathrm{DM}}}{4\pi 8.1 \times 10^{-6}} \Big)^{1/3}, \tag{5.35}$$

are a parameter of the dark-matter halo, the median concentration and the scale radius, respectively. For the model NFW halo, the free parameters fitted by JAM were Υ, β, and M_{DM}. From the density profile we can calculate the enclosed dark matter mass profile:

$$M_{\mathrm{DM}}(< R) = 4\pi \int_{r=0}^{R} \rho_{\mathrm{DM}}(r) r^2 dr \tag{5.36}$$

where $\rho_{\mathrm{DM}}(r)$ is the density at the radius r given by Equation 5.32. From the enclosed mass we derived the circular velocity profile of the dark matter component:

$$v_{\mathrm{c, DM}}(R) = \sqrt{\frac{M_{\mathrm{DM}}(< R) G}{R}}. \tag{5.37}$$

The total enclosed mass and density are given by the sum of the ones coming from the luminous and dark matter components, while the total circular velocity is given by:

$$v_{\mathrm{c}}(R) = \sqrt{v_{\mathrm{c, L}}^2(R) + v_{\mathrm{c,DM}}^2(R)}. \tag{5.38}$$

5.2.3   Generalized Navarro, Frenk, & White model

In this case we added a dark matter halo, whose mass density profile is the generalization of the one given by Navarro et al. (1997):

$$\rho_{\mathrm{DM}}(R) = \rho_{\mathrm{s}} \, R \, \gamma \bigg(\frac{2}{1+R} \bigg)^{(\gamma+3)} \tag{5.39}$$

where ρ_{s} is the mass density of the halo at its scale radius and γ is a power index for the halo. When $\gamma = -1$ this formula becomes the NFW halo density profile. For the generalized NFW (gNFW) halo the free parameters fitted by JAM were $\beta_z, \rho_{\mathrm{s}}, R_{\mathrm{s}}$, and γ, while Υ was fixed to the value found using the model with the NFW halo. This was done because when it was left as free parameter, the best fitting model was the one with $\Upsilon = 0$, that has no physical meaning. Then, inserting Equation 5.39 into Equation 5.36 we got the enclosed mass profile. Then, putting this profile into Equation 5.37 we obtained the circular velocity profile of the gNFW dark matter halo. These profiles were combined with the ones of the luminous component to obtain the total $M(< R)$, $\rho(R)$, and $v_{\mathrm{c}}(R)$ profiles.

5.2.4   Quasi-isothermal sphere model

Lastly, in addition to the mass density given by the luminous component and supermassive black hole, we added a quasi-isothermal spherical (QIS) dark matter halo, whose mass density radial profile is given by:

$$\rho(R) = \rho_0 \left[1 + \Big(\frac{R}{R_{\mathrm{c}}} \Big)^2 \right]^{-1}, \tag{5.40}$$

where ρ_0 is the central mass density and R_{c} is the core radius of the halo. In this case, the free parameters fitted by JAM were $\Upsilon, \beta_z, \rho_0$, and R_{c}. Then, inserting Equation 5.40 into Equations 5.36 and 5.37 we obtained the enclosed mass and circular velocity profiles of the QIS dark matter halo. These were combined with the luminous profile to obtain the total $M(< R)$, $\rho(R)$, and $v_{\mathrm{c}}(R)$ profiles.
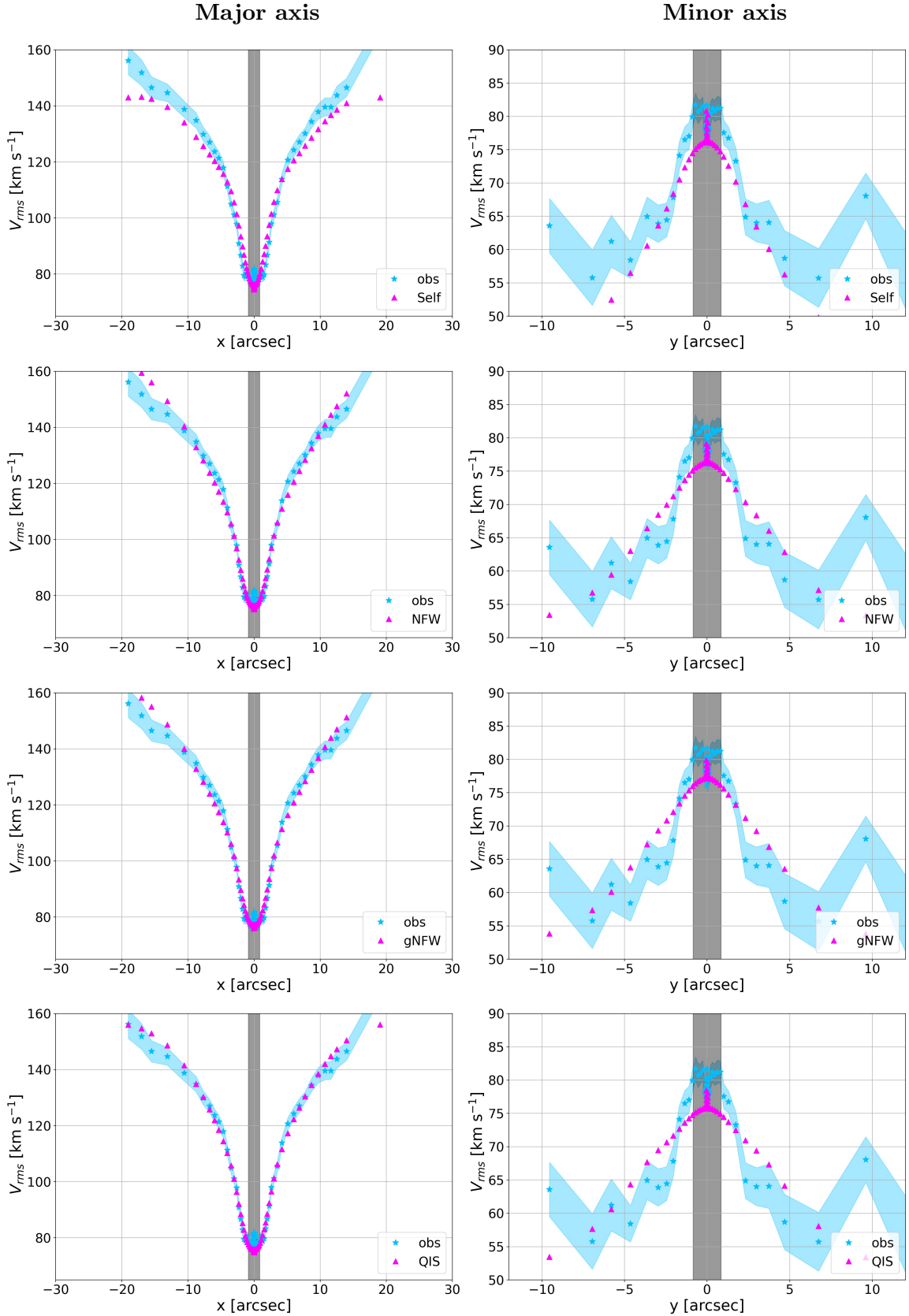
Figure 5.1: Observed and JAM kinematics of NGC 7664. V_{rms} radial profiles extracted along slices of 2-arcsec width taken on the major (*left panels*) and minor (*right panels*) axes of NGC 7664. The blue stars are the observed data, the blue area represents the measurement errors. The purple triangles represent the values coming from the JAM fitting. The gray area indicates the PSF radial range of 0.85 arcsec excluded from the fitting. *From top to bottom panels*: results for the self-consistent, NFW, gNFW, and QIS models, respectively.
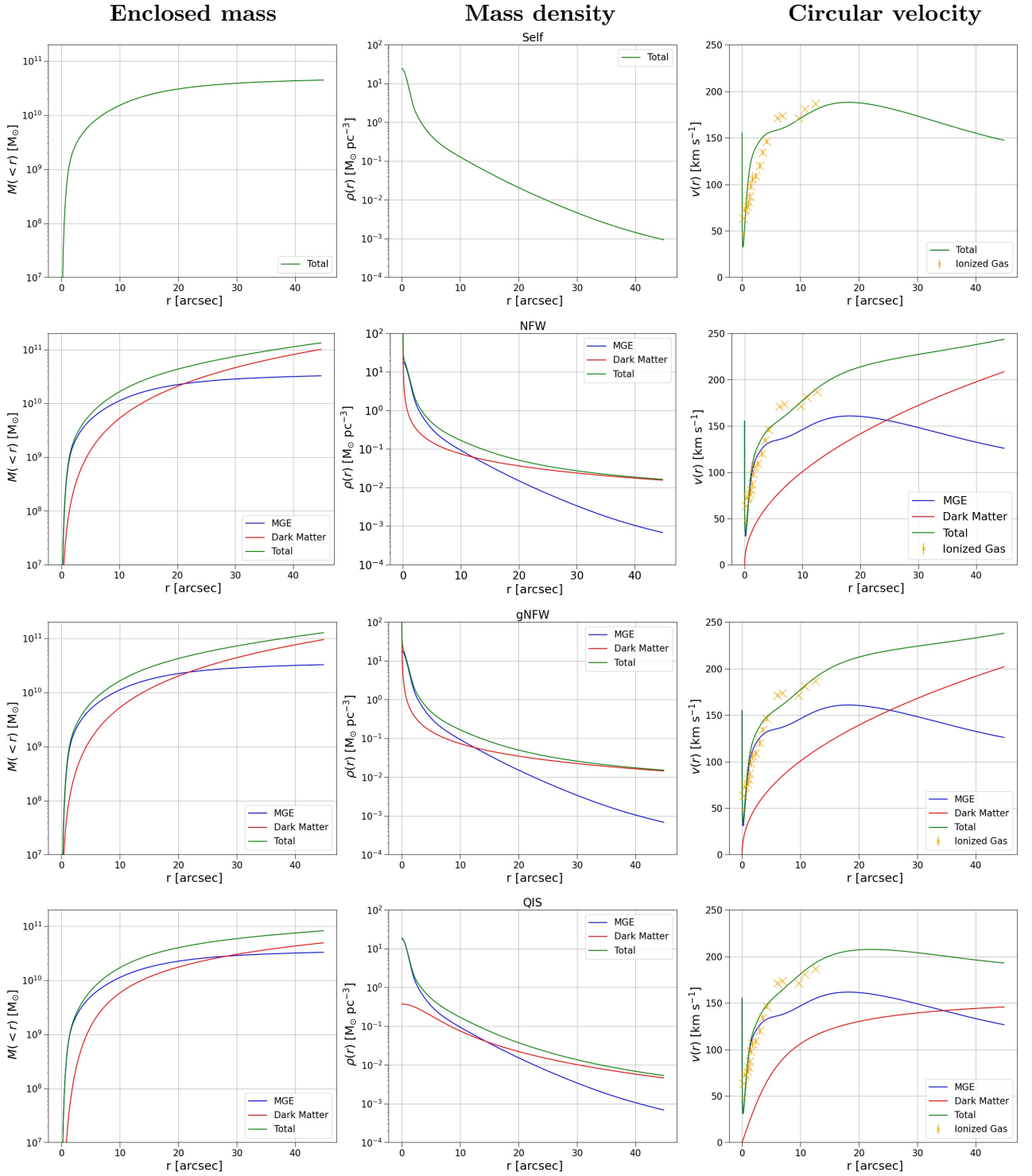
Figure 5.2: Enclosed mass (*left panels*), mass density (*middle panels*), and circular velocity (*right panels*) radial profiles computed from the best-fitting model of JAM. The blue, red, and green lines represent the luminous, dark matter, and total component, respectively. The deprojected ionized-gas velocity data of Cuomo (2015) are overplotted to the circular velocity profile (yellow crosses). *From top to bottom panels*: result for the self-consistent model and models with the NFW, gNFW, and QIS dark matter halo, respectively.
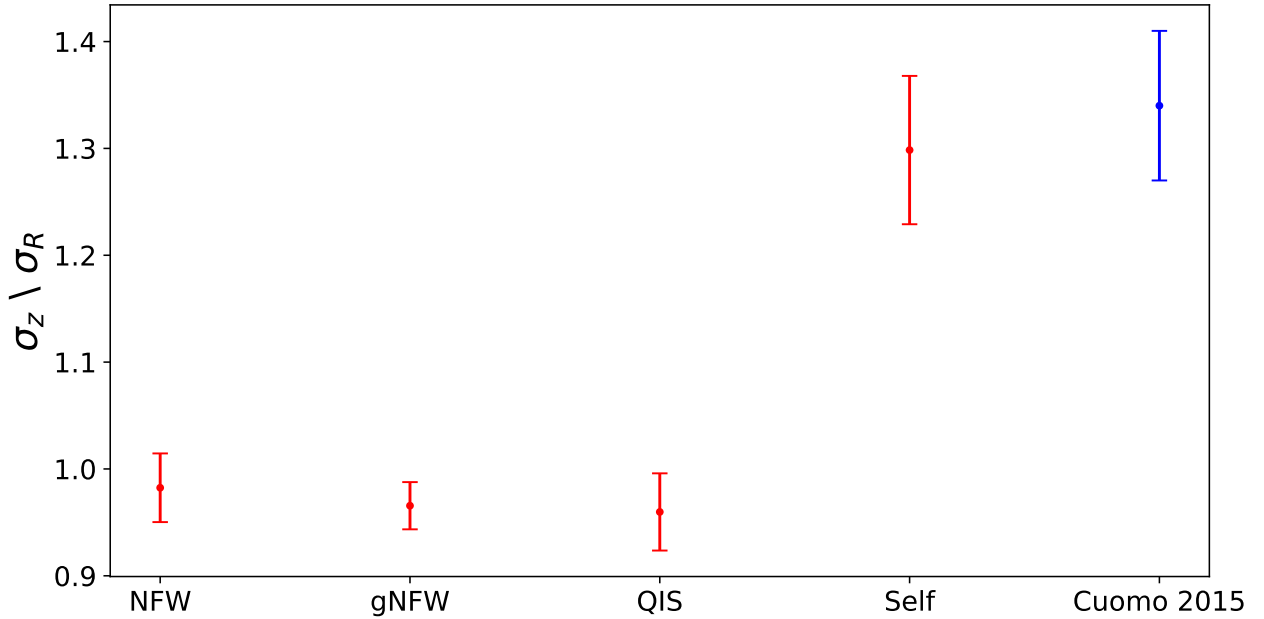
Figure 5.3: Values of the σ_z/σ_R ratio from JAM modelling. *From left to right*: results of the NFW, gNFW, QIS, and self-consistent models. The blue point is the value found with the asymmetric drift modelling by Cuomo (2015).

5.3 Results of the Jeans anisotropic modelling

The JAM model produced the best fitting parameters for each model we adopted. In addition to the parameters, the code returns the χ^2 of the best fitting model and the reduced χ^2, defined as:

$$\chi^2_{\mathrm{red}} = \frac{1}{N_{\mathrm{dof}}}, \tag{5.41}$$

where N_{dof} is the number of degrees of freedom, corresponding to the difference between the number of data and the free parameters.

The values of the best fitting parameters for each model, together with the values of the χ^2 and χ^2_{red} are listed in Table 5.1. The enclosed mass, mass density, and circular velocity profiles for the luminous, dark matter, and total components derived from each model are shown in Figure 5.2. Since the velocity of the ionized gas is a good tracer for the circular velocity, we deprojected the values v_{gas} measured by Cuomo (2015) for the NGC 7664 inclination $i = 57°$ and position angle $\phi = 87°$:

$$v_{\mathrm{gas},\,0} = \frac{v_{\mathrm{gas}}}{\sin i \cos \phi}, \tag{5.42}$$

and we plotted the deprojected ionized-gas velocity profile together with the circular velocity calculated with the best fitting parameters coming from the JAM modelling to compare them.

5.3.1 Measurement of the σ_z/σ_R ratio

From the fitted parameter β_z in the JAM modelling, we calculated the shape of the SVE of NGC 7664. Since the anisotropy parameter is defined as $\beta_z = 1 - \sigma_z^2/\sigma_R^2$, the ratio between the vertical and radial components of the velocity dispersion can be derived as:

$$\frac{\sigma_z}{\sigma_R} = \sqrt{1 - \beta_z}. \tag{5.43}$$

63

Table 5.2: Ratio between the z and R components of the SVE of NGC 7664 taken from Cuomo (2015) and obtained from the JAM modelling.

Model	σ_z/σ_R
Asymmetric drift	1.34 ± 0.07
Self	1.30 ± 0.07
NFW	0.98 ± 0.03
gNFW	0.97 ± 0.02
QIS	0.96 ± 0.04

From this formula we derived the shape of the SVE for the models that contains a dark-matter halo and self-consistent one. The resulting values of σ_z/σ_R from the JAM modelling with the corresponding errors, together with the value found by Cuomo (2015) using the asymmetric drift modelling are listed in Table 5.2 and plotted in Figure 5.3.

Chapter 6

Discussion and conclusions

In this chapter we discuss the obtained results and we present the future perspectives and conclusions of this thesis. In Section 6.1 we summarize the results we obtained. In Section 6.2 we discuss these results and we present the galaxies we found in literature with a SVE possibly elongated along the vertical direction. In Section 6.3 we describe the future perspectives of this thesis, that are the application of integral-field spectroscopy and orbit-superposition dynamical modelling. Finally, in 6.4 we present the conclusions.

6.1 Summary of the results

In this thesis we aim at studying the disk heating mechanism of the Sc NGC 7664 by measuring the shape of its SVE. The galaxy total absolute magnitude is $M_{B_{\mathrm{T}}}^0 = -20.4$ mag, which was measured using a distance $D = 46.1 \pm 3.2$ Mpc and its isophotal major and minor diameters measured at a surface brightness level of $\mu_B = 25$ mag arcsec^{-2} are $D_{25} \times d_{25} = 20.1$ kpc $\times 8.0$ kpc. We performed the photometric analysis of NGC 7664 using its i-band image taken from the DAS of the SDSS Data Release 17 (Abdurro'uf et al., 2022). After the sky-subtraction, we did an ellipse fitting of the galaxy surface-brightness distribution to derive the surface brightness, position angle, and ellipticity radial profiles. From these last two profiles we measured the mean values for the galaxy disk $\langle \mathrm{PA} \rangle = 86.75 \pm 0.36°$ and $\langle \epsilon \rangle = 0.45 \pm 0.1$, which corresponds to an inclination $i = 57°$. Then we performed an MGE fitting of the NGC 7664 $i-$band image to parametrize the galaxy surface-brightness distribution. To measure the SVE shape we used also the stellar kinematics data obtained from long-slit spectra taken with the GN telescope by Cuomo (2015) at PA $= 270°$ and PA $= 0°$ for the major and minor axes, respectively. Cuomo (2015) extracted the stellar and ionized-gas kinematics and used these data to measure the shape of the SVE using the asymmetric drift dynamical modelling, finding the controversial value of $\sigma_z/\sigma_R = 1.34 \pm 0.07$.

We measured the SVE shape using the JAM modelling from the MGE parametrization of the galaxy surface-brightness distribution and stellar kinematics data. From the JAM modelling we found a value of $\sigma_z/\sigma_R = 0.97 \pm 0.03$ when a dark matter halo is considered and a value of $\sigma_z/\sigma_R = 1.30 \pm 0.07$ using a self-consistent model with no dark matter. This last result is consistent with the one found by Cuomo (2015) using the asymmetric drift modelling.

6.2 Discussion

NGC 7664 is not the only galaxy with a SVE possibly elongated along the vertical direction. By expanding the sample by Pinna et al. (2018), we found 105 galaxies with a measured σ_z/σ_R ratio. These ratios as a function of the galaxy Hubble type are shown in Figure 6.1. We counted 23 galaxies (22%) which have $\sigma_z/\sigma_R \geq 1$ within 1σ confidence limit and 12 galaxies (11%) which have $\sigma_z/\sigma_R > 1$ but are not consistent with $\sigma_z/\sigma_R = 1$ within 1σ confidence limit. These galaxies range a wide interval of morphological types from S0 to Sd. Their σ_z/σ_R ratios are listed in Table 6.1 and their multi-band

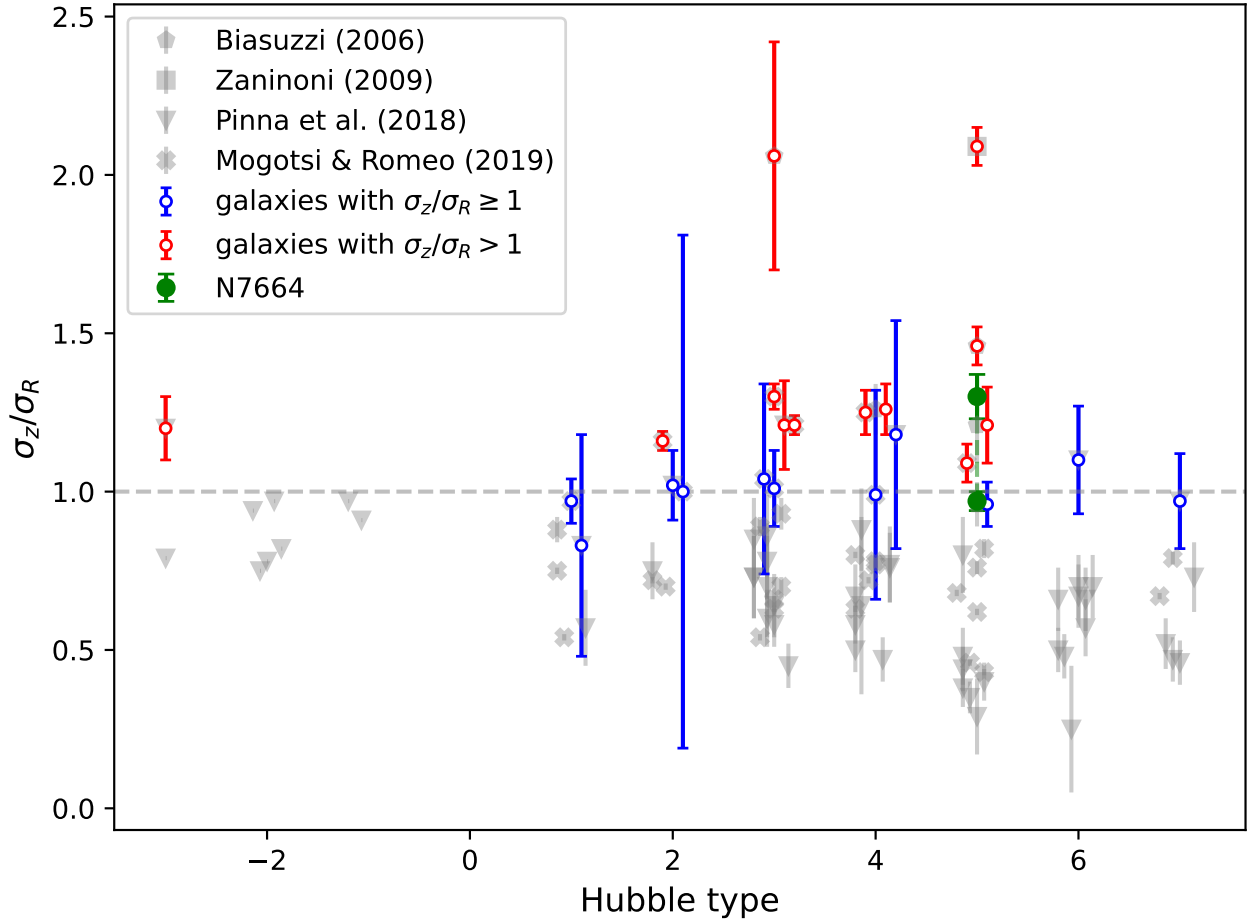Figure 6.1: The σ_z/σ_R ratio as a function of Hubble Type. The grey pentagons, squares, triangles, and crosses are the values obtained for 105 galaxies with a measured σ_z/σ_R ratio of the SVE taken from Biasuzzi (2006), Zaninoni (2009), Pinna et al. (2018), and Mogotsi & Romeo (2019), respectively. The green solid circles mark the values we obtained with JAM. The blue open squares are the galaxies with $\sigma_z/\sigma_R > 1$ which are consistent with $\sigma_z/\sigma_R = 1$ within 1σ. The red open circles are the galaxies with $\sigma_z/\sigma_R > 1$ which are not consistent with $\sigma_z/\sigma_R = 1$ within 1σ. The dashed line marks the isotropic case $\sigma_z/\sigma_R = 1$. The points are horizontally shifted to improve the visualization.

images taken from the DAS of the SDSS data release 17 (Abdurro'uf et al., 2022) or the data archive of the Digitized Sky Survey (DSS) are shown in Figure 6.2. All these galaxies show no evidence of a disturbed morphology or interactions, with the exception of NGC 7664, which has an asymmetric outer spiral arm.

Here we summarize the results only for the galaxies which are not consistent with $\sigma_z/\sigma_R \leq 1$.

Emsellem et al. (1999) They used dynamical three-integral analytical models to fit photometric and integral-field spectroscopic data of the S0 NGC 3115, finding a best-fitting value for the shape of the SVE of $\sigma_z/\sigma_R = 1.2 \pm 0.1$. They concluded that their models are accurately fitting the light distribution of the galaxy and included the derivation of the distribution function. However, their analysis was not focused on deriving the shape of the SVE, so they did not discuss the disk heating mechanism.

Biasuzzi (2006) The asymmetric drift modelling was used to fit photometric and long-slit spectroscopic data to measure the shape of the SVE of 11 low surface-brightness (LSB) galaxies with morphological type from Sa to Sc. Biasuzzi (2006) found a value of $\sigma_z/\sigma_R = 1.26 \pm 0.08$ for ESO-LV 189-G07, $\sigma_z/\sigma_R = 1.21 \pm 0.12$ for ESO-LV 206-G14, $\sigma_z/\sigma_R = 2.06 \pm 0.36$ for ESO-LV 446-G17, and $\sigma_z/\sigma_R = 1.46 \pm 0.06$ for ESO-LV 514-G10, respectively.

Table 6.1: SVE shape of galaxies with $\sigma_z/\sigma_R > 1$. The columns are: (1) name of the galaxy; (2) morphological type from de Vaucouleurs et al. (1991); (3) measure of the σ_z/σ_R ratio; (4) reference for the measure of σ_z/σ_R; (5) dynamical method used to measure the shape of the SVE.

Galaxy name	Hubble type	σ_z/σ_R	Reference	Method
(1)	(2)	(3)	(4)	(5)
ESO-LV 189-G07	SAB(rs)bc	1.26 ± 0.08	Biasuzzi (2006)	Asymmetric drift
ESO-LV 206-G14	SAB(s)c	1.21 ± 0.12	Biasuzzi (2006)	Asymmetric drift
ESO-LV 446-G17	(R)SB(s)b	2.06 ± 0.36	Biasuzzi (2006)	Asymmetric drift
ESO-LV 514-G10	SAB(s)c:	1.46 ± 0.06	Biasuzzi (2006)	Asymmetric drift
NGC 2742	SA(s)c	2.09 ± 0.06	Zaninoni (2009)	Asymmetric drift
NGC 3115	S0$^-$	1.2 ± 0.1	Emsellem et al. (1999)	Three-integral dynamics
NGC 3223	SA(s)b	1.21 ± 0.14	Gentile et al. (2015)	Asymmetric drift
NGC 4664	Sb	1.30 ± 0.04	Mogotsi & Romeo (2019)	Self-consistent JAM
NGC 5056	Sc	1.09 ± 0.06	Mogotsi & Romeo (2019)	Self-consistent JAM
UGC 3253	Sb	1.21 ± 0.03	Mogotsi & Romeo (2019)	Self-consistent JAM
UGC 3539	Sbc	1.25 ± 0.07	Mogotsi & Romeo (2019)	Self-consistent JAM
UGC 5108	SBab	1.16 ± 0.03	Mogotsi & Romeo (2019)	Self-consistent JAM

Zaninoni (2009) The asymmetric drift modelling was used to fit photometric and long-slit spectroscopic data to measure the shape of the SVE of the Sc galaxy NGC 2742 finding a value of $\sigma_z/\sigma_R = 2.09 \pm 0.06$. She found the same result changing the galaxy inclination, increasing the radius where the disk starts to dominate over the spheroid, and changing the disk scale radius. She concluded that $\sigma_z/\sigma_R > 1$ is not due to errors in data acquisition and analysis or to the peculiar morphology of the galaxy.

Gentile et al. (2015) They used the asymmetric drift modelling of photometric and long-slit spectroscopic data to measure the shape of the SVE of the Sab galaxy NGC 3223 finding the best-fitting value of $\sigma_z/\sigma_R = 1.21 \pm 0.14$. They found the same result by changing the inclination, radius at which the disk starts to dominate, and scale radius of the surface brightness profile. Gentile et al. (2015) concluded that NGC 3223 is more vertically heated than expected and it is an outlier in the observational relation of Gerssen & Shapiro Griffin (2012).

Mogotsi & Romeo (2016) They used the JAM modelling of photometric and integral field spectroscopic data to measure the shape of the SVE of 34 spirals taken from the Calar Alto Legacy Integral Field Area survey (CALIFA, Sánchez et al., 2016) with morphological type from Sa to Sd. In this case they used a self-consistent model. Mogotsi & Romeo (2019) found a value of $\sigma_z/\sigma_R = 1.30 \pm 0.04$ for NGC 4664, $\sigma_z/\sigma_R = 1.09 \pm 0.06$ for NGC 5056, $\sigma_z/\sigma_R = 1.21 \pm 0.03$ for UGC 3253, $\sigma_z/\sigma_R = 1.25 \pm 0.07$ for UGC 3539, and $\sigma_z/\sigma_R = 1.16 \pm 0.03$ for UGC 5108. In their analysis, Mogotsi & Romeo (2019) performed a velocity dispersion cut-off and 20 per cent error cut-off to ensure the reliability and accuracy of their data. They concluded that these cut-offs led to the loss of many low-quality data that affected the analysis at large radii.

All the previous results were obtained using different methods based on the asymmetric-drift (Biasuzzi, 2006; Zaninoni, 2009; Gentile et al., 2015) and dynamical modelling (Emsellem et al., 1999; Mogotsi & Romeo, 2019). However, none of them takes into account for the presence of dark matter.

Our results based on the JAM modelling show that when we fit the data using a self-consistent model, we find a σ_z/σ_R ratio that is consistent with the one obtained by Cuomo (2015) using the asymmetric drift modelling. The $\chi^2_{\rm red}$ of the best-fitting self-consistent model is not optimal and values of $V_{\rm rms}$ on the major axis computed by this model are systematically lower with respect to the observed ones

for $R > 5$ arcsec (Figure 5.1). Moreover, the circular velocity profile computed for the self-consistent model does not match the deprojected ionized-gas velocity data in the central regions of the galaxy (Figure 5.2). On the other hand, when we model the data taking into account the contribution of a spherical dark matter halo we found that the SVE shape becomes nearly isotropic, with a mean value of $\sigma_z/\sigma_R = 0.97 \pm 0.03$. In particular, we obtained $\chi^2_{\rm red} = 2.03$ with the QIS model and the observed $V_{\rm rms}$ profile on the major axis is well fitted even at large radii (Figure 5.1). Moreover, the circular velocity profile computed from the models with a dark matter halo matches the deprojected ionized-gas velocity data in the central regions of the galaxy (Figure 5.2). These results suggest that the peculiar values of σ_z/σ_R may be caused by the fact that the methods used to derive the shape of the SVE do not take into account the presence of a dark matter halo. However, to test this hypothesis we should model with JAM the data of other peculiar galaxies whose SVE has been already measured with asymmetric-drift modelling or a dynamical model without dark matter.

Molecular clouds Spitzer & Schwarzschild (1951) and minor mergers Quinn et al. (1993) produce a nearly isotropic SVE. We conclude that minor mergers are the main heating mechanism of the stellar disk of NGC 7664 since this galaxy has a very low content of molecular gas ($\log M_{\rm H_2}/M_{\rm HI} = -1.2$, Sauty et al., 2003) with respect to the other Sc spirals ($\langle \log M_{\rm H_2}/M_{\rm HI} \rangle = -0.75$, Obreschkow & Rawlings, 2009) and its outermost spiral arm shows a morphologically disturbed shape suggestive of a tidal interaction (Figure 2.3).

Another possible explanation for the observed $\sigma_z/\sigma_R > 1$ ratios could be that we are observing these galaxies in a certain phase of their evolution. Indeed, the shape of the SVE can change with time and the only disk heating mechanism that causes these changes is a merger event (Walo-Martín et al., 2021). Pinna et al. (2018) studied the evolution of the σ_z/σ_R ratio as a function of time using five simulated galaxies. They found that for four of them the shape of the SVE changes significantly with time. In particular, in one case the σ_z/σ_R increases up to $\sigma_z/\sigma_R \sim 1.3$ at 9 Gyr and then drops down to $\sigma_z/\sigma_R \sim 0.6$ after ~ 3 Gyr (Figure 6.3). However, this increase of the σ_z/σ_R ratio is not due to a vertical heating mechanism, but due to a faster cooling of σ_R with respect to σ_z. On the other hand, the time evolution of the SVE shape by Walo-Martín et al. (2021) on $Auriga$ galaxies shows that some of them present changes in the σ_z/σ_R ratio in periods of time where heating events occur from mergers (Figure 1.6. These changes might lead to increasing or decreasing of σ_z and σ_R at different rates. These results suggest that the $\sigma_z/\sigma_R > 1$ ratios in observed galaxies may be due to a phase of their evolution where σ_R decreased faster with respect to σ_z, or because they recently suffered merger events.

6.3 Future perspectives

6.3.1 Integral-field spectroscopy

In this thesis we used the stellar kinematics derived from long-slit spectroscopic data taken with the GN telescope and reduced by Cuomo (2015). The observations were not carried out exactly on the major and minor axes of NGC 7664, but the slits was tilted by an angle ΔPA = 3° with respect to these axes. Even if we obtained a good fitting using the JAM modelling, with a $\chi^2_{\rm red} = 2.03$ for the QIS model, the long-slit spectroscopy data does not provide a complete map of the stellar kinematics. Integral-field spectroscopic observations of NGC 7664 would allow us to perform the JAM modelling to better constrain the shape of the SVE.

6.3.2 Orbit-superposition dynamical modelling

Another aspect to take into account is that the JAM modelling return the best-fitted value of the β_z parameter, from which we can obtain the value of the global σ_z/σ_R ratio of the galaxy. However, Walo-Martín et al. (2021) which studied the local variations of the SVE in the $Auriga$ galaxies pointed out that the global SVE of galaxies does not help to constrain the dynamical heating that affects the stars in the disk of galaxies. The spatial variations of the SVE are important because they can be used to reconstruct the galaxy evolutionary history. To have a more accurate constrain on the disk heating

NGC 3223 **NGC 3115** **NGC 2742** **ESO-LV 189-G07**

ESO-LV 206-G14 **ESO-LV 446-G17** **ESO-LV 514-G10** **NGC 4664**

NGC 5056 **UGC 3253** **UGC 3539** **UGC 5108**
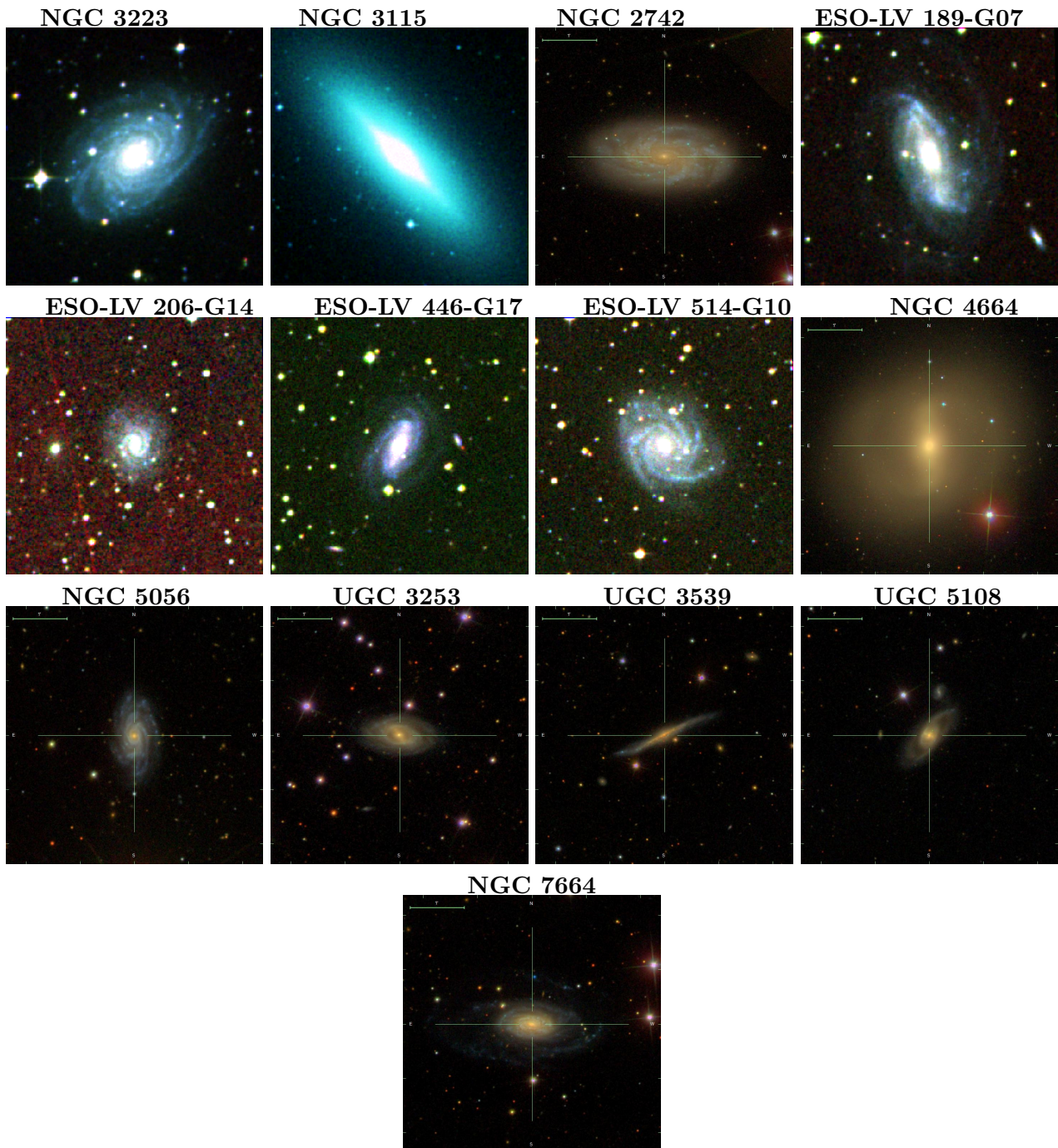
NGC 7664

Figure 6.2: Multi-band images of the galaxies reported in Table 6.1. The images of the galaxies with a haircross are taken from the SDSS archive, while the other ones are from the DSS archive. All the images have a field of view of $5 \times 5\,\mathrm{arcmin}^2$ with north up and east left.
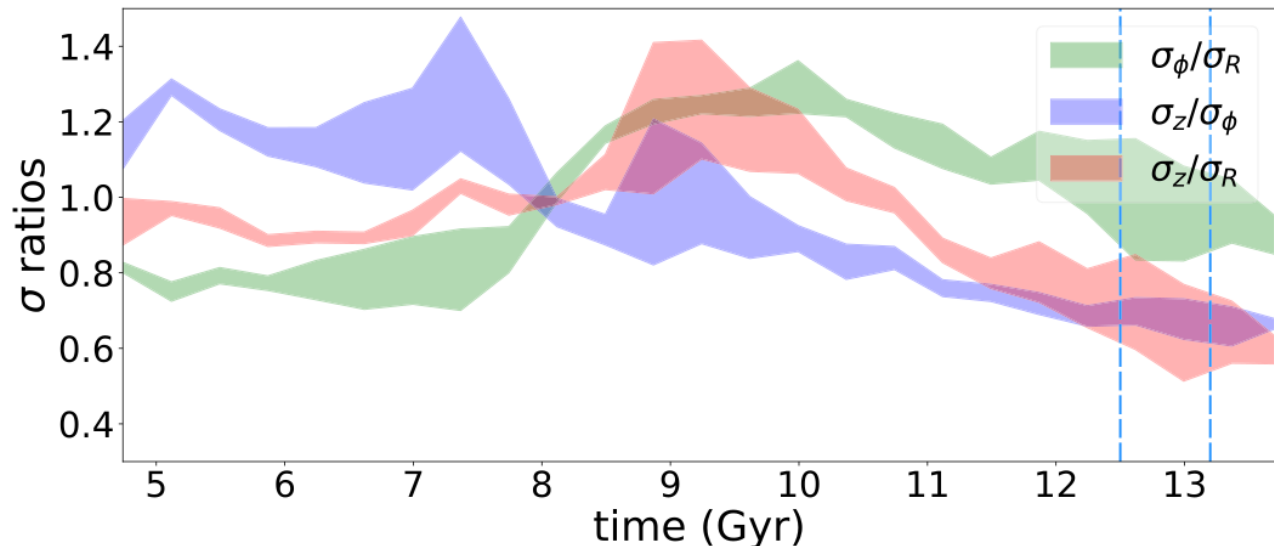
Figure 6.3: Evolution in time of the SVE axial ratios from a simulated galaxy. The shaded green, blue, and red areas mark the 16% and 84% percentiles of the values for σ_ϕ/σ_R, σ_z/σ_ϕ, and σ_z/σ_R, respectively. The dashed vertical lines indicates the epochs where the mergers occur. (Pinna et al., 2018)

mechanism we should then use a dynamical model based on the Schwarzschild's orbit superposition method (Schwarzschild, 1979), which allows to investigate these spatial variations and isolate the contribution of the disk of the galaxy.

The orbit superposition method proposed by Schwarzschild (1979) is a flexible method to build dynamical models of galaxies. The original implementation was aimed at reproducing a given triaxial density distribution. Subsequently it was applied to a large variety of densities distributions. The application of this method on NGC 7664 would allow us to accurate constrain on the disk heating mechanism, by investigating the spatial variations of the SVE and isolate the contribution of the disk of the galaxy. Basically, this technique creates a model for an arbitrary potential, integrates the equations of motion for a representative orbit library and finds the orbital weights that best reproduce the mass density of the system to match the observations. This method can include the presence of a supermassive black hole, a dark matter halo, and multiple kinematic components. In particular, we refer the triaxial modelling implementation by van de Ven et al. (2008). In the following we present a brief summary of this method.

In order to generate a gravitational potential, we need to construct a mass model given by the stellar and dark matter distributions, plus a point mass potential for a supermassive black hole. The stellar mass distribution is inferred from the intrinsic luminosity obtained from the deprojection of the surface brightness. To describe the stellar light distribution, the MGE parametrization is used (Section 2.4), while the dark matter distribution is described by a spherical NFW halo, whose density profile is given by Equation 5.32. The supermassive black hole contributes to the non luminous component. Its potential is described by Equation 5.10. For the modelling, the free parameters are: the dynamical M/L ratio Υ, the concentration of the dark matter halo c_{DM}, the fraction of dark-to-stellar mass $M_{200}/M_\star$, and the mass of the supermassive black hole $M_\bullet$.

After defining the mass model, the physically permitted orbits are generated via numerical integration. The sample of orbits has to be representative of the assumed potential. Even though the orbits in a MGE potential are more complicated than those in a separable potential, it is possible to use the properties of the latter for sampling the initial condition (van den Bosch et al., 2008). The sampling is done across the three conserved integrals of motion, E (the energy), I_2, and I_3. Then for each sampled energy the orbital intial condition are linearly sampled from a dense grid in the (x, z) plane. The orbits starting points (x, z) are selected from a polar grid (R, θ) in between the thin orbit and the
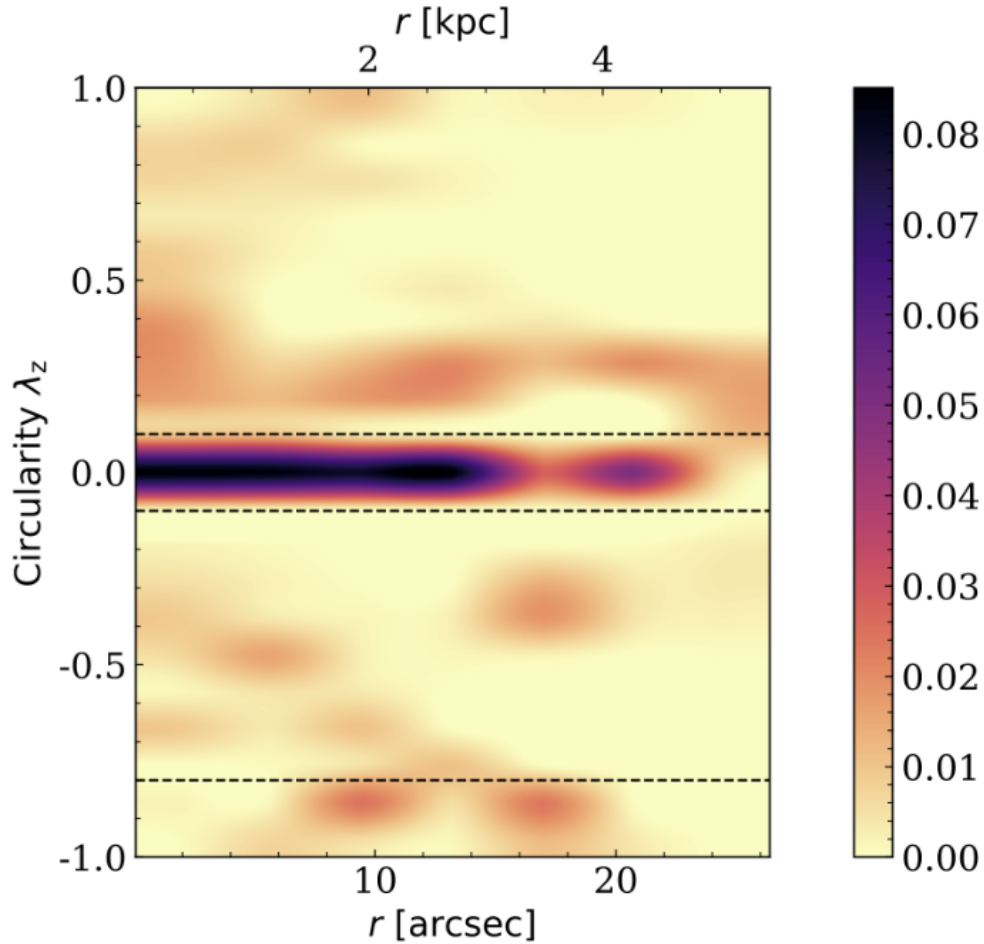
Figure 6.4: Circularity radial profile of the best-fitting Schwarzschild model of NGC 4191. The horizontal dashed lines mark the orbital cuts at $\lambda_z = -0.8, -0.1, 0.1$ (Rubino et al., 2021).

equipotential. The total numbers of orbits N_{orb} necessary to make a model depends on, for example, the number of observed kinematics, the size of the galaxy model, and the shape of the potential.

The orbit solution is given by the fit to observed data. Here, the MGE model and the kinematic maps are used as model constraints. Therefore, the solution of orbit weights is a linear least square problem, where the χ^2 function is computed by a non-negative least-squares fit to all observed constraints simultaneously. To constrain the luminosity distribution both the 2D MGE model describing the flux on the sky plane and the deprojected 3D MGE model giving the luminosity density are used. Similarly, for the kinematic data, the Gauss-Hermite parametrization of the velocity distribution by Gerhard (1993) and van der Marel & Franx (1993) is used.

We can now build a dynamical model using, for example, the code DYNAMITE[1] (i.e. dynamics, age and metallicity indicators tracing evolution, van den Bosch et al., 2008). The code requires as input the MGE parametrization of the light distribution and the kinematic data. Once the constraints are defined, we can set the grid of the model's parameters and run the simulations. When the parameter search is terminated, we get the best fitting model and the code performs the orbital decomposition. The best fitting model will have the total number of orbits sampled to get the solution N_{orb}. The orbits of the mode have intrinsic 3D angular momentum and orbital anisotropy. Thus for the best fitting model the code can calculate the radial profile of the circularity λ_z of each orbit, defined by Zhu et al. (2018) as:

---

[1]The DYNAMITE source code is available at the following link: `https://github.com/dynamics-of-stellar-systems/dynamite_release/releases`.

$$\lambda_z = \frac{\overline{L_z}}{\overline{r}\,\overline{V_c}}, \tag{6.1}$$

where $\overline{L_z}$, $\overline{r}$, and $\overline{V_c}$ are the mean angular momentum, radius, and circular velocity of the orbit, respectively. $|\lambda_z| = 1$ represent a circular orbit, while $\lambda_z = 0$ indicates a box or radial orbit. An example of λ_z radial profile from a Schwarzschild model of NGC 4191 by Rubino et al. (2021) is shown in Figure 6.4

From the orbits circularity profile of the best fitting model of NGC 7664 computed with DYNAMITE, we can identify a cold component with nearly circular orbits ($\lambda_z > 0.8$) and a hot component with radial orbits ($\lambda_z < 0.1$), while the orbits in between construct a warm component. By doing so, we can select only the orbits that belong to the disk of the galaxy (the ones with $\lambda_z > 0.8$) and calculate the radial profile of the σ_z/σ_R ratio. This would allow us to investigate the local variations of the SVE and constrain the dynamical heating only for the disk component, without any contamination from the galaxy spheroid.

6.4 Conclusions

We measured the SVE shape of the late-type spiral galaxy NGC 7664 using the JAM modelling, finding a best-fitting value of $\sigma_z/\sigma_R = 1.30 \pm 0.07$ with a self-consistent model and $\sigma_z/\sigma_R = 0.97 \pm 0.03$ when adding a dark matter halo to the model. The self-consistent result is consistent with the one found by Cuomo (2015) using the asymmetric drift dynamical modelling. However, it does not reproduce well the stellar and ionized-gas kinematic data. We also found that 11% of the galaxies with a measured σ_z/σ_R ratio are not consistent with $\sigma_z/\sigma_R \leq 1$ within 1σ. However, all the methods used to measure the shape of the SVE do not take into account the presence of dark matter. Our results may suggest that these peculiar SVE shapes could be explained by the lack of consideration of a dark matter halo into the method used to derive the σ_z/σ_R ratio. On the other hand, the studies on the time evolution of the σ_z/σ_z ratio (Pinna et al., 2018; Walo-Martín et al., 2021) pointed out that some galaxies can show a value of $\sigma_z/\sigma_R > 1$ for a limited amount of time in their evolution. We conclude that minor mergers are responsible for the nearly isotropic SVE of NGC 7664. Indeed, the galaxy shows a very low content of molecular gas and displays a tidally-disturbed morphology of its outermost spiral arm.

From all these considerations we can conclude that dynamical heating in disk galaxies remains still a open question. Our results may suggest a lack in the methods used up to now for the measurements of the σ_z/σ_R ratio. However, to draw some conclusions we should use the JAM modelling on a larger sample of galaxies whose SVE shape was measured using other methods using both a self-consistent model and one with a dark matter halo and re-build the plot of Figure 6.1. Furthermore, the application of the Schwarschild's orbit-superposition dynamical modelling to integral-field unit data would also allows us to study in detail the σ_z/σ_R ratio coming only from the disk component and study its spatial variation. The large number of high-quality observations and the availability of state of the art dynamical models will allows us to compare observations with theoretical predictions to constrain the disk heating mechanisms in galaxies, which is essential to understand the dynamical state of galaxy disks.

Bibliography

Abdurro'uf et al., 2022, ApJS, 259, 35

Aihara H., et al., 2011, ApJS, 193, 29

Aumer M., Binney J., 2009, MNRAS, 397, 1286

Aumer M., Binney J., Schönrich R., 2016, MNRAS, 462, 1697

Barbanis B., Woltjer L., 1967, ApJ, 150, 461

Bender R., Saglia R. P., Gerhard O. E., 1994, MNRAS, 269, 785

Bendinelli O., 1991, ApJ, 366, 599

Biasuzzi B., 2006, B.Sc. Thesis, University of Padova

Binney J., Mamon G. A., 1982, MNRAS, 200, 361

Binney J., Tremaine S., 2008, Galactic Dynamics: Second Edition. Princeton University Press, Princeton

Bundy K., et al., 2015, ApJ, 798, 7

Cappellari M., 2002, MNRAS, 333, 400

Cappellari M., 2008, MNRAS, 390, 71

Cappellari M., Emsellem E., 2004, PASP, 116, 138

Cappellari M., et al., 2006, MNRAS, 366, 1126

Carlberg R. G., 1987, ApJ, 322, 59

Chilingarian I. V., Zolotukhin I. Y., 2012, MNRAS, 419, 1727

Cuomo V., 2015, M.Sc.Thesis, University of Padova

D'Onghia E., 2015, ApJ, 808, L8

Dehnen W., Binney J. J., 1998, MNRAS, 298, 387

Doi M., et al., 2010, AJ, 139, 1628

Emsellem E., Monnet G., Bacon R., 1994, A&A, 285, 723

Emsellem E., Dejonghe H., Bacon R., 1999, MNRAS, 303, 495

Emsellem E., et al., 2007, MNRAS, 379, 401

Franx M., 1988, MNRAS, 231, 285

Fukugita M., et al., 1996, AJ, 111, 1748

Gaia Collaboration et al., 2018, A&A, 616, A11

Gebhardt K., et al., 2000, ApJ, 539, L13

Gentile G., et al., 2015, A&A, 576, A57

Gerhard O. E., 1993, MNRAS, 265, 213

Gerhard O., Kronawitter A., Saglia R. P., Bender R., 2001, AJ, 121, 1936

Gerssen J., Shapiro Griffin K., 2012, MNRAS, 423, 2726

Gerssen J., Kuijken K., Merrifield M. R., 1997, MNRAS, 288, 618

Gimeno G., et al., 2016, in Evans C. J., Simard L., Takami H., eds, Society of Photo-Optical Instrumentation Engineers (SPIE) Conference Series Vol. 9908, Ground-based and Airborne Instrumentation for Astronomy VI. SPIE, Cardiff, p. 99082S

Grand R. J. J., et al., 2016, MNRAS, 459, 199

Grand R. J. J., et al., 2017, MNRAS, 467, 179

Gunn J. E., et al., 1998, AJ, 116, 3040

Gunn J. E., et al., 2006, AJ, 131, 2332

Guthrie B. N. G., 1992, A&AS, 93, 255

Hook I. M., et al., 2004, PASP, 116, 425

Huchra J. P., Vogeley M. S., Geller M. J., 1999, ApJS, 121, 287

Jedrzejewski R. I., 1987, MNRAS, 226, 747

Jenkins A., Binney J., 1990, MNRAS, 245, 305

Kazantzidis S., Bullock J. S., Zentner A. R., Kravtsov A. V., Moustakas L. A., 2008, ApJ, 688, 254

Kent S. M., 1985, ApJS, 59, 115

Kent S. M., 1988, AJ, 96, 514

Klypin A. A., Trujillo-Gomez S., Primack J., 2011, ApJ, 740, 102

Kormendy J., Ho L. C., 2013, ARA&A, 51, 511

Lacey C. G., 1984, MNRAS, 208, 687

Lawson C. L., Hanson R. J., 1974, Solving Least Squares Problems. Society for Industrial and Applied Mathematics, Philadelphia

Majewski S. R., et al., 2017, AJ, 154, 94

Malhotra S., 1995, ApJ, 448, 138

Martig M., Bournaud F., Croton D. J., Dekel A., Teyssier R., 2012, ApJ, 756, 26

Martig M., Minchev I., Flynn C., 2014, MNRAS, 443, 2452

Martinez-Valpuesta I., Knapen J. H., Buta R., 2007, AJ, 134, 1863

Martinez-Valpuesta I., Aguerri J. A. L., González-García A. C., Dalla Vecchia C., Stringer M., 2017, MNRAS, 464, 1502

Massey P., Strobel K., Barnes J. V., Anderson E., 1988, ApJ, 328, 315

Merrifield M. R., Gerssen J., Kuijken K., 2001, in Funes J. G., Corsini E. M., eds, Astronomical Society of the Pacific (ASP) Conference Series Vol. 230, Galaxy Disks and Disk Galaxies. ASP, San Francisco, pp 221–224

Mogotsi K. M., Romeo A. B., 2019, MNRAS, 489, 3797

Monnet G., Bacon R., Emsellem E., 1992, A&A, 253, 366

Moultaka J., Ilovaisky S. A., Prugniel P., Soubiran C., 2004, PASP, 116, 693

Navarro J. F., Frenk C. S., White S. D. M., 1997, ApJ, 490, 493

Newman P. R., et al., 2004, in Moorwood A. F. M., Iye M., eds, Society of Photo-Optical Instrumentation Engineers (SPIE) Conference Series Vol. 5492, Ground-based Instrumentation for Astronomy. SPIE, Cardiff, pp 533–544

Nordström B., et al., 2004, A&A, 418, 989

Obreschkow D., Rawlings S., 2009, MNRAS, 394, 1857

Padilla N. D., Strauss M. A., 2008, MNRAS, 388, 1321

Percival W. J., 2017, Physics Today, 70, 32

Pinna F., et al., 2018, MNRAS, 475, 2697

Planck Collaboration et al., 2014, A&A, 571, A16

Press W. H., Teukolsky S. A., Vetterling W. T., Flannery B. P., 1992, Numerical Recipes in FORTRAN. The Art of Scientific Computing. Cambridge University Press, Cambridge

Prugniel P., Soubiran C., 2001, A&A, 369, 1048

Quinn P. J., Hernquist L., Fullagar D. P., 1993, ApJ, 403, 74

Rix H.-W., White S. D. M., 1992, MNRAS, 254, 389

Rubin V. C., Ford W. K. J., Thonnard N., 1980, ApJ, 238, 471

Rubino M., et al., 2021, A&A, 654, A30

Saha K., Tseng Y.-H., Taam R. E., 2010, ApJ, 721, 1878

Sánchez S. F., et al., 2016, A&A, 594, A36

Sandage A., Bedke J., 1994, The Carnegie Atlas of Galaxies. Carnegie Institution of Washington Washington, D.C

Sarzi M., et al., 2006, MNRAS, 366, 1151

Satoh C., 1980, PASJ, 32, 41

Sauty S., et al., 2003, A&A, 411, 381

Schlafly E. F., Finkbeiner D. P., 2011, ApJ, 737, 103

Schwarzschild K., 1907, Nachrichten von der Gesellschaft der Wissenschaften zu Goettingen, Mathematisch-Physikalische Klasse, 5, 614

Schwarzschild M., 1979, ApJ, 232, 236

Shapiro K. L., Gerssen J., van der Marel R. P., 2003, AJ, 126, 2707

Spitzer Lyman J., Schwarzschild M., 1951, ApJ, 114, 385

Toth G., Ostriker J. P., 1992, ApJ, 389, 5

Velazquez H., White S. D. M., 1999, MNRAS, 304, 254

Walo-Martín D., et al., 2021, MNRAS, 506, 1801

Wielen R., 1977, A&A, 60, 263

Willmer C. N. A., 2018, ApJS, 236, 47

Zaninoni E., 2009, M.Sc. Thesis, University of Padova

Zhu L., et al., 2018, MNRAS, 473, 3000

de Vaucouleurs G., de Vaucouleurs A., Corwin Jr. H. G., Buta R. J., Paturel G., Fouque P., 1991,
    Third Reference Catalogue of Bright Galaxies. Springer-Verlag, New York (RC3)

van de Ven G., de Zeeuw P. T., van den Bosch R. C. E., 2008, MNRAS, 385, 614

van den Bosch R. C. E., van de Ven G., Verolme E. K., Cappellari M., de Zeeuw P. T., 2008, MNRAS,
    385, 647

van der Marel R. P., 1994, MNRAS, 270, 271

van der Marel R. P., Franx M., 1993, ApJ, 407, 525